Monolithic Heterovalent Integration of Compound Semiconductors and Their Applications

By

Maxwell Brock Lassise

A Dissertation Presented in Partial Fulfillment
of the Requirements for the Degree
Doctor of Philosophy

Approved April 2019 by the
Graduate Supervisory Committee:

Yong-Hang Zhang, Chair
David J. Smith
Shane R. Johnson
Martha R. McCartney

ARIZONA STATE UNIVERSITY

May 2019

ABSTRACT

Compound semiconductors tend to be more ionic if the cations and anions are further apart in atomic columns, such as II-VI compared to III-V compounds, due in part to the greater electronegativity difference between group-II and group-VI atoms. As the electronegativity between the atoms increases, the materials tend to have more insulator-like properties, including higher energy band gaps and lower indices of refraction. This enables significant differences in the optical and electronic properties between III-V, II-VI, and IV-VI semiconductors. Many of these binary compounds have similar lattice constants and therefore can be grown epitaxially on top of each other to create monolithic heterovalent and heterocrystalline heterostructures with optical and electronic properties unachievable in conventional isovalent heterostructures.

Due to the difference in vapor pressures and ideal growth temperatures between the different materials, precise growth methods are required to optimize the structural and optical properties of the heterovalent heterostructures. The high growth temperatures of the III-V materials can damage the II-VI barrier layers, and therefore a compromise must be found for the growth of high-quality III-V and II-VI layers in the same heterostructure. In addition, precise control of the interface termination has been shown to play a significant role in the crystal quality of the different layers in the structure. For non-polar orientations, elemental fluxes of group-II and group-V atoms consistently help to lower the stacking fault and dislocation density in the II-VI/III-V heterovalent heterostructures.

This dissertation examines the epitaxial growth of heterovalent and heterocrystalline heterostructures lattice-matched to GaAs, GaSb, and InSb substrates in a single-chamber growth system. The optimal growth conditions to achieve alternating

layers of III-V, II-VI, and IV-VI semiconductors have been investigated using temperature ramps, migration-enhanced epitaxy, and elemental fluxes at the interface. GaSb/ZnTe distributed Bragg reflectors grown in this study significantly outperform similar isovalent GaSb-based reflectors and show great promise for mid-infrared applications. Also, carrier confinement in GaAs/ZnSe quantum wells was achieved with a low-temperature growth technique for GaAs on ZnSe. Additionally, nearly lattice-matched heterocrystalline PbTe/CdTe/InSb heterostructures with strong infrared photoluminescence were demonstrated, along with virtual (211) CdZnTe/InSb substrates with extremely low defect densities for long-wavelength optoelectronic applications.

DEDICATION

In memory of my best friend Robby Mahoney

ACKNOWLEDGMENTS

I would like to thank my advisor, Dr. Yong-Hang Zhang, as well as my other committee members, Dr. David Smith, Dr. Shane Johnson, and Dr. Martha McCartney for their continued support. Additionally, I would like to thank my colleagues who have provided significant help along the way, including Dr. Brian Tracy for his relentless TEM work, Dr. Preston Webster for sharing his extensive knowledge of MBE and photoluminescence measurements, Dr. Peng Wang who provided valuable support with the heterovalent growth chamber, and Tyler McCarthy who has helped extensively with sample characterization and analysis. I would also like to thank my family for their undying love and support, and for providing me with every opportunity to succeed. This work was partially supported by AFOSR grant FA 9550-15-1-0196.

TABLE OF CONTENTS

Page

LIST OF TABLES

LIST OF FIGURES

Figure Page

Figure Page

CHAPTER 1

INTRODUCTION

Epitaxial growth of semiconductor heterostructures, particularly with molecular beam epitaxy (MBE) [1], has allowed for advances in technologies such as lasers [2], [3] infrared (IR) detectors [4]–[6], and high-speed electronics [7], [8], but close lattice-matching must be observed between the crystalline layers to retain epitaxial compatibility and keep dislocations from forming at the interface and propagating through the epilayers [9]. This constraint on the lattice size limits the variety of semiconductor material properties available for integration on a specific substrate, and can frustrate efforts to improve device performance due to the epitaxial limitations. Fortunately, every common III-V binary semiconductor has at least one corresponding binary II-VI material with a similar lattice constant but significantly different optical and electrical properties [10], [11]. This phenomenon typically occurs when the cations and anions of the two materials reside in the same atomic row, and therefore have similar atomic sizes. For example, Ga and Zn are in the same atomic row, as are Sb and Te, which results in GaSb and ZnTe having a very similar atomic spacing in the crystal lattice. While the two materials have a close lattice match, the differences in the ionicity between their constituent atoms leads to a significant difference in the material characteristics of the two semiconductors since the crystals with more ionic bonds generally tend to have more insulator-like properties, including a relatively high energy band gap, high resistivity, and a low dielectric constant (which results in a high index of refraction). These contrasting properties can be utilized numerous different ways in monolithic heterostructures by introducing new materials to

existing platforms to achieve structures which can probe novel physical phenomena and outperform state-of-the-art isovalent heterostructure devices.

With the advantages of heterovalent integration in mind, there are two unique challenges for combining these different materials into a single epitaxial heterostructure: First, the atoms at the heterovalent interface do not share eight valence electrons, therefore the interface bonding can shift the crystal structure to redistribute the electron bonds or create defects which can propagate into the upper layers if the interface growth conditions are not tuned properly [12]–[18]. This can also affect the electrical behavior of the structure as unwanted atomic diffusion between the II-VI and III-V layers will cross-contaminate the layers and the stray atoms will act as dopants that can supply or remove an electron from the lattice [19], [20]. The second challenge of heterovalent integration involves the different thermal properties of the materials. II-VI crystals tend to have higher vapor pressures and lower ideal growth temperatures than their lattice-matched III-V counterparts. This complicates the growth of III-V materials on II-VI layers since the growth must be started at a relatively low substrate temperature, and therefore a compromise must be found to obtain high-quality III-V layers without damaging the II-VI material during the growth [21]. The difficulties with the thermal properties of the heterostructure can be compounded with the epitaxial integration of additional materials, such as rock-salt lead chalcogenides, which have low growth temperatures similar to the II-VI materials but the thermal expansion coefficient is nearly an order of magnitude higher which can create dislocations in the layers after the growth is finished.

Integration of II-VI heterostructures on III-V substrates has been studied for decades [22], [23], with the first heterovalent structures being proposed as a path to

obtaining low-cost blue/green light emitters on GaAs [24]–[27]. The wide band gap, optical confinement potential, and close lattice match of ZnSe on GaAs also inspired a strong interest in II-VI/III-V integration, although these first heterostructures did not have heterovalent interfaces located near the active region to keep the interfaces from influencing the electrical and optical characteristics of the II-VI material [28], [29]. ZnSe-based heterostructures grown on inexpensive GaAs substrates were a promising candidate for elusive wide-band gap light emitters in the 90's [30]–[34], but difficulties with doping [35] eventually led to II-VI materials being overtaken by GaN for blue/green LEDs and lasers [36], [37]. In the years since, the focus of heterovalent integration has shifted to encompass the prospect of enhancing nearly every type of semiconductor device with an exceptional variety of material parameters available for any given lattice constant or substrate material. Recently, high-quality devices such as solar cells [38], [39], lasers [40], and detectors [41] consisting of at least one heterovalent interface have been achieved on commercially-available III-V substrates. Additionally, studies of the novel interface characteristics have shown that these heterovalent heterostructures can offer new functionality for applications impossible with isovalent structures alone, such as spintronics and topological insulators [42], [43].

In addition to heterovalent zincblende heterostructures, IV-VI lead chalcogenides with rock-salt crystal structures were epitaxially integrated with II-VI and III-V materials into heterocrystalline heterostructures. The motivation for these heterocrystalline structures follow a similar rationale, since many IV-VI semiconductor crystals are lattice-matched to III-V substrates, such as PbTe and InSb, but have significantly different optical and electrical properties. The integration of the lead chalcogenides with heterovalent III-

V/II-VI heterostructures enables another dimension of epitaxial integration which will allow for even more flexibility with the material properties in a single-crystal semiconductor structure. Lead salt IR devices have been studied since the 1930's and show promise for inexpensive room-temperature devices, but integration with III-V and II-VI materials has presented an issue due to the different crystal structure and large thermal expansion mismatch of the IV-VI materials compared to the III-V and II-VI crystals.

The growth of II-VI layers on III-V substrates has been relatively well-studied since the II-VI materials generally have a higher vapor pressure and lower growth temperature than the III-V materials, and therefore can be grown under ideal conditions without forming unintentional defects from diffusion or destruction of the epilayers. Previous studies have demonstrated how high-quality II-VI epilayers can be achieved by correctly tuning the interface flux conditions at both the end of the III-V layer and the initiation of the II-VI layer growth [44]. The case of III-V growth on II-VI layers is much more challenging because the relatively low vapor pressure of the group-III materials means that significantly higher substrate temperatures are required to provide the adatoms with enough thermal energy to migrate across the growth surface. If the substrate temperature is too low, the adatoms will favor a Volmer-Weber growth mode which results in the metallic atoms coalescing together to form three-dimensional islands [45]. Therefore, creative growth techniques and precise control over the growth conditions are required to achieve high-quality III-V layers on II-VI films. Due to these difficulties, only a small amount of samples have been reported which contain III-V layers epitaxially grown on II-VI materials, and there are only a few rare reports with convincing evidence of electrical

confinement and optical emission from III-V layers in close proximity to II-VI interfaces [46], [47].

For heterovalent growth in a single-chamber MBE system, even small operational aspects such as the temperature of the idle group-III cells can alter the flux ratio or cause unwanted evaporation of atoms from the shutters or sidewalls. Uncontrolled material evaporation could possibly cause unintentional doping in the layers or interfere with the delicate chemistry of the interfaces. The flux conditions at the interface play a critical role in determining the electrical configuration and bonding arrangement of the subsequent epilayers [48], and poor interface conditions can completely destroy an otherwise perfect crystal growth. Due to the buildup of charge at the heterovalent interface, more energetically favorable bonding configurations other than the expected bulk crystal structure may occur [49], and hence control of the interface is key to achieving defect-free heterovalent heterostructures. The geometry of the structure can also affect the bonding arrangement since thinner quantum wells with polar orientations can have charged interfaces close enough to affect each other, whereas the two interfaces of thicker double heterostructures can be electrically isolated [50]. To enable the full potential of heterovalent integration, the interface bonding and the III-V overgrowth on II-VI and IV-VI layers must be fully understood so that non-radiative recombination at the interfaces of these novel heterostructures can be suppressed.

From a quick glance at the band gap vs lattice constant relationship in figure 1, it is clear that the materials with larger lattice constants tend to have smaller band gaps. This presents an issue for isovalent epitaxial heterostructures since the energy band gap scales with the lattice constant and we are confined to only a small range of band gaps for a

specific isovalent material platform. This epitaxial limitation of isovalent heterostructures highlights the natural advantage of heterovalent heterostructures because the III-V semiconductors tend to have relatively narrow band gaps and higher conductivities due to the lower ionicity between the constituent atoms compared to the II-VI materials, as evident in figure 2. Because of this, the entire electromagnetic spectrum, from visible to far IR, can be covered by a single lattice-matched heterovalent heterostructure or material system [51]. Additionally, the higher ionicity and more insulator-like characteristics of the II-VI materials could also provide excellent insulating buffers or electron confinement layers for high-mobility III-V structures, which could enhance the current state of III-V transistors by reducing the electron leakage into the substrate or the gate and therefore enable new channel materials with high carrier mobilities. This could be tremendously beneficial for III-V semiconductors without any suitable lattice-matched isovalent barrier materials, such as InSb, which has the highest electron mobility of any known compound semiconductor but cannot be integrated into device structures because of its uncommonly large lattice constant [52]. Additionally, novel interface physics such as spin-orbit coupling or permanent electric fields due to the non-uniform charge distribution can possibly be harnessed for a variety of potential devices, as evident in figure 3 [42], [53]. Other optical properties, including a large refractive index contrast between epitaxially compatible II-VI and III-V materials, can be utilized to improve optical cavity devices by increasing the reflectivity and reducing the absorption and thickness of distributed Bragg reflector (DBR) structures [54]. A wide range of device structures based on these heterovalent DBRs have been proposed and modeled in this study to demonstrate the advantages of the enhanced flexibility with the available material properties when II-VI

and III-V semiconductors are combined. In this dissertation, the characterization techniques and the basic science behind them are discussed in section 2, followed by a discussion of the MBE growth system and processes in section 3. Section 4 covers the main body of work, including the heterostructure growths along with the characterization results and analysis. The potential for high-reflectivity heterovalent DBRs and mid-IR optical cavities are examined in section 5 before concluding with a summary in section 6.

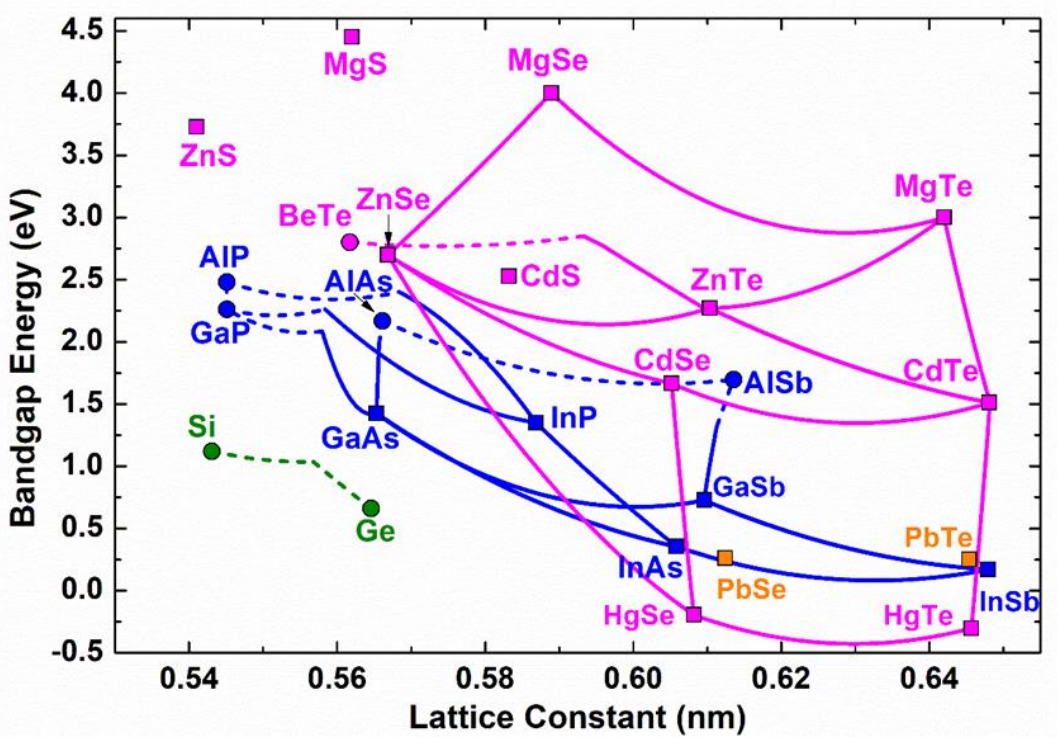

Fig. 1: Band gap energy vs lattice constant for common II-VI (pink), III-V (blue), IV-VI (orange), and group-IV (green) semiconductors and their alloys. The solid and dashed lines represent direct and indirect band gaps, respectively.

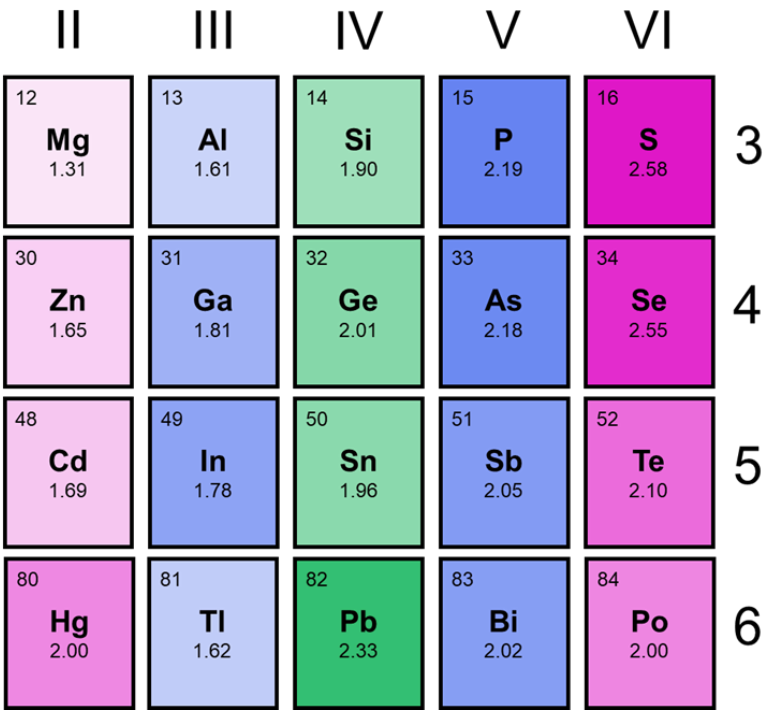

Fig. 2: Electronegativity comparison (in Pauling units) of the atoms commonly found in monocrystalline semiconductors. Larger differences in the electronegativity between the constituent atoms in the lattice will tend to result in a more insulator-like material, and higher atomic numbers will increase the lattice constant of the crystal.

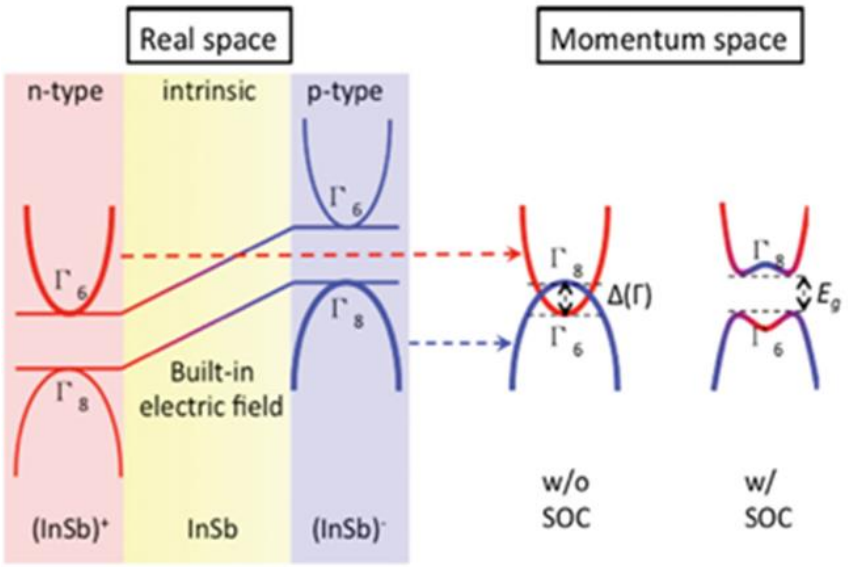

Fig. 3: Spin-orbit coupling in InSb superlattice layers induced by the built-in electric field formed from the Coulomb force of the polar (211) InSb/CdTe interfaces [42].

CHAPTER 2

SEMICONDUCTOR CHARACTERIZATION TECHNIQUES

Various characterization techniques have been used to obtain information about the semiconductor structures presented in this dissertation. Photoluminescence (PL) measurements were made using a couple of different spectroscopy methods to measure the emission and reflection profiles of samples for a range of relevant wavelengths. To measure wavelengths in the visible to near-IR, a grating spectrometer was used in combination with either a photomultiplier tube for emission in the visible band or a Ge photodetector for emission in the near IR. Dispersive systems such as grating spectrometers measure the sample spectrum by diffracting, separating, and scanning each individual wavelength using a network of gratings or prisms. The light hitting the grating inside the spectrometer is dispersed at different angles, and experiences constructive interference when equation 1 is satisfied.

$$Sin(\theta) = \frac{m\lambda}{d} \tag{1}$$

Where d is the slit spacing and m is the diffraction order. Clearly from this equation, the higher order diffraction harmonics must be filtered out to avoid erroneous measurements as, for example, the second order diffraction of light with a wavelength of 400 nm could be mistaken as the first order diffraction from light with a wavelength of 800 nm. This overlap can be avoided by using a long-pass filter in the path of the emitted light to ensure no higher-order diffraction peaks from high-energy signals corrupt the spectrum data. After the incoming light is dispersed by the gratings in the monochromator, it is then passed through a narrow slit in front of the detector to control the resolution of the system and to

separate the different wavelengths. The resolution of the system is determined by the superposition of the spectral width components of the emitted light, the optical system, and the spectrometer apparatus. The spectral width of the emitted light depends on the optical quality of the sample, as more defects in the lattice will introduce electronic states below the band gap energy and result in a wider spectral peak emitted from the sample. For the optical system, any diffraction or dispersion effects from the optics of the system can cause spreading of the measured signal linewidth. The spectral width of the laser emission can be factored into the linewidth spreading for the optical system as the deviation in photon energies can influence the observed emission profile. Additionally, the spectrometer apparatus contributes to the broadening of the observed spectrum from the linear grating dispersion and the finite slit widths in the spectrometer which decrease the spectral resolution at longer wavelengths. The slit width of the spectrometer can be narrowed to increase the resolution of the system, but the signal intensity will be reduced and a compromise between the resolution and the signal-to-noise ratio must be made. Since the dispersive system samples each wavelength individually through a narrow slit depending on the orientation of the internal gratings, the signal-to-noise ratio can only be increased by prolonging the sampling time or increasing the excitation density. The resolution of the system is determined by the groove density of the grating, and is inversely proportional to the wavelength. The resolving power required to distinguish two distinct features in a spectrum, which is also the inverse of the chromatic resolution, is given by equation 2.

$$R = \frac{\lambda}{\Delta\lambda} = mN \tag{2}$$

Where N is the grating density required to resolve features which are separated by a spacing of $\Delta\lambda$ at a wavelength of λ. From this equation, we can see that a higher resolving power is required for longer wavelengths, which in turn requires a higher density of grating grooves. Clearly, diffraction gratings work well for resolving relatively short wavelengths, but for longer wavelengths the grating density required to resolve closely-spaced peaks becomes unfeasible and therefore an interferometer is far more efficient and precise for this wavelength range.

For samples which emit at longer wavelengths, a Fourier transform infrared (FTIR) spectrometer equipped with either an InSb or HgCdTe detector was used to obtain the PL spectrum. A schematic of the FTIR measurement system is shown in figure 4. FTIR spectroscopy works by using an interferometer to simultaneously scan a range of wavelengths, which gives it a measurement speed advantage over dispersive spectroscopy and allows for high-precision IR measurements [55]. The incoming light is separated with a beam splitter before reflecting and recombining again at the separation point. The mirror in one of the beam paths is moved with a fixed velocity, and as the mirror moves and increases the beam path length, the different wavelengths present in the signal interfere with each other due to the optical path difference between the split beams to create a complex interferogram represented in the time domain. This interferogram can be interpreted as a spectrum of wavenumbers or energy through a Fourier transform which deconstructs the signal into the prevalence of its constituent frequencies to form the emission spectrum. Since the velocity of the mirror needs to be extremely precise, a reference signal from an internal HeNe laser source follows the same path as the incoming light and is used to calibrate the mirror speed. Careful attention must be paid to the system

settings, including mirror velocity and the lock-in time constant, to avoid spectral artifacts. The sampling rate of the FTIR system is determined by the mirror velocity, and therefore the velocity should be slow enough to avoid oversampling the incoming AC signal. Because FTIR spectrometers sample signals digitally, the signal must be sampled at a rate of twice its own frequency to deconstruct the waveform correctly. This is called the Nyquist frequency, and is explained in equations 3 and 4 where v_m is the velocity of the mirror and λ is the signal wavelength.

$$f_{Nyquist} = \frac{f_{meas}}{2} \tag{3}$$

$$f_{meas} = \frac{2v_m}{\lambda} \tag{4}$$

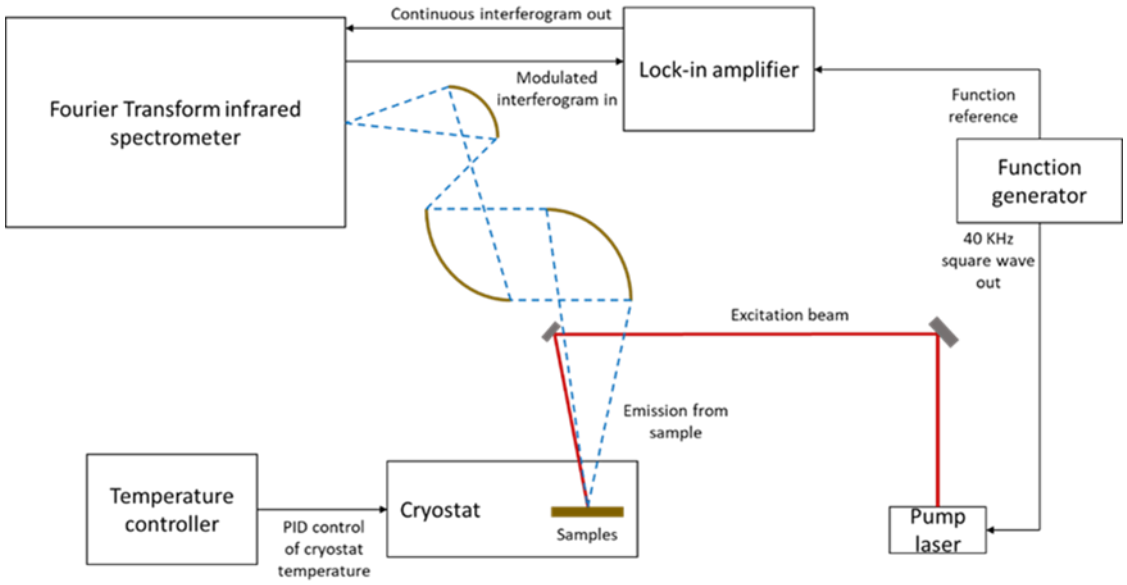

Fig. 4: Diagram of the FTIR equipment, optical setup, and beam path.

The throughput of the different spectrometer experiments was first measured to calibrate the emission spectrum measurements. A calibrated blackbody source was placed

at the focal point of the system and the emission from the source was measured for each setup. The real spectrum of the blackbody source, which is provided by the manufacturer, was then divided by the observed spectrum to obtain a normalized calibration curve, shown in figure 5, which gives the system's relative intensity as a function of wavelength. This calibration curve can then be multiplied by any observed spectrum to correct for the non-uniform throughput of the entire system, leaving the final spectrum free of any artifacts such as atmospheric absorption for IR measurements. The power density of each laser was determined using the blade-edge technique with a power meter to determine the spot size of the beam. Using this technique, a razor blade or cleaved wafer with a well-defined edge is positioned perpendicular to the beam path on a moveable stage with the edge of the blade facing perpendicular to both the direction of the stage movement and the beam path. The blade is then slowly and precisely moved to block a portion of the beam as the power meter reading is recorded. The measured intensity as a function of the blade position resembles an S-curve, and when integrated shows the Gaussian beam profile. The beam diameter is defined as the point where the integrated intensity reaches a value of $1/e^2$ of the peak intensity. This calculation is illustrated in figure 6 below.

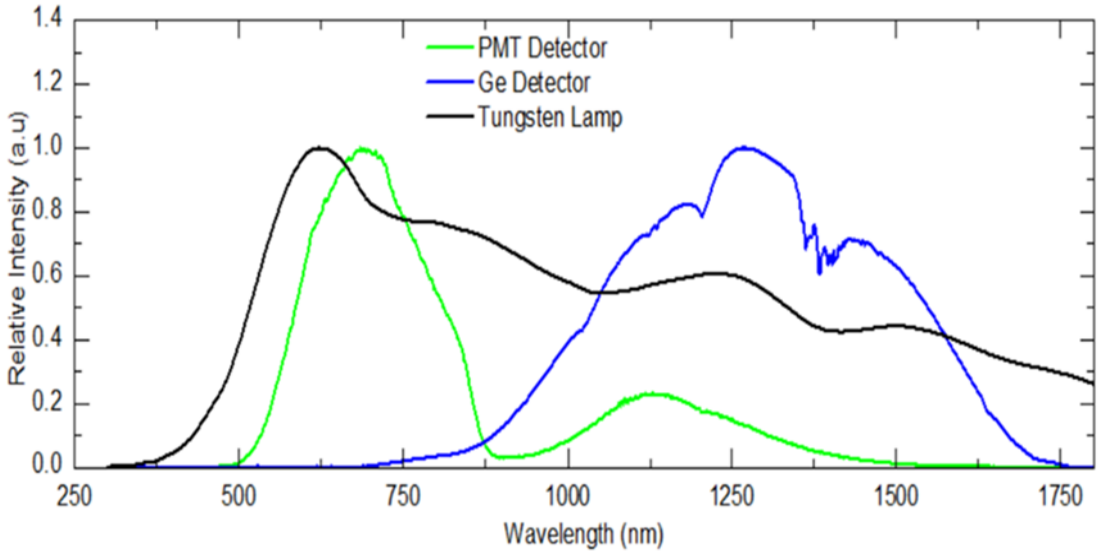

Fig. 5: Normalized throughput measurements for the grating spectrometer system observed with the two different detectors compared to the actual emission curve of the tungsten lamp.

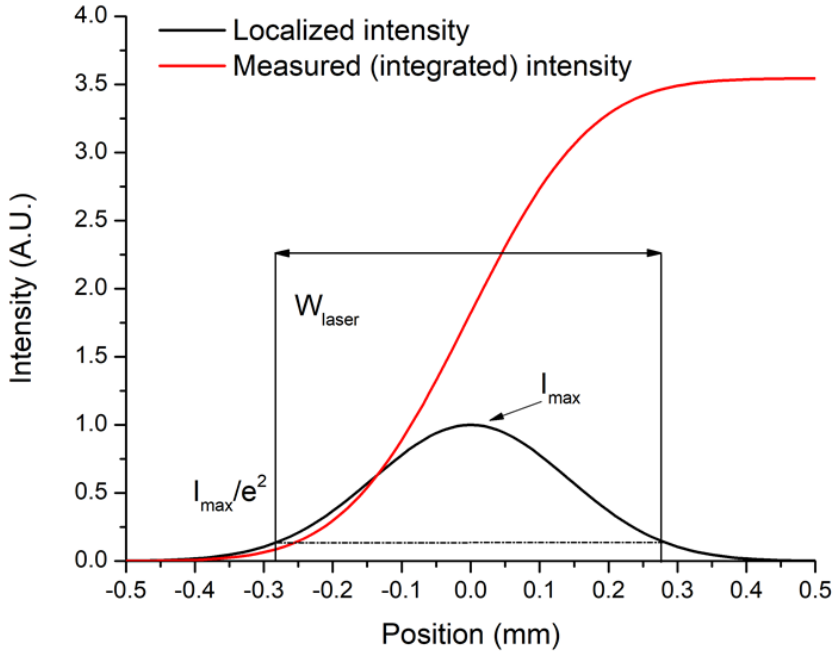

Fig. 6: Illustration of a typical Gaussian beam size measurement. The red curve is the measured intensity from the power meter, and the black curve is the intensity distribution in the blade's axis of movement.

In addition to optical emission measurements, FTIR spectroscopy was also utilized to study a variety of other optical material characteristics, such as the reflection and transmission profiles of samples. Reflection measurements were made using a vacuum-compatible Bruker IFS 66 FTIR system. The measurement setup for this system is comprised of a broadband mid-IR source, which emits near to longwave-IR wavelengths, a KBr beamsplitter, and a DTGS detector. A Seagull variable angle reflectance module was loaded with either a calibrated gold mirror for background spectral calibrations or the sample to be measured, then placed in the beam path in the evacuated sample chamber. The reflection spectrum of the sample was compared to the calibrated spectrum of the gold mirror to obtain the true reflectivity of the sample over a range of wavelength values. For these measurements, the aperture size and the sample size were carefully chosen to improve the overall reflectance measurement accuracy.

For measurements of the crystal structure of the samples, the close, periodic spacing of the crystal lattices allows for the diffraction of electromagnetic radiation with wavelengths on the order of the atomic spacing in the crystal. The structural characteristics of crystalline heterostructures, including the lattice spacing, layer thickness, defect density, and interface sharpness can all be determined from x-ray diffraction (XRD) measurements. Diffraction from the crystal planes is determined by the Bragg condition, described in equations 5 and 6.

$$2dSin(\theta) = m\lambda \tag{5}$$

$$d = \frac{a_0}{\sqrt{h^2 + k^2 + l^2}} \tag{6}$$

Where a_0 is the (001) lattice spacing and h, k, and l represent the direction of the atomic plane being measured. As the sample is tilted in the beam, the intensity is measured by an x-ray detector and plotted as a function of the incident angle. The electromagnetic waves experience interference as they are scattered by the atoms in the periodic crystal planes, which in turn determine the angle and intensity of the observed diffraction peaks [56]. In addition to the peak position and the lattice spacing, the interface between different materials will create a diffraction pattern, known as Pendellösung fringes, which can be used to determine the thickness of various layers using equation 7.

$$d = \frac{(m_i + m_j)\lambda}{2(sin\omega_i - sin\omega_j)} \tag{7}$$

Where m is the fringe order and λ is the wavelength of the x-ray source, which is 1.5406 Å for the Cu k-α source used for these experiments. From this equation, it is clear that the fringe spacing will decrease as the thickness of the layer increases. Figure 7 shows an XRD measurement of a CdTe/InSb heterostructure with prominent Pendellösung fringes. These fringes only appear when a sharp interface exists between the materials, and more prominent fringes can signify a good epitaxial quality between the two layers.

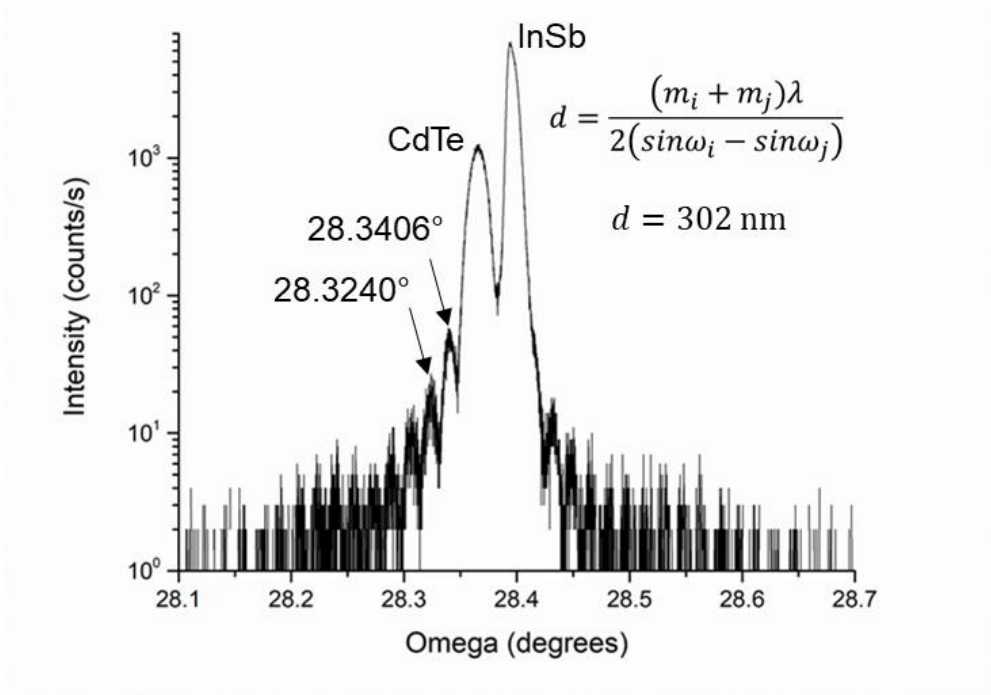

Fig. 7: XRD spectrum of a CdTe/InSb heterostructure with prominent Pendellösung fringes. The thickness of the layers can also be determined from the spacing of the fringes.

Not every angle which satisfies Bragg's law will produce a diffraction peak, as the unit cell of the crystal may be conducive to destructive interference for certain angles. Therefore, diffraction peaks for some atomic planes can be considered forbidden if the diffraction conditions cause equal-intensity signals with a 180° phase shift in the scattered beams. This is the idea behind structure-factor calculations, with which the diffraction conditions for a specific conventional unit cell can be calculated from the positioning of the atoms in the cell and the atomic scattering factors of the different elements. Structure-factor calculations can be useful for determining the crystal structure of a lattice since the relative intensity for each atomic plane can be calculated with a single equation. This is especially important for measurements of samples which contain multiple crystal structures, such as InSb/PbTe heterostructures. As an example, consider a zincblende unit

cell with atom A as the cation and B as the anion. From the coordinates of the atoms in the unit cell, we can calculate the expected beam interference as a function of the atomic scattering factor, *f*, which is related to the atomic number of the constituent element. The scattering factor is simply the ratio of the portion of the beam scattered by an atom compared to the portion scattered by a single electron, and therefore increases for heavier elements with higher atomic numbers. The structure factor of the unit cell, described in equation 8, is used to calculate the relative peak intensity for each atomic plane.

$$F = \sum^{N_A} f_A e^{2\pi i(uh+vk+wl)} + \sum^{N_B} f_B e^{2\pi i(uh+vk+wl)} \quad (8)$$

Where *u*, *v*, and *l* represent the atomic coordinates for each atom in the unit cell. Figure 8 shows the unit cell for a zincblende crystal, and from this schematic and table 1 it is clear that if the constituent atoms have similar scattering factors, i.e. similar atomic weights, then nearly complete destructive interference can be achieved for certain diffraction planes which would otherwise satisfy the diffraction condition. From equation 8, we can determine for which planes constructive or destructive interference should occur, and their peak intensities relative to each other which can help to determine the crystal structure of the sample. Figure 9 shows the rock-salt unit cell, and with table 2 the scattering conditions can be determined for any diffraction plane. Due to the change in atomic positioning in the unit cell, the two crystal structures have different diffraction intensities for angles corresponding to different atomic planes. Equations 9-10 show the final result of the structure factor calculations.

$$F(ZB) = \begin{cases} 4(f_A + f_B) & h + k + l = 4N \\ 4(f_A \pm i f_B) & h + k + l = 2N + 1 \\ 4(f_A - f_B) & h + k + l = 4N + 2 \end{cases} \quad (9)$$

$$F(RS) = \begin{cases} 4(f_A + f_B) & h, k, l = all\ even \\ 4(f_A - f_B) & h, k, l = all\ odd \\ 0 & h, k, l = mixed \end{cases} \quad (10)$$

From these equations, we can predict for which planes the crystal structures experience maximum constructive or destructive interference. For a binary zincblende semiconductor composed of elements with similar atomic weights (i.e. similar atomic scattering factors) such as InSb, then the planes which satisfy the destructive interference case will almost completely eliminate the diffraction peak. On the other hand, for rock-salt lattices, we can see that the case for constructive interference is slightly different than the zincblende condition but many planes, such as the (004) diffraction plane, will maximize constructive interference for both lattices. Some planes in the rock-salt lattice will also give perfect destructive interference regardless of the different atomic scattering factors. For heterostructures with non-uniform layers, the interfaces between the different materials can create observable features in the diffraction spectrum which can be analyzed to gather information about the sample. The individual diffraction peaks can also help determine the defect density from the width of the peak if the thickness of the layer is known, as the layer thickness also effects the peak width [57]. With more defects in the layer, the convolution of the form factor is not as strong due to the structural imperfections, and therefore the diffracted beam is spread out across a wider scan angle.

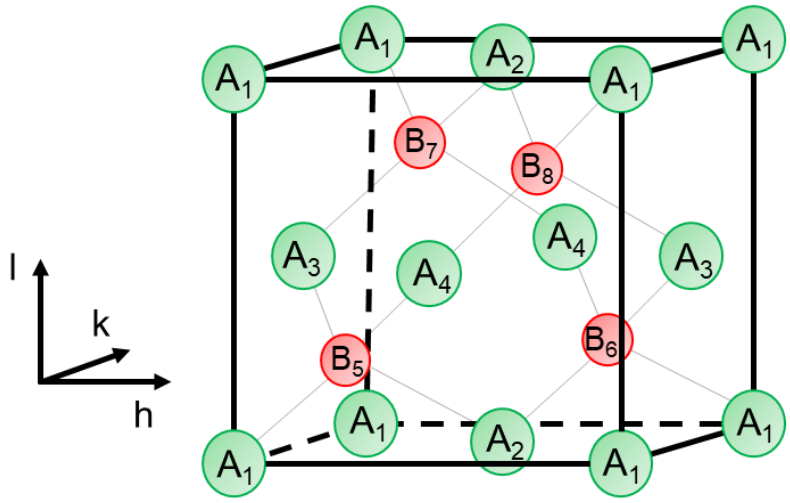

Fig. 8: A zincblende unit cell composed of elements A and B. Each element has four unique atoms in the unit cell, with 8 redundant corner atoms and 2 of each face-centered atom.

Table 1: Atomic ordering and diffraction conditions for the zincblende unit cell.

Zincblende

$X_{\#}$	(u,v,w)	$F = \sum f_x e^{2\pi i(uh+vk+wl)}$
A_1	(0,0,0)	$F_1 = f_A$
A_2	(½,½,0)	$F_2 = f_A e^{\pi i(h+k)}$
A_3	(0,½,½)	$F_3 = f_A e^{\pi i(k+l)}$
A_4	(½,0,½)	$F_4 = f_A e^{\pi i(h+l)}$
B_5	(¼,¼,¼)	$F_5 = f_B e^{\frac{1}{2}\pi i(h+k+l)}$
B_6	(¾,¾,¼)	$F_6 = f_B e^{\frac{1}{2}\pi i(3h+3k+l)}$
B_7	(¼,¾,¾)	$F_7 = f_B e^{\frac{1}{2}\pi i(h+3k+3l)}$
B_8	(¾,¼,¾)	$F_8 = f_B e^{\frac{1}{2}\pi i(3h+k+3l)}$
$F = f_A[1+(-1)^{h+k}+(-1)^{k+l}+(-1)^{h+l}] + f_B[i^{h+k+l}+i^{3h+3k+l}+i^{h+3k+3l}+i^{3h+k+3l}]$		

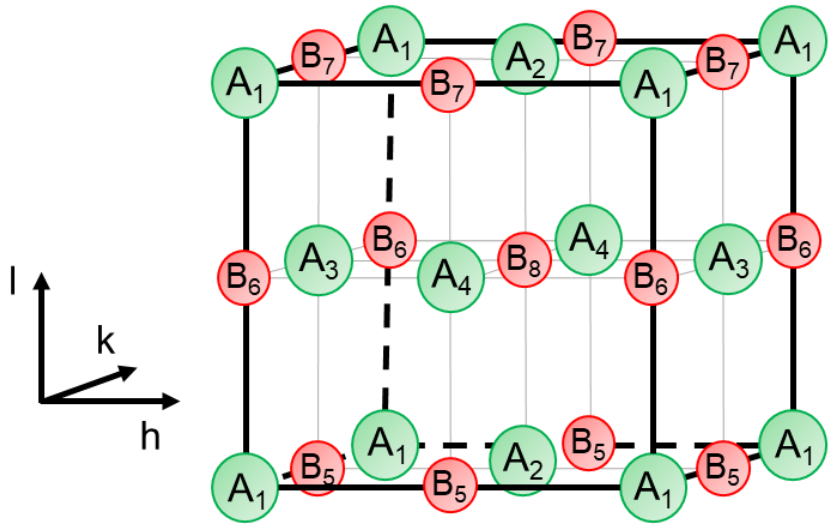

Fig. 9: A rock-salt unit cell composed of elements A and B. The structure is similar to the zincblende crystal, but the B atoms are in the same plane as the A atoms which contrasts the zincblende structure.

Table 2: Atomic ordering and diffraction conditions for the rock-salt unit cell.

Rock-salt

$X_{\#}$	(u,v,w)	$F = \sum f_x e^{2\pi i(uh+vk+wl)}$
A_1	(0,0,0)	$F_1 = f_A$
A_2	(½,½,0)	$F_2 = f_A e^{\pi i(h+k)}$
A_3	(0,½,½)	$F_3 = f_A e^{\pi i(k+l)}$
A_4	(½,0,½)	$F_4 = f_A e^{\pi i(h+l)}$
B_5	(½,0,0)	$F_5 = f_B e^{\pi ih}$
B_6	(0,0,½)	$F_6 = f_B e^{\pi il}$
B_7	(½,0,1)	$F_7 = f_B e^{\pi i(h+2l)}$
B_8	(½,½,½)	$F_8 = f_B e^{\pi i(h+k+l)}$
$F = f_A[1 + (-1)^{h+k} + (-1)^{k+l} + (-1)^{h+l}] + f_B[(-1)^h + (-1)^l + (-1)^{h+2l} + (-1)^{h+k+l}]$		

In addition to post-growth characterization, in-situ methods for obtaining real-time information, such as reflection high-energy electron diffraction (RHEED) and optical pyrometry, were also utilized to observe the surface conditions during the growth process. RHEED uses a high-energy electron beam reflected at a grazing incidence to observe the diffraction pattern from the reconstructed crystal surface, and can be used to determine the flux conditions and growth rate. RHEED is a powerful tool only available for growth techniques which utilize ultra-high vacuum (UHV) growth conditions, as the electrons need to travel from the RHEED gun to the projection screen without interacting with other particles. The surface reconstruction of the crystal's dangling electrons and their interaction with the vacuum environment can be interpreted from the diffraction pattern on the projection screen. The reconstruction will change if the dangling electron bonds or atomic positions along the surface are rearranged, which can happen under different temperature or flux conditions. RHEED can be used to determine the surface conditions by monitoring the reconstruction shift that can occur if a certain elemental species is prevalent on the surface or if a specific temperature has been reached. Figure 10 illustrates a RHEED oscillation measurement, which tracks the intensity change of the diffraction pattern at a selected spot on the phosphorous screen, and can determine the growth rate by monitoring the periodic change in the intensity [58]. For layer-by-layer growth, the diffracted signal will be strongest when the surface is completely flat and weaker when adatoms have incorporated onto about 50 % of the surface, resulting in a periodic intensity fluctuation which can be interpreted as the growth rate of the material. In addition to the growth rate and surface reconstruction, the growth temperature must also be closely monitored to achieve high-quality material growth. The thermocouple of the substrate

manipulator only measures a relative temperature which can change depending on the wafer holder's material and geometry, the substrate thermal conductivity, and the growth chamber conditions such as the effusion cell temperatures, so an accurate method of reading the substrate temperature is needed to obtain repeatable results. Optical pyrometers satisfy this requirement as they can accurately measure the substrate temperature without contacting the growth surface by observing the gray body radiation at a specific wavelength, and therefore only the emissivity of the material must be specified to determine the temperature. This technique works well for most semiconductor materials, but not for other common substrates such as glass and sapphire which are transparent to a significant portion of the IR spectrum. Additionally, the pyrometer reading can be altered if the optics are out of focus, the emissivity setting is incorrect, the substrate is small, or if the observation window gets coated. This can lead to an incorrect growth temperature reading and inadequate growth conditions, and therefore the pyrometer equipment must be checked and calibrated often during a growth campaign to ensure consistent growth conditions.

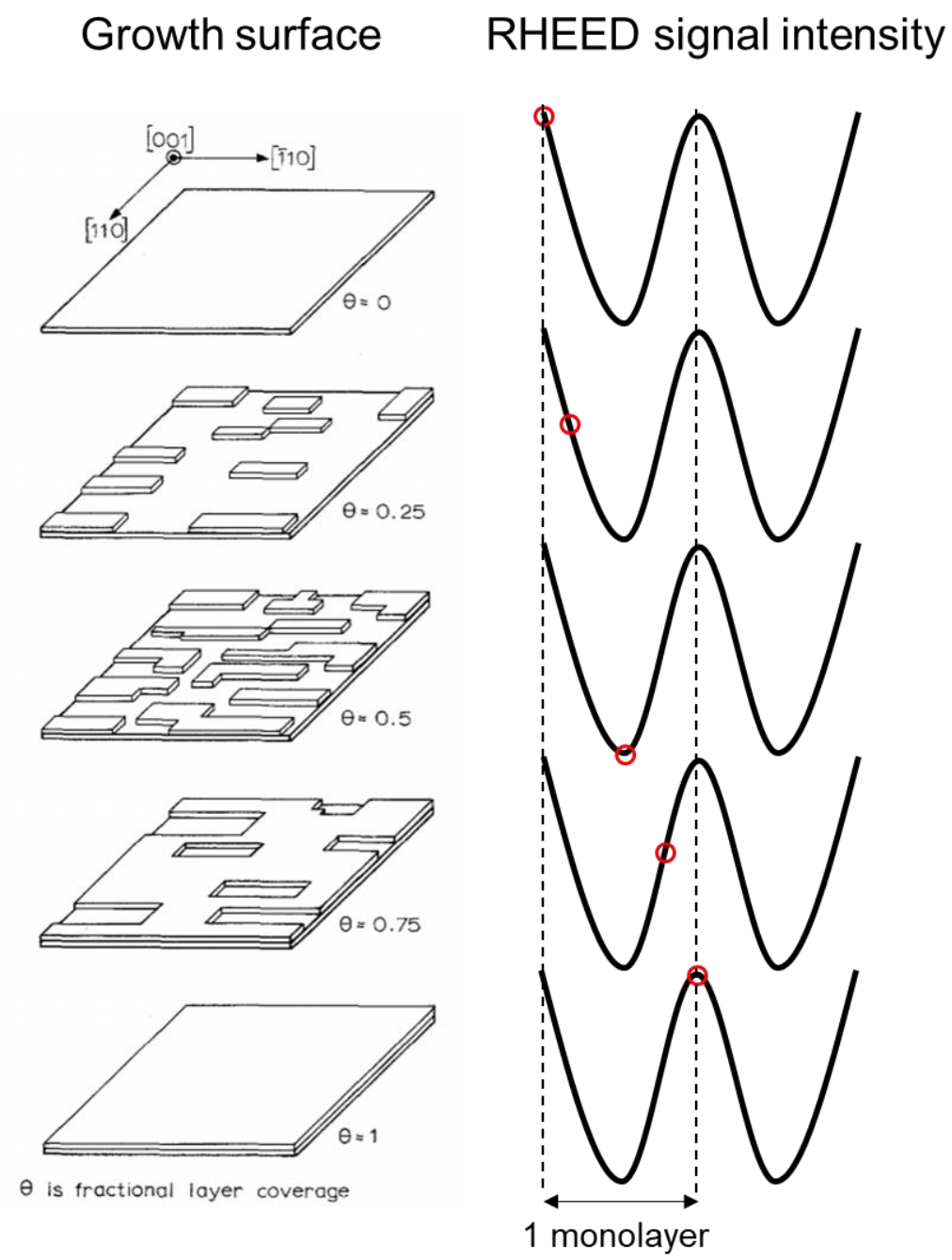

Fig. 10: Illustration of how adatoms covering the growth surface effect the RHEED signal intensity, enabling the RHEED oscillation technique for growth rate measurements [58].

CHAPTER 3

MBE GROWTH AND OPTIMIZATION OF GROWTH CONDITIONS

Heterovalent heterostructures were primarily grown in a novel single-chamber VG-V80 molecular beam epitaxy (MBE) system, shown in figure 10, equipped with effusion cells containing group II, III, IV, V, and VI elemental sources. Heterovalent quantum structures composed of GaAs/ZnSe, GaSb/InAs/PbSe/CdSe/ZnTe, and InSb/PbTe/CdTe were grown in this system [59], [60] and characterized with transmission electron microscopy (TEM), XRD, and PL. Combining materials with significantly different properties into one growth chamber has historically been avoided as one material system can act as an unintentional dopant for another [61], and only one other group has reported results from heterovalent samples grown in a single-chamber MBE system [62]. The evaporated source material can also coat any surfaces inside the chamber, which can cause problems if the temperature of any of those surfaces is raised by a nearby source of heat such as an ion gauge or effusion cell. Additionally, due to the large variation in vapor pressures between the different source materials, a range of cell temperatures are required for operation. A material with a low vapor pressure will need a very hot effusion cell for evaporation, but this may lead to uncontrolled evaporation of the high vapor pressure material from the surfaces of the chamber. The placement of the different cells in the 8 cell ports on the growth flange is therefore critical for minimizing the effect of unintentional evaporation in the heterovalent growth chamber. The single growth chamber design was chosen because it allows for the investigation of the interface properties between these materials in more detail and enables experiments with growth conditions and material combinations that are impossible with a dual-chamber growth system. In the

current configuration, the growth chamber is equipped for growth of Cd, Zn, Ga, In, Pb, Sn, Sb, As, Te, and Se, with eight material sources being available at a time, as shown in figure 11. Other sources such as Ge, Mg, Al, or Bi could be swapped out if there exists a clear benefit to changing the material combinations for the next growth campaign.

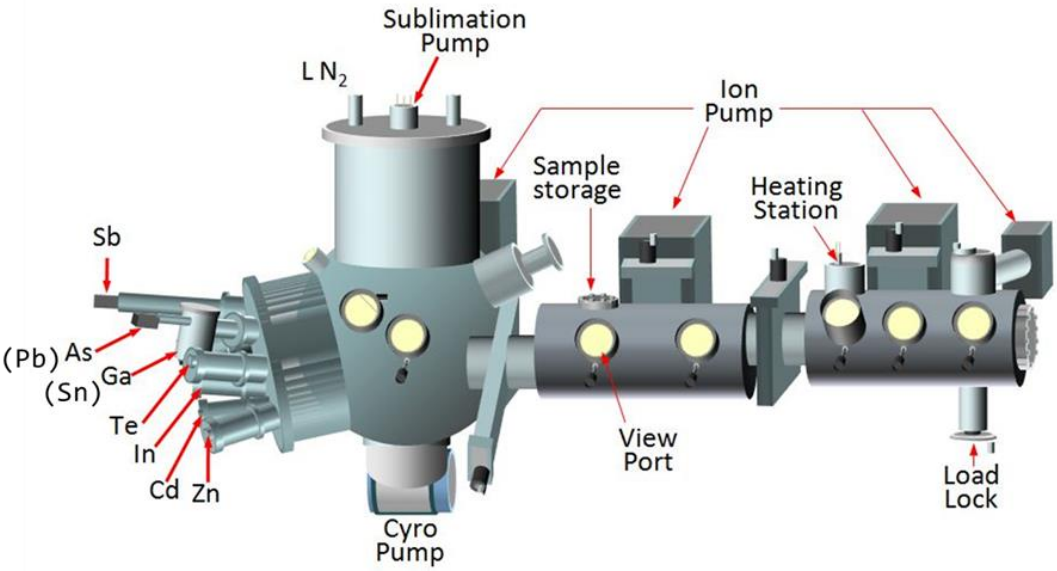

Fig. 11: Diagram of the single-chamber heterovalent VG-V80 MBE growth system.

The pre-owned VG-V80 MBE system was previously used for HgCdTe detector growth and was purchased to be retrofitted for a range of III-V and II-VI material systems. New effusion cells and vacuum pumps were added to the system, along with an entirely new N2 manifold and vent apparatus, water delivery system, pneumatic shutter lines and shutter controller, RHEED gun and monitoring software, control computer and software, residual gas analyzer, power supplies, liquid nitrogen delivery system, and PID temperature controllers. A significant amount of mercury had to be removed from the growth chamber, and trace amounts of mercury outgassing is seen on the mass spectrometer when the chamber walls are baked at 200 °C. Under normal operating

conditions no Hg is detected in the chamber or in any of the samples, certifying that the Hg outgassing is not an issue with any of the growths.

Other heterovalent heterostructures were grown in a dual-chamber MBE system with dedicated III-V and II-VI V80 growth chambers connected under UHV conditions by a transfer chamber. This setup is ideal for II-VI growth on III-V substrates, but the potential risk of cross-contamination from II-VI materials in the III-V growth chamber limits the possible structures available to be grown in this system. The issue of cross contamination is best illustrated by plotting the vapor pressure curves of the different materials, as shown in figure 12, where the II-VI materials clearly evaporate at much higher rates than the group-III elements such as In and Ga. This can cause uncontrolled evaporation from surfaces inside the chamber near the hot group-III effusion cells. Additionally, the separate growth chambers hinder the ability to test different interfacial growth conditions between the II-VI and III-V layers. Therefore, the dual-chamber system was rarely used for the III-V growth on II-VI layers once the single-chamber system was online.

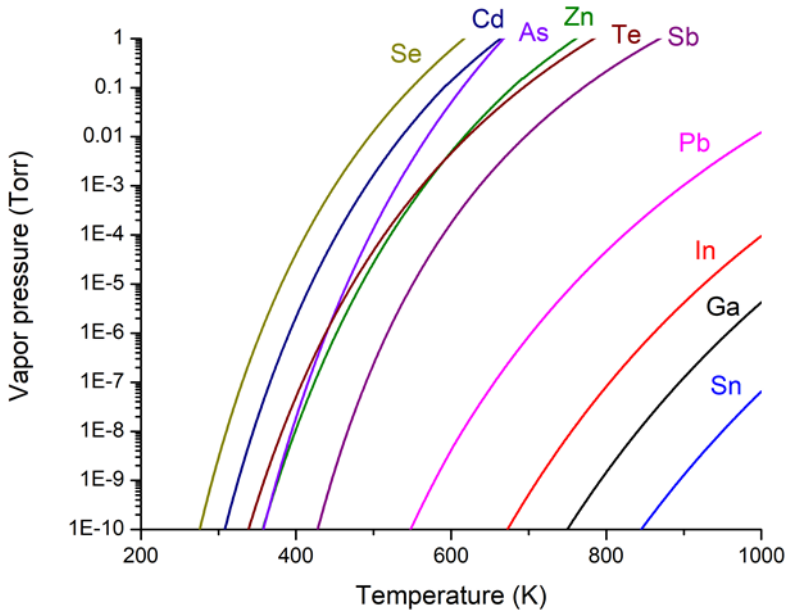

Fig. 12: Vapor pressure curves of various elements used for epitaxial growth of heterovalent heterostructures.

Calibration of the III-V growth conditions was first performed for GaAs, InAs, GaSb, and InSb. The beam equivalent pressure (BEP) of the cells was measured with a retractable ion gauge centered in front of the substrate manipulator and then correlated to the thermocouple temperature reading of the effusion cell, which can be directly related to the growth rate for the group-III sources or the V/III flux ratio for the group-V sources. To complete the group-V flux calibrations, the surface reconstruction was monitored during growth as the group-V flux was decreased to find the stoichiometry point where the actual flux ratio is unity, noted by a shift in the reconstruction pattern due to the change in the surface chemistry. This method for finding the V/III flux ratio is possible because the group-V atoms will not typically incorporate into the crystal at standard growth temperatures without a group-III element to bond with [63]. Therefore, III-V materials can

be grown at a V/III flux ratio higher than unity with a negligible effect on the material properties. To find the growth rate, which is determined by the group-III elemental flux under excess group-V flux conditions, RHEED oscillation and XRD analysis of the Pendellösung fringes as described earlier was used. Once the growth rate is known for a group-III cell temperature and BEP flux, the growth rate can then be extrapolated for a range of cell temperatures using the BEP flux-temperature curves.

For II-VI materials, the growth conditions are slightly more complicated to determine since these materials can be grown epitaxially with either an excess flux of group-II or group-VI atoms. Therefore, unlike with III-V materials, the growth rate does not plateau when the flux ratio reaches unity but instead just enters a different growth regime. A shift between group-II rich and group-VI rich growth conditions can be determined by the RHEED surface reconstruction. With an excess group-VI flux, the surface is reconstructed into a (2×1) diffraction pattern. If the group-II flux is increased to the point where it overcomes the group-VI flux, the excess group-II atoms on the surface create a c(2×2) reconstruction pattern [64]. Additionally, the growth rate trend should shift as the group-II cell temperature is increased beyond the stoichiometry point as less atoms will stick without Te atoms available to bond with, and therefore the slope of the growth rate compared to the cell temperature will be lower as the cell temperature is raised past the stoichiometry point as shown in figure 13. The point where the surface reconstruction shifts and the growth rate vs cell temperature trend slows signifies a II/VI flux ratio of unity for a specific growth temperature.

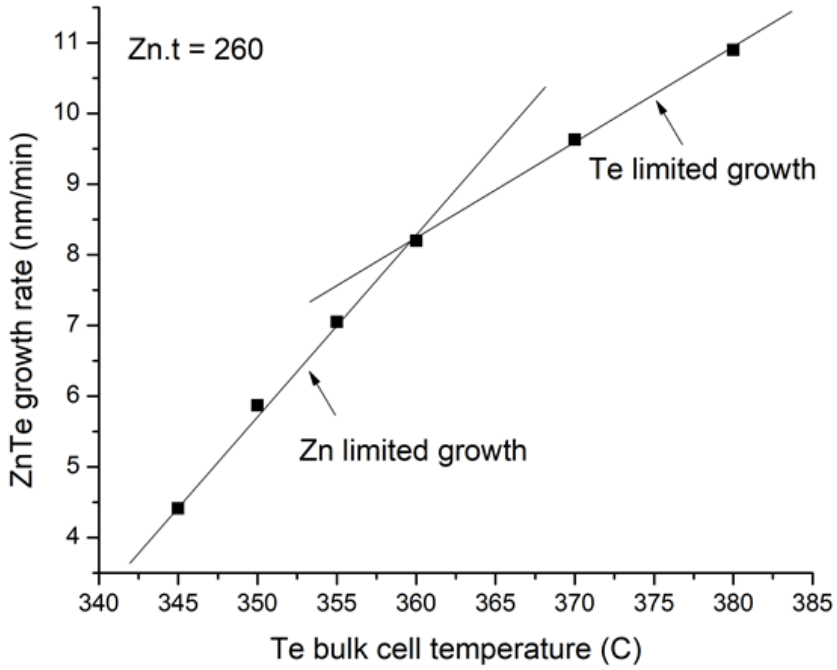

Fig. 13: ZnTe growth rate measured as a function of the Te effusion cell temperature at a substrate temperature of 280 °C. The point where the slope changes is defined as the stoichiometry point for ZnTe.

In addition to the flux conditions and substrate temperature, heterovalent heterostructures require precise control over the interface conditions since the mismatched electron sharing between the interface atoms can cause interfacial defects or III_2VI_3 compounds to form instead of a high-quality zincblende crystal structure [65]. The prevalence of these defective compounds at the interfaces between III-V and II-VI materials is due to the group-VI atoms' propensity to displace group-V atoms from the III-V surface [66], [67] and the low formation energy of III_2VI_3 compounds compared to covalent bonds with 9 electrons shared between the group-III and group-VI atoms at the interfaces [68]. This case can be compared to II-V interface bonds, which have more

favorable formation energies to retain the zincblende crystal structure. Therefore, bonding between group-II and group-V atoms at the interface must be promoted using specific flux conditions between the growth of III-V and II-VI materials to retain a consistent epilayer quality and coherent crystal structure [69].

While typically the positively-charged interfaces seem to work best for II-VI/III-V single-interface heterostructures, the buildup of charge at the interface could possibly affect the interface bonding condition if multiple interfaces are placed in close proximity, as the positively or negatively-charged interfaces could interact in thin layers and set up a built-in electric field which would alter the formation energies of the different interface structures. To suppress the III-VI bonding at the interface, a soak of group-V and group-II elements was applied after the growth of one layer and before the start of the next different material. The substrate temperature during the elemental soak should ideally be set so that only a single layer of atoms will stick to the surface, and the rest are desorbed instead of incorporating into the crystal. The difference between a group-II and group-VI terminated interface is clearly apparent in the straightforward case of ZnTe grown on nearly lattice-matched (100) GaSb substrates. Characterization of the two samples show that a 30-second Zn overpressure before the start of the ZnTe growth results in a coherent ZnTe layer, whereas a 30-second Te overpressure destroys the crystal quality of the interface and the subsequent ZnTe epilayer. This phenomenon is shown in the TEM images in figure 14 for the ZnTe/GaSb interface, and has been noticed in all of the II-VI/III-V material combinations discussed here.

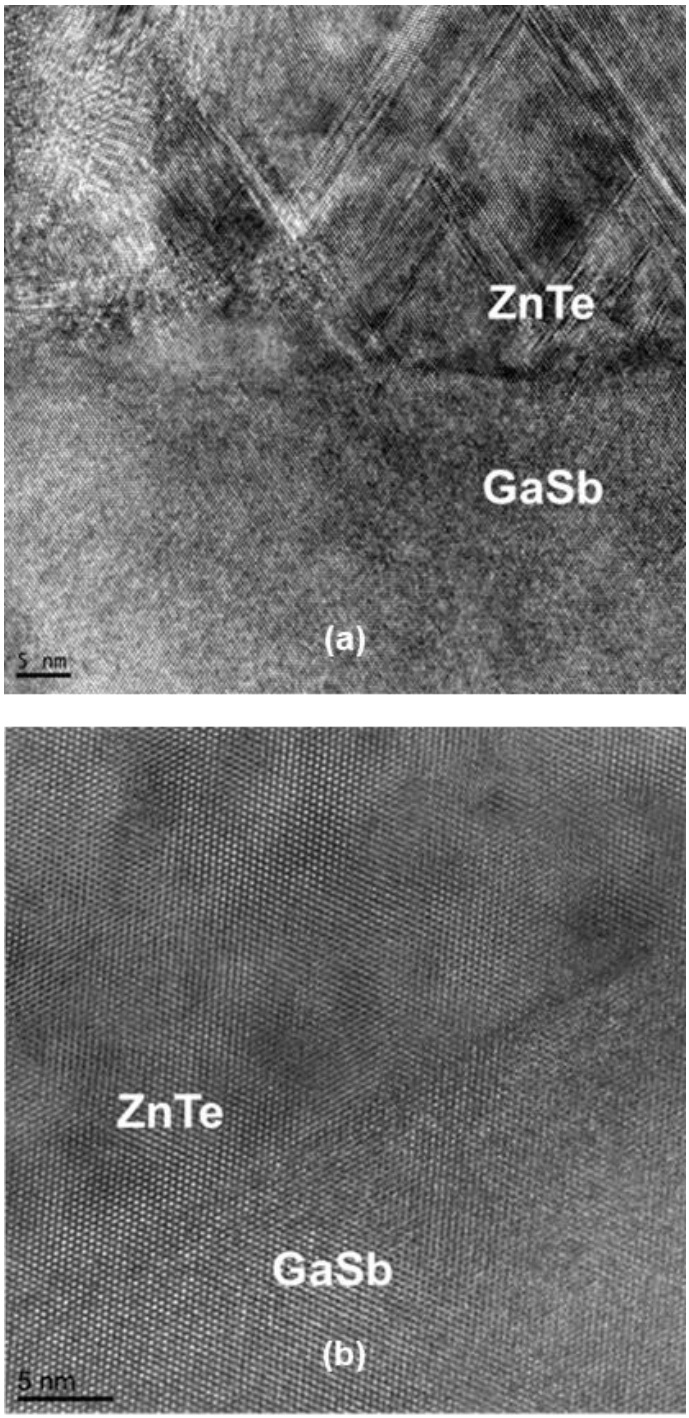

Fig. 14: TEM images of ZnTe grown on GaSb with 30 seconds of Te flux (a) and 30 seconds of Zn flux (b) prior to the ZnTe layer growth. Sample prep and imaging performed by Dr. Brian Tracy.

The high vapor pressure and weak bond strength of the II-VI crystals complicates the growth of III-V films on II-VI layers, as the required growth temperatures for high-quality III-V films can cause the underlying II-VI layers to desorb or diffuse into the III-V layers. Therefore, to accommodate the II-VI materials in the structure, the III-V layer may be grown at a significantly reduced substrate temperature to protect the II-VI layer from being destroyed. This not only reduces the diffusion length of the adatoms which can introduce stacking faults and other defects into the lattice, but the flux ratio will also change as the group-V desorption rate is temperature-dependent so the V/III ratio can increase as the substrate temperature is reduced.

To avoid these problems and obtain high-quality growth of thin III-V layers on II-VI materials, migration-enhanced epitaxy (MEE) can be used to increase the diffusion length of the surface adatoms at relatively low temperatures by alternating the group-V and group-III fluxes. Precise control of the elemental flux from both the group-III and group-V sources must be tightly controlled to achieve an acceptable level of material quality, and the flux should be alternated after every monolayer of atoms is deposited. The growth rate, surface temperature, and the adatom relaxation time where no flux is present on the surface must all be optimized to obtain the highest-quality material at low temperatures. Naturally, this takes an immense amount of time and precise equipment, and therefore these parameters have only been calibrated to a level where acceptable material quality can be achieved in both antimonides and arsenides. As an example, the migration-enhanced As and Ga shutter sequence for GaAs growth is illustrated in figure 15. With MEE, the shutters for the group-III and group-V materials were modulated to deposit a single monolayer of atoms on the surface at a time. A short delay between closing one shutter

and opening the other was implemented to allow the adatoms to diffuse across the surface and incorporate into the crystal before the deposition of the next monolayer. By using this technique at low growth temperatures, high-quality III-V films which demonstrate band-to-band optical transitions can be grown on II-VI layers.

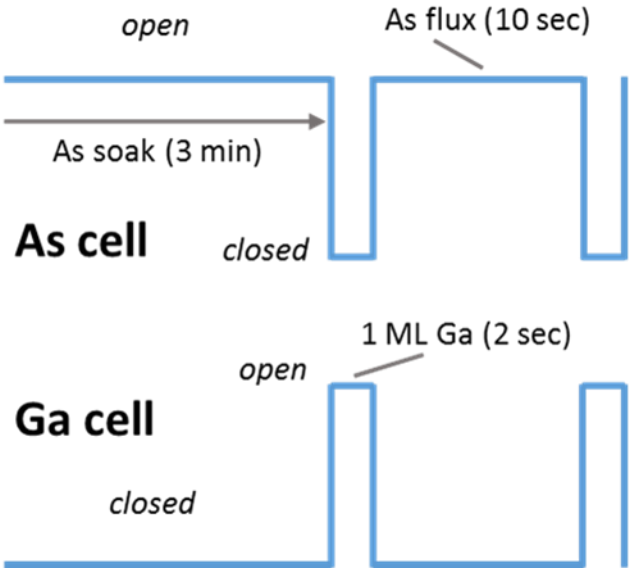

Fig. 15: Illustration of the migration-enhanced shutter sequence for low-temperature GaAs growth. With this technique, the surface is exposed to alternating group-III and group-V elemental fluxes to increase the diffusion length of the adatoms on the growth surface.

The viability of MEE is much improved for group-V atoms with a low sticking coefficient due to the imprecise nature of the V/III flux calibrations for low growth temperatures. A low sticking coefficient simplifies the deposition of a single monolayer of material, as any excess atoms will have trouble building up on the surface without a crystal site to bond to. Therefore, As-containing III-V semiconductors have an advantage for low-temperature growth compared to Sb-containing materials since Sb can build up at the surface and cause severe problems without a precise V/III ratio. Even with this issue, Sb-containing materials are possible to grow with MEE and still show a dramatic

improvement in the PL quality and defect density compared to samples grown with no modulation at low temperatures. Under similar growth conditions, a sample grown with simultaneous Ga and Sb fluxes has significant structural issues as evidenced by a diffuse RHEED reconstruction during growth and an indistinguishable XRD pattern. On the other hand, the samples grown with an alternating Sb and Ga shutter sequence consistently produce much narrower GaSb XRD peaks with streaky RHEED reconstructions suggesting coherent, flat interfaces between the GaSb and ZnTe layers. The uneven interfaces seen in these studies are likely caused by the low substrate temperatures during the epilayer deposition as the surface adatoms have insufficient thermal mobility to migrate across the lattice and find a step to incorporate, but instead they supersaturate on the surface and form three-dimensional islands. Additionally, the group-V flux conditions affect the group-III diffusion length and therefore the V/III flux ratio must be close to unity to achieve layer-by-layer growth [70]. The different epitaxial growth modes are illustrated in figure 16, and while the layer-by-layer, or Frank-van der Merwe growth mode, is ideal, epitaxial growth typically occurs under either the Volmer-Weber or Stranski-Krastinov growth mode.

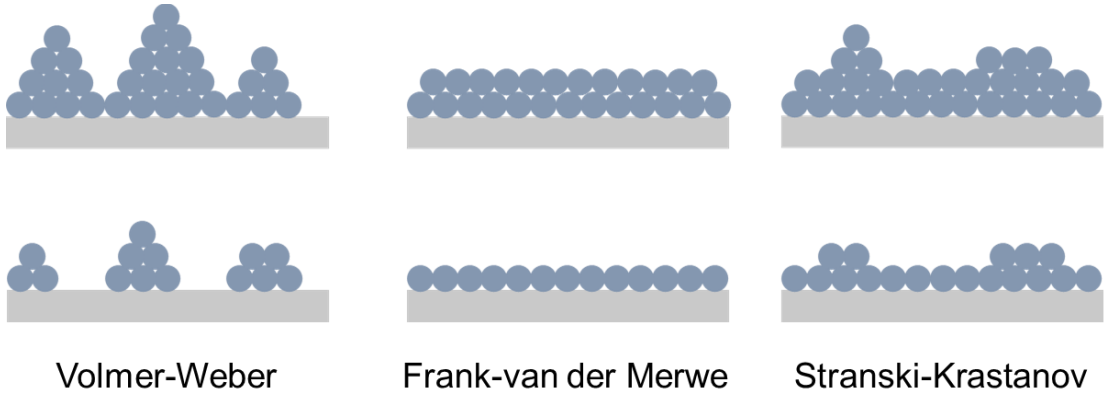

Fig. 16: Illustration of epitaxial growth modes, including island formation (Volmer-Weber), layer-by-layer (Frank-van der Merwe), and layer-plus-island (Stranski-Krastanov).

For heterovalent structures with relatively thick III-V layers such as double heterostructures or DBRs, a substrate temperature ramp can be utilized to improve the material quality of the III-V layer as it is grown on the II-VI layer. With this method, the III-V growth is started while the substrate temperature is still at the II-VI growth temperature to keep the II-VI surface from desorbing. While the III-V material grows, the substrate temperature is rapidly increased and the material quality of the III-V layer, as determined by the RHEED reconstruction, improves. Even with the II-VI layer protected by a thin III-V film deposited at a low temperature, the substrate temperature still must be kept low enough to minimize diffusion between the III-V and II-VI layers, as seen in table 3, so typically the maximum growth temperature is still lower than the ideal III-V growth temperature as the maximum temperature depends on the thermal energy required to break the bonds in the II-VI crystal. For the II-VI temperature stability, it was found that Zn-containing materials tend to have a higher temperature tolerance (around 500 °C) compared to Cd-containing materials which tend to create relatively more defects at lower substrate temperatures. We can therefore seek to select material combinations with acceptable III-V growth temperatures lower than the temperatures where the II-VI materials become unstable, such as GaSb and ZnTe, for the best heterovalent heterostructure results. High-quality heterovalent heterostructures with strong PL emission and prominent Pendellösung fringes can be obtained with the temperature ramp method if the III-V layer is sufficiently thick, but issues still persist for thinner layers grown using this technique.

Table 3: Growth and desorption temperatures for various lattice-matched heterovalent material combinations.

Material (III-V / II-VI)	III-V growth temp (°C)	II-VI growth temp (°C)	II-VI desorption temp (°C)
GaAs / ZnSe	600	300	500
InAs / CdSe	450	280	460
GaSb / ZnTe	500	300	>500
InSb / CdTe	390	280	300

While the growth temperature mismatch can be a problem for III-V/II-VI integration, the IV-VI layers can be grown at substrate temperatures similar to the II-VI materials. This enables narrow-band gap semiconductors to be incorporated with the II-VI barrier layers into heterostructures on a single lattice-matched III-V substrate. Elemental Pb and Te sources were used for the growth of PbTe on lattice-matched InSb substrates, often with adjacent CdTe barrier layers. BEP flux ratios between the Pb and Te were varied over an order of magnitude to determine the ideal growth conditions for PbTe on InSb and CdTe, and a high Pb/Te flux ratio of over 10:1 was required to achieve growth rates on the order of 5 nm/min. Additionally, the ideal interface flux conditions were found to vary depending on if the PbTe was grown on InSb or CdTe layers, with a 30 second Te flux favored for PbTe growth on InSb compared to a Cd interface flux for layers grown on CdTe.

For non-polar substrate orientations such as the (100) plane, the atomic species on the surface can be mixed and the interfaces are not charged. This contrasts polar orientations such as the (211) or (111) facets, as illustrated in figure 17, where charge neutrality for compound semiconductors dictates the surface termination since the bottom

surface is terminated with either a cation or anion only. Therefore, heterovalent interfaces in polar structures can experience a significant buildup of charge due to the complete termination of the surface by a single element, and this Coulomb energy can alter the interface bonding arrangement. These polar-oriented heterovalent heterostructures are of great interest when combined with the prospect of monolithic integration. Non-polar orientations do not have anything other than the growth flux to determine the interface termination, and therefore the (100) orientation can possess either an interface terminated with two elements or a charge-neutral mixed interface with atoms from both materials along the interfacial plane. Additionally, the formation energy of different bonding arrangements will change with different substrate orientations, possibly allowing for alternately-charged quantum well interfaces and superlattices. Currently, this is difficult with non-polar orientations due to the issues associated with achieving III-VI terminated interfaces without forming defective compounds between the materials. This could change for a polar interface configuration, as the zincblende structure formation energy could be lower when influenced by an oppositely-charged zincblende interface, which would make the III-VI terminated interface more stable for the zincblende structure.

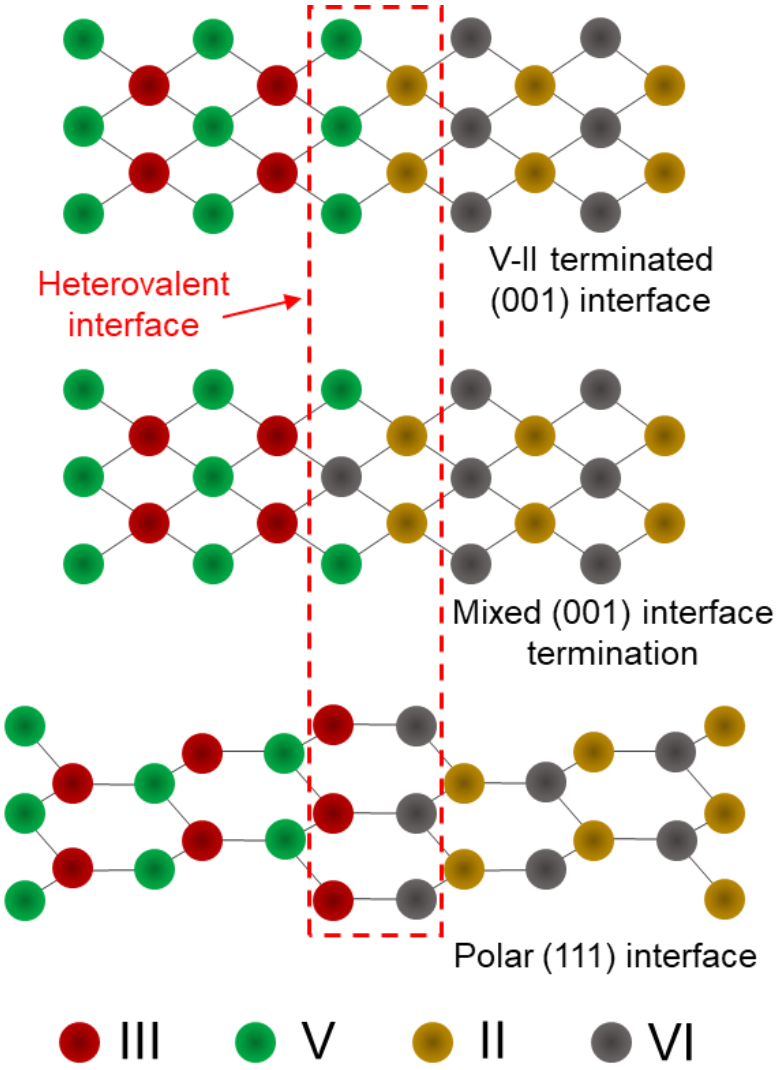

Fig. 17: Heterovalent interface termination and atomic ordering at polar and non-polar interfaces.

Growths of heterovalent heterostructures on substrates with polar orientations were investigated due to the more predictable interface configuration, the strong polar charge at the heterovalent interfaces, and the prospect of achieving new virtual substrates for HgCdTe IR detectors which are currently fabricated on extremely small, expensive (211) $Cd_{0.96}Zn_{0.04}Te$ substrates. Since InSb is closely lattice-matched to these materials, (211)B

InSb substrates were used to explore the prospect of PbTe, CdTe, or CdZnTe growth in this orientation. For HgCdTe IR focal plane arrays, the dislocation density needs to be kept as low as possible to maximize the detectivity and minimize the dark current from defect generation in the device. This starts with the substrate defect density, which can be compared from the FWHM of the XRD peak. The main issue with these virtual substrates is the oxide desorption of (211) InSb, which usually takes around 2 hours to complete, and the precise control of the growth conditions required at the interface which can significantly reduce the quality of the II-VI layer if not calibrated properly. Work on the polar InSb/CdTe heterostructures on (211) substrates has been under investigation alongside the non-polar InSb/CdTe structures on (100) substrates.

CHAPTER 4

HETEROVALENT HETEROSTRUCTURES

III-V layers confined by nearly lattice-matched II-VI barrier layers, including GaAs/ZnSe, GaSb/ZnTe, and InSb/CdTe heterostructures were grown on III-V substrates and the growth conditions were optimized, particularly at the interfaces between the materials, over a number of sample runs. Lead chalcogenide IV-VI materials were also integrated with their lattice-matched zincblende counterparts into heterocrystalline heterostructures. Growth conditions, including the growth rates, flux ratios, interface conditions, and substrate temperatures were altered to achieve thin layers with heterovalent and heterocrystalline interfaces in close proximity. The double heterostructures, quantum wells, and superlattices were characterized to quantify the electrical, optical, and structural properties of the crystal.

4.1 GaAs/ZnSe heterostructures

Since the GaAs/ZnSe material system has a wealth of published data and growth methods available due to the blue-green LED push a few decades ago [71], heterostructures comprised of these materials were the first attempted growths after bringing the single-chamber MBE system online. Although the integration of GaAs and ZnSe has been investigated far more than any of the other lattice-matched III-V/II-VI material systems, the growth temperature difference between these two materials is much larger than any of the other material combinations discussed in this dissertation, as shown in figure 18. This complicates the growth of the GaAs layers confined by ZnSe as the GaAs growth needs to be performed at a significantly lower substrate temperature, which can introduce stacking

faults or interstitial defects within the III-V layer. One way to reduce the growth temperature "dead zone" is to cap the II-VI layer with a different II-VI material that has a lower vapor pressure, or start the III-V layer by growing a material with a slightly higher vapor pressure. This will allow for higher III-V material quality and sharper interfaces without increasing interdiffusion between the II-VI and III-V layers. This could enhance the sharpness of the interface, minimize defect propagation in the subsequent epilayers, and reduce the unintentional doping from the exchange of atoms between the II-VI and III-V layers.

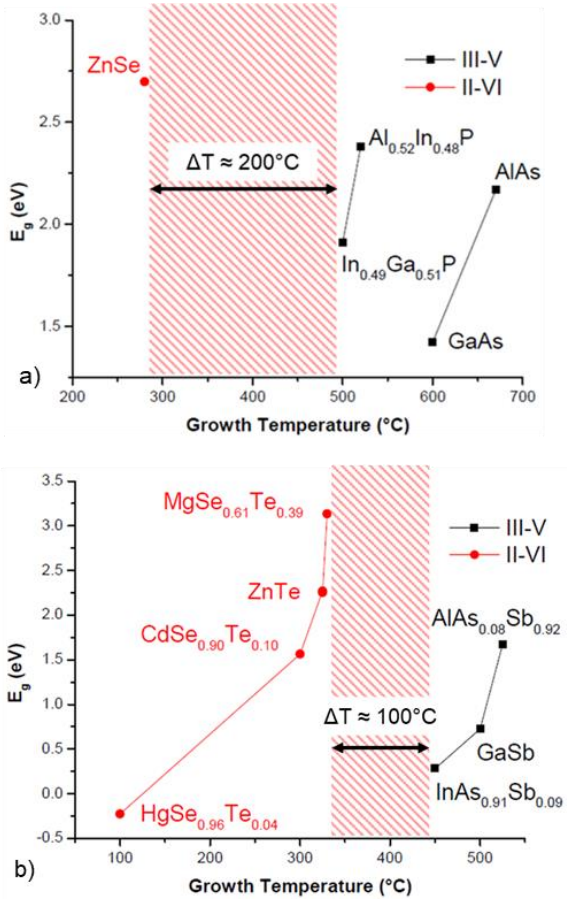

Fig. 18: Growth temperature vs band gap energy for materials lattice matched to a) GaAs substrates, and b) GaSb substrates. As the temperature 'dead zone' (red striped area) between the II-VI and III-V materials is reduced, growth of III-V materials on their lattice-matched II-VI counterpart is simplified.

Due to the significant differences in growth temperatures between GaAs and ZnSe, a multi-step growth process was adopted to optimize the GaAs material quality [72]. Arsenic has difficulty sticking to ZnSe surfaces at elevated temperatures, so a low-temperature As deposition process was implemented at 75 °C to achieve Zn-As bonds at the heterovalent interface [73], [74]. During this process, the surface reconstruction changed from a streaky c(2×2) Zn-terminated ZnSe pattern [75] to an amorphous reconstruction, signified by diffuse rings on the RHEED screen. A thin layer of Ga was then deposited on top of the As layer before annealing the substrate in the growth chamber at 420 °C under an As overpressure, at which point a streaky (2×4) surface reconstruction was observed. The rest of the GaAs quantum well was grown at 400 °C using MEE. This is in contrast to the GaAs/ZnSe double heterostructure sample, where a gradual temperature ramp up to 400 °C at 30 °C/min was sufficient to achieve a high quality 500 nm GaAs layer confined by 100 nm ZnSe.

A schematic of the quantum well and double heterostructure growth structures is shown in figure 19. The reconstruction of the GaAs surface during the double heterostructure growth shows that initially the layer is uneven as evident by the spotty RHEED pattern in figure 20, but eventually improves to a streaky (2×4) pattern as the substrate temperature is increased. PL measurements of the two samples, seen in figure 21, show the contrast between the different growth structures. A 1.56 eV emission peak can be seen from the GaAs quantum well with a low-energy shoulder from the GaAs buffer layer, only about 14 meV higher than the calculated ground state energy from a 20 nm GaAs quantum well confined by ZnSe barriers. The emission peak of the quantum well shows significant broadening, most likely due to uneven heterovalent interfaces from the

low-temperature As deposition technique. The double heterostructure, on the other hand, has a narrow peak at 1.52 eV from the direct transitions in the GaAs layer. The low-energy peak in the double heterostructure can be attributed to recombination in the defect centers [76], caused by point defects incorporated at the low GaAs growth temperature.

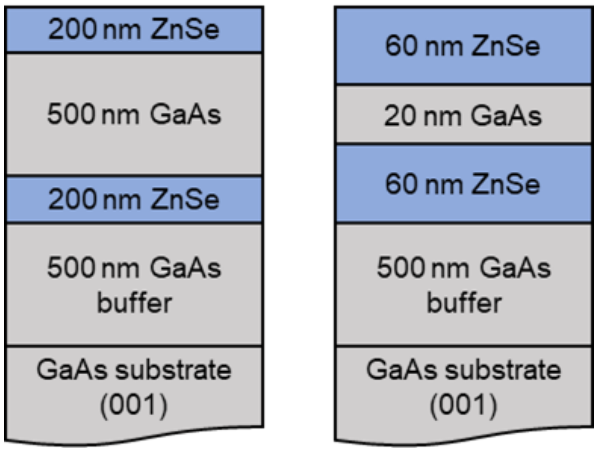

Fig. 19: Schematic growth structure for the GaAs/ZnSe double heterostructure (left) and quantum well (right) samples.

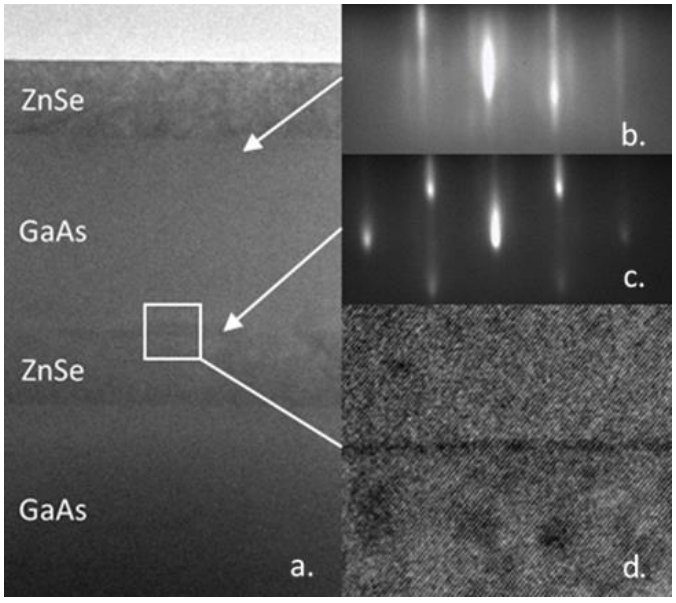

Fig. 20: TEM image of the GaAs/ZnSe double heterostructure (a,d), inset (b,c) shows the RHEED surface reconstruction evolution throughout the growth. Sample prep and imaging performed by Dr. Brian Tracy.

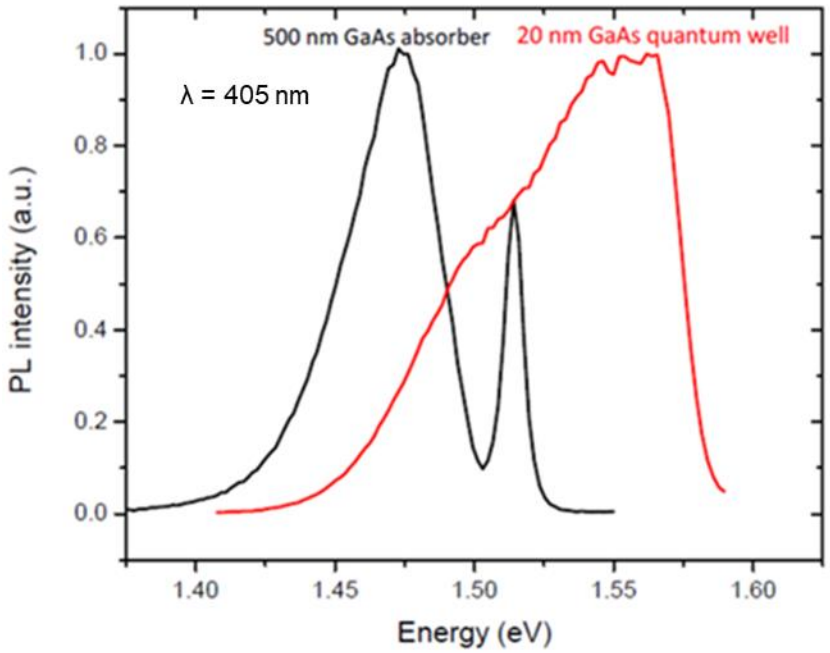

Fig. 21: PL measurements of the GaAs/ZnSe double heterostructure (black) and the quantum well sample (red).

GaAs/ZnSe heterovalent superlattices were also grown in the single-chamber MBE system using growth conditions similar to those of the GaAs/ZnSe quantum well structures. For the initial deposition of the GaAs layers on ZnSe, a low-temperature As deposition was used to avoid formation of III-VI interface bonds before depositing the GaAs material using MEE at 300 °C. Figure 22 shows a transmission electron microscope (TEM) image of the heterovalent superlattice, and the sharp interfaces and distinct individual layers can be determined from the brightness contrast between the two materials due to the difference in the atomic numbers of the different atoms.

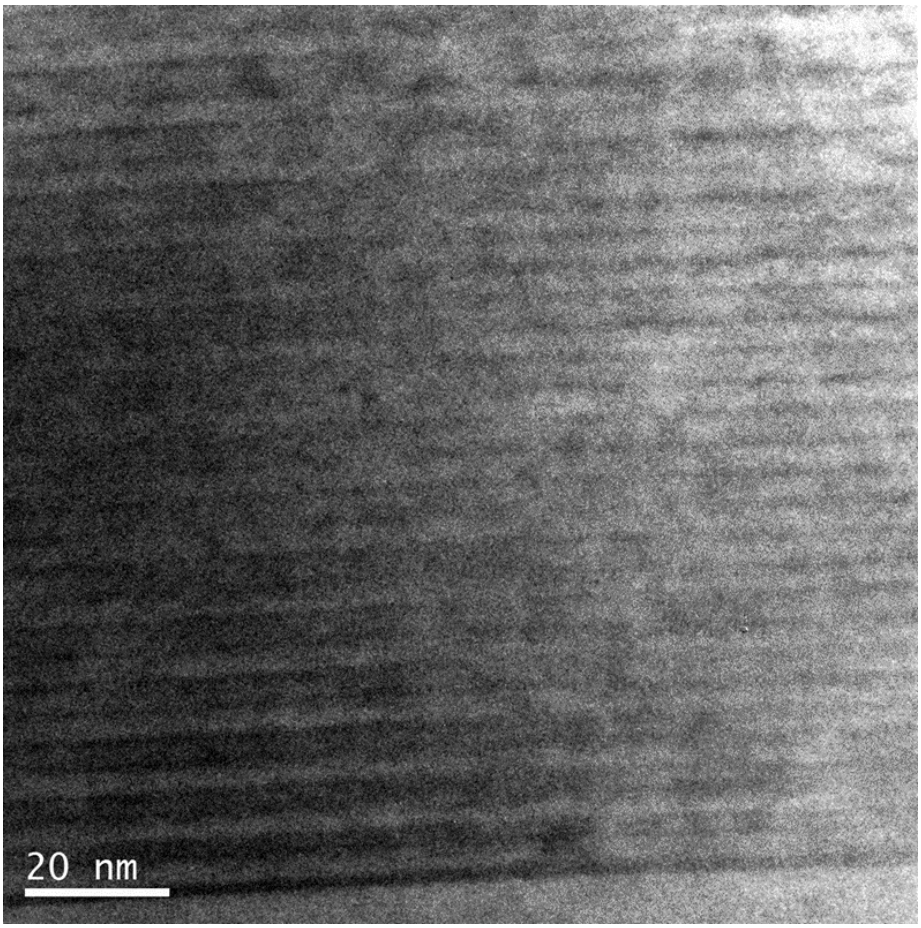

Fig. 22: TEM image of GaAs/ZnSe superlattice with 50 periods of alternating 4 nm layers. Sample prep and imaging performed by Dr. Brian Tracy.

It is clearly evident from the XRD and TEM results in figures 23 and 24 that the material quality of both the double heterostructure and quantum well samples are good and the interfaces are abrupt, but the GaAs quality of the double heterostructure is superior due to the low-temperature growth conditions required throughout the GaAs quantum well layer which causes defect propagation in the subsequent epilayers. Additionally, propagating structural defects in the ZnSe layers of the quantum well sample are visible in the TEM images, which will increase the non-radiative recombination in the GaAs well and contribute to the spectral broadening of the well emission. A GaAs multiple quantum

well structure with 3 thin GaAs wells was also grown using 100 nm ZnSe confinement layers to examine how the additional heterovalent interfaces affect the crystal quality of the structure. It can be seen from figures 25 and 26 that these layers can be stacked multiple times without destroying the structural quality of the GaAs or ZnSe epilayers. While high-quality growth of GaAs on ZnSe has been demonstrated, the large growth temperature difference between GaAs and ZnSe remains the single most pressing issue for the development of thin GaAs/ZnSe heterostructures.

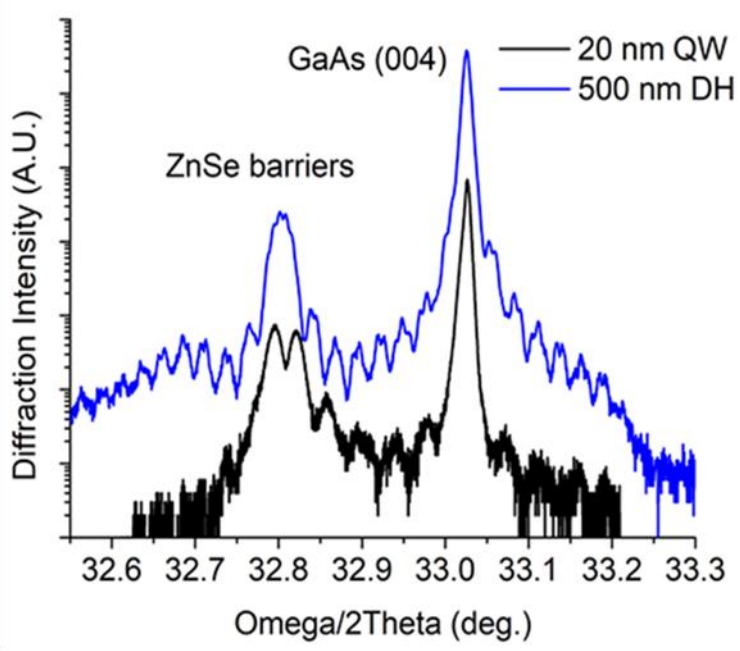

Fig. 23: XRD scan of the GaAs/ZnSe double heterostructure (blue) and quantum well (black) samples. Pendellösung fringes are seen in both of the samples, but are much more prominent in the double heterostructure sample due to the sharper GaAs/ZnSe interfaces.

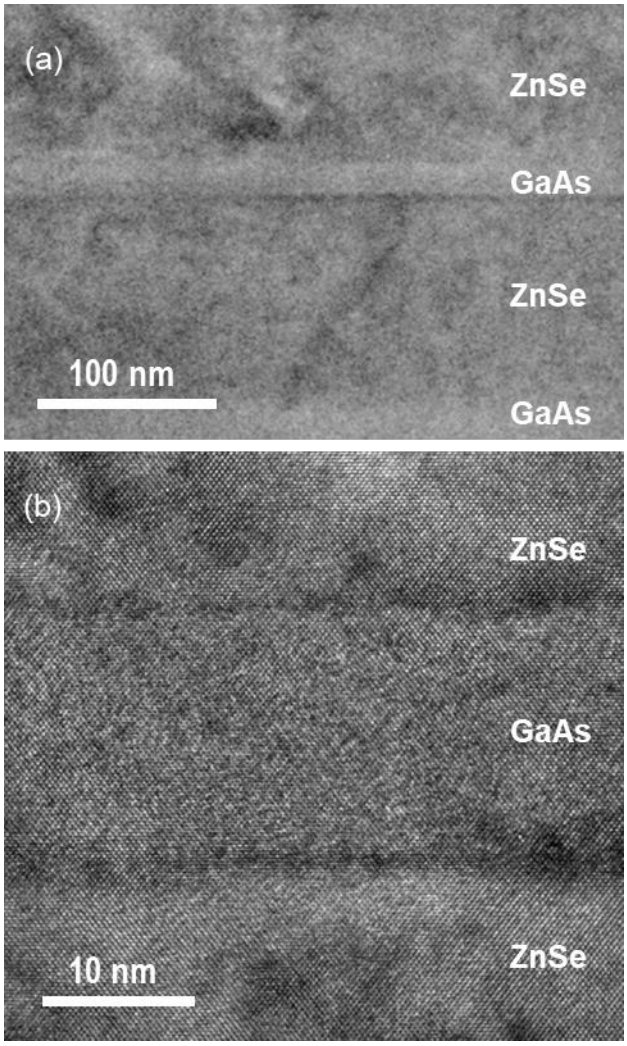

Fig. 24: TEM images of the GaAs/ZnSe quantum well, showing a) propagating defects visible in the ZnSe barriers, and b) nearly defect-free GaAs well layer. Sample prep and imaging performed by Dr. Brian Tracy.

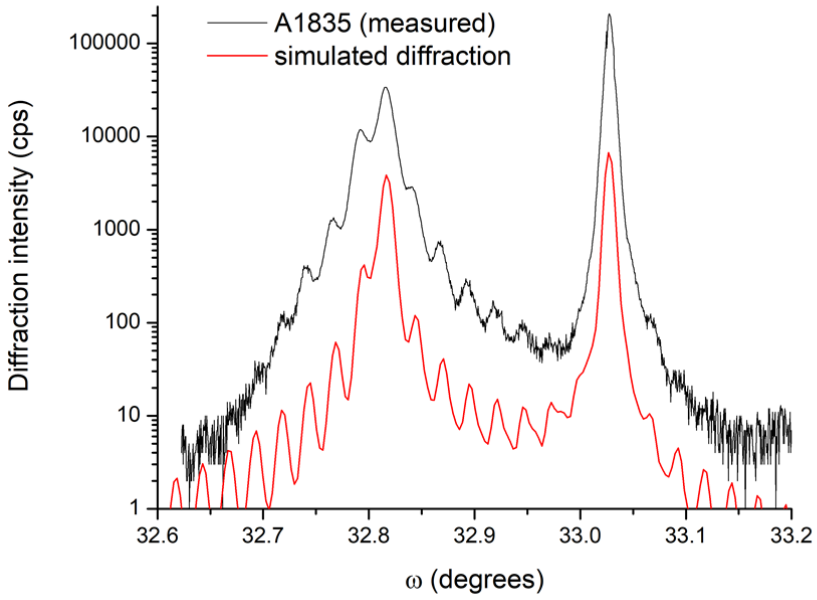

Fig. 25: XRD scan of the GaAs/ZnSe multiple quantum well structure. The diffraction pattern closely matches the simulated curve, suggesting that the additional wells in the structure do not significantly degrade the crystal quality of the epilayers.

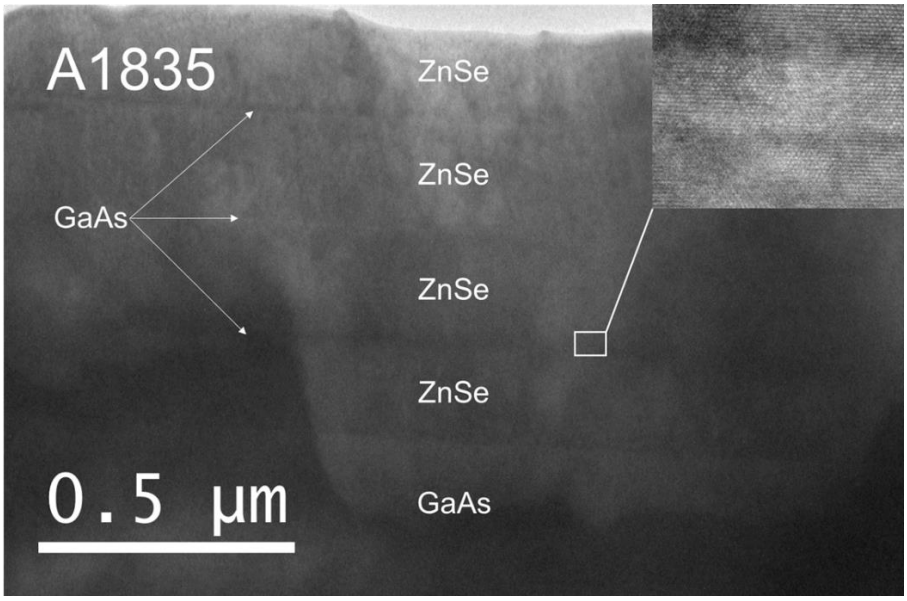

Fig. 26: TEM image of the GaAs/ZnSe multiple quantum well structure. No propagating defects are seen with the addition of more heterovalent quantum well layers. Sample prep and imaging performed by Dr. Brian Tracy.

4.2 GaSb/ZnTe heterostructures

Although historically the GaSb/ZnTe material system has not been investigated as thoroughly as the GaAs/ZnSe system, the integration of heterovalent materials on GaSb substrates is desirable for a multitude of reasons. Unlike with GaAs substrates, semi-insulating GaSb substrates are not commercially available and therefore GaSb-based electronic devices have lagged behind those based on GaAs and InP due to a lack of low-conductivity III-V materials lattice-matched to GaSb to prevent carrier leakage from the epilayers into the substrate. Additionally, GaSb has no adequate wide-band gap isovalent counterpart for suitable electron blocking layers since the AlGaSb lattice constant quickly increases as the Al composition (and therefore the AlGaSb band gap) rises. Instead, a quaternary AlGaAsSb alloy is required for lattice matching, but this material does not sufficiently contrast the low band gap and high conductivity of GaSb and can be difficult to calibrate and grow consistently. The reduced barrier height and width available for GaSb confinement is detrimental to electronic and optoelectronic devices as electrons can leak across the weak barriers and reduce the efficiency of the structure [77]. ZnTe, on the other hand, has a band gap approximately 3 times larger (2.26 eV) than GaSb and is still nearly lattice-matched to GaSb substrates (0.13 % mismatch) [78]. As seen in figure 27, the GaSb/ZnTe heterojunction has conduction and valence band offsets of 726 and 600 meV, respectively [79]. Therefore, ZnTe can be used to create insulating virtual substrates for GaSb-based microelectronics or strong electron confinement barrier layers for optoelectronic or microelectronic applications. Because of this, optimizing GaSb layers on ZnTe films can enhance the performance and the device possibilities for materials

lattice-matched to GaSb substrates by isolating the conductive substrate or unpassivated surfaces from the rest of the structure with a ZnTe barrier layer.

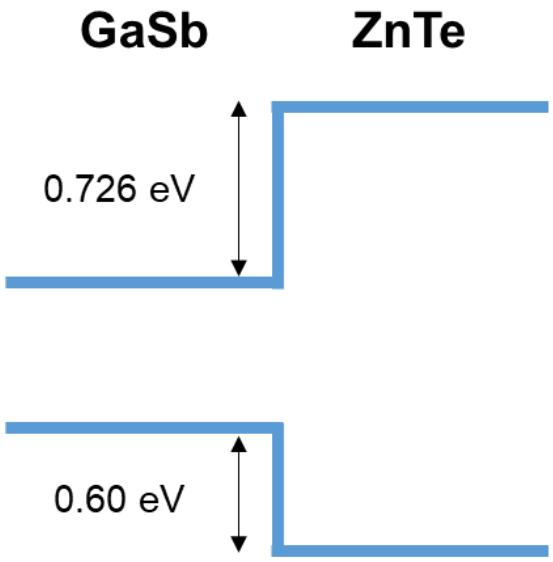

Fig. 27: Conduction and valence band offsets of the GaSb/ZnTe heterojunction.

GaSb/ZnTe quantum wells were grown on GaSb substrates using a variety of different growth conditions to examine how the interface conditions effect the crystal structure and optical emission of the GaSb well. Similar to the ZnSe/GaAs heterostructures, a II/V interface termination is achieved by applying elemental Zn and Sb fluxes between the ZnTe and GaSb layers. The interfacial Sb flux was deposited at a substrate temperature of 325-350 °C for a span of 0.5-6 minutes. A streaky (3×1) surface reconstruction and sharp XRD features, seen in figure 28, suggest that a 30-second Sb flux as the temperature is gradually raised from 325 to 350 °C is sufficient to adequately suppress the Ga-Te bonding at the interface and form high-quality GaSb layers on ZnTe. The low growth temperature required for the start of the GaSb layer is again mitigated using MEE as the substrate temperature is ramped from 350 to 460 °C at a rate of 30

°C/min. Unlike with As on ZnSe, Sb does not desorb from the ZnTe surface and therefore more precise control of the low-temperature V/III ratio is required for an acceptable GaSb quality using MEE. Due to the close proximity of the heterovalent interfaces, the flux conditions between the ZnTe and GaSb layers play a critical role in limiting the interface recombination velocity and improving the PL emission. Three emission peaks, shown in figure 29, were observed at low temperatures from the GaSb/ZnTe quantum well structure. These peaks can be attributed to the different recombination mechanisms in the growth structure. The peak at 780 meV, which is blue-shifted with respect to the bulk GaSb band gap and only seen at low temperatures, is from the band-to-band recombination in the GaSb well, whereas the lower-energy peaks can be attributed to recombination due to defect states since these peaks become prominent as the temperature increases along with the ionization probability of point defects in the GaSb layer. The emission strength of the GaSb well, while low, could possibly be improved with further tuning of the growth conditions. Experimentation with the V/III flux ratio at reduced substrate temperatures would benefit the PL characteristics of the quantum well, as the excess Sb atoms may not completely desorb from the surface and could introduce parasitic In vacancies or Sb interstitial point defects.

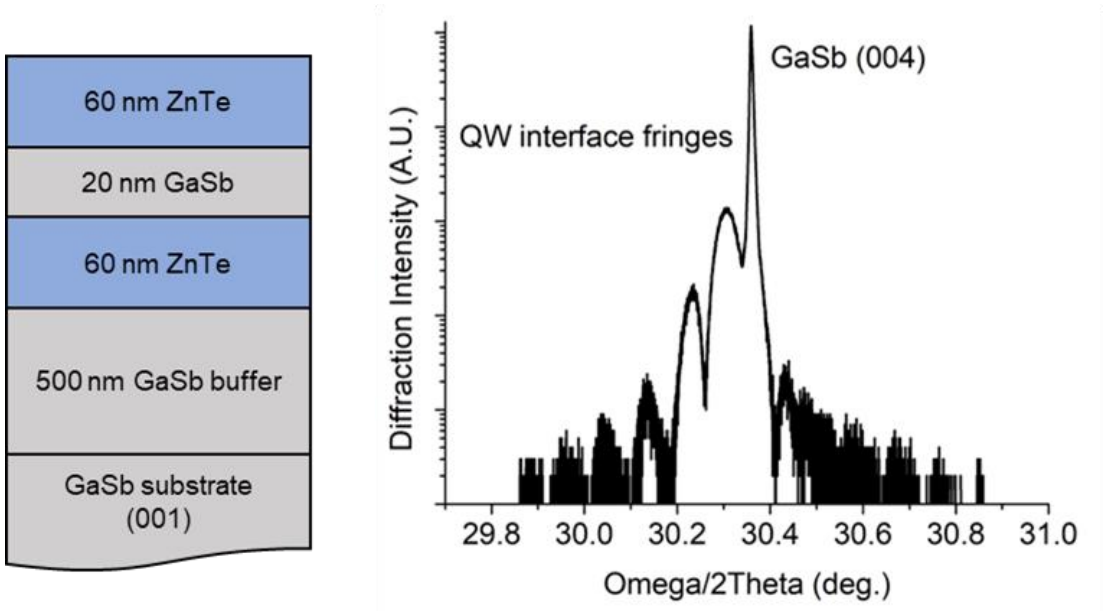

Fig. 28: Schematic growth structure and XRD pattern for the GaSb/ZnTe quantum well sample.

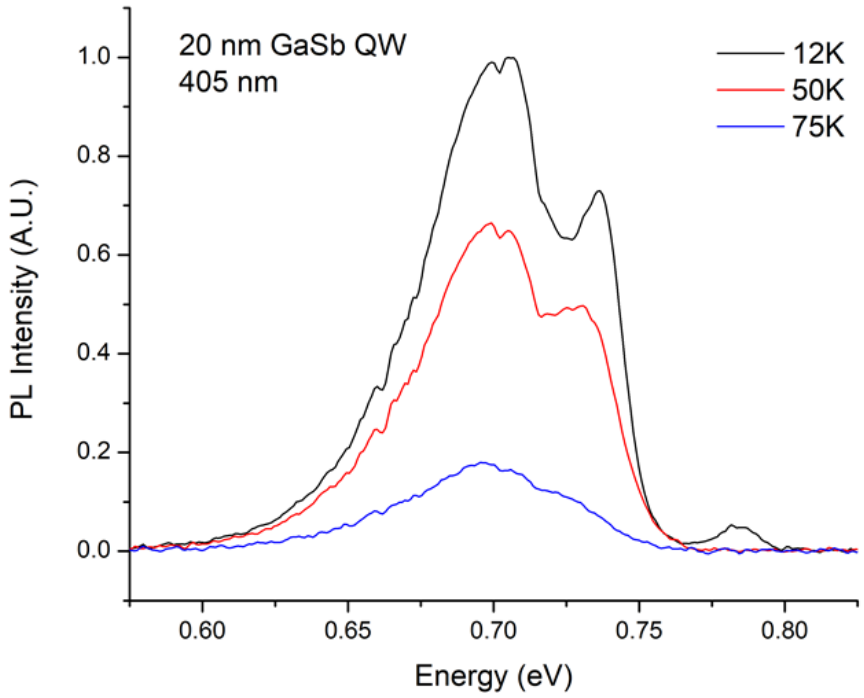

Fig. 29: PL spectrum of the 20 nm GaSb/ZnTe quantum well grown on a (100) GaSb substrate. The 405 nm pump laser is absorbed in both the GaSb and ZnTe layers.

GaSb/ZnTe superlattices were grown with 50 periods of alternating ZnTe/GaSb layers 5 nm thick. The GaSb layers were achieved using MEE at the same substrate growth temperature as the ZnTe layers with Sb and Zn elemental fluxes at the interfaces to promote II-V bonding. Although the RHEED reconstruction appeared spotty after the first few periods, TEM images in figure 30 of the structure show sharp, well-defined interfaces with no propagating defects visible in the layers. The structure gave PL emission under a pump wavelength of 785 nm, shown in figure 31, but the emission energy peak of 710 meV at 12 K was well below the GaSb band gap. This suggests that the layers in the GaSb/ZnTe superlattice have numerous defects that create mid-gap traps which increase the optical density of states at energies below the band gap.

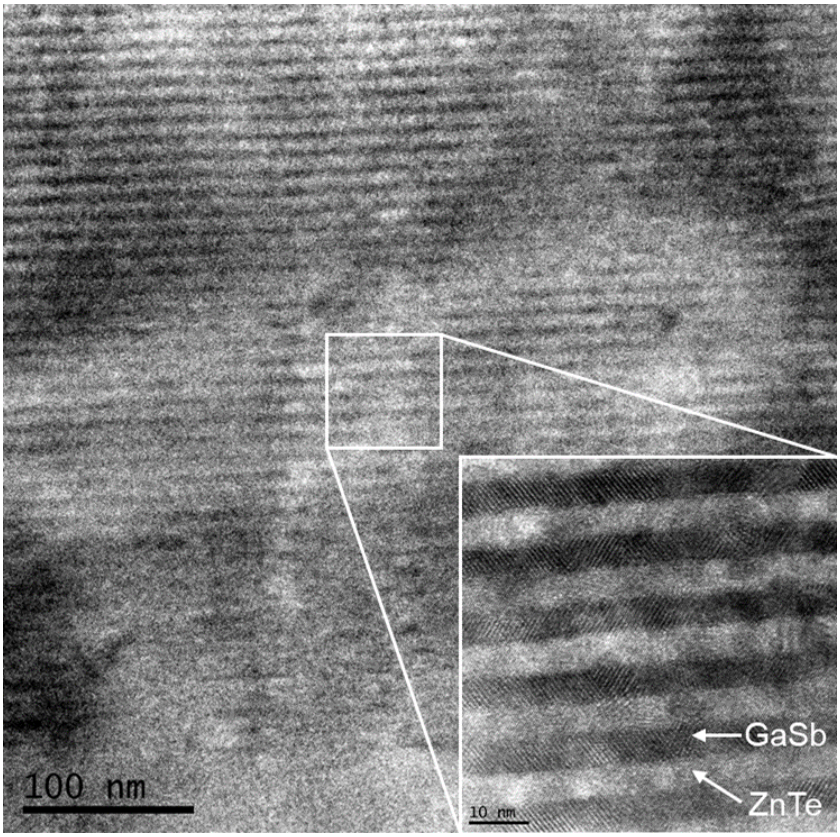

Fig. 30: TEM image of GaSb/ZnTe superlattice with 50 periods of alternating 5 nm layers. Sample prep and imaging performed by Dr. Brian Tracy.

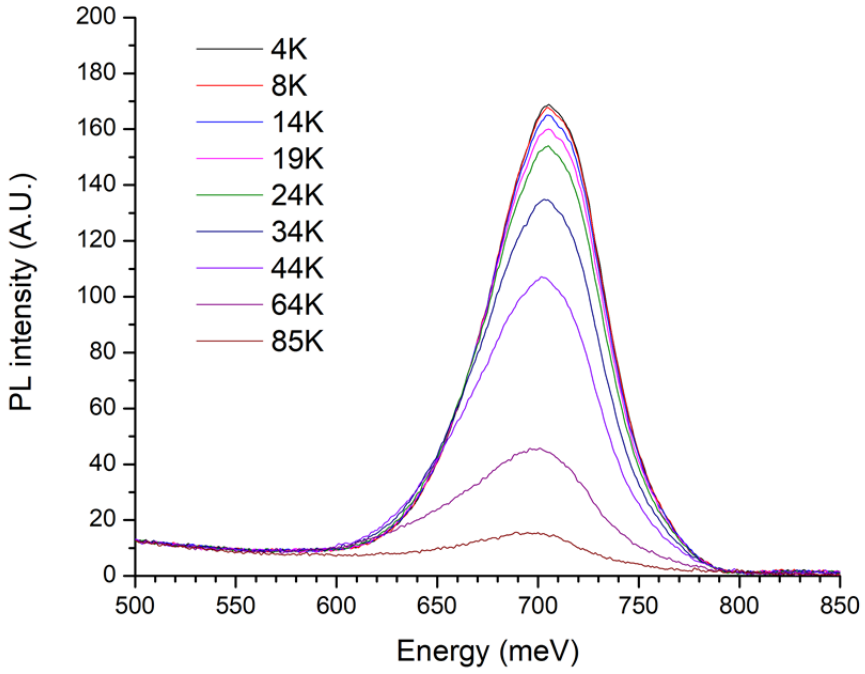

Fig. 31: Temperature-dependent PL spectrum of a GaSb/ZnTe superlattice.

In addition to the quantum structures, thicker GaSb layers were grown on ZnTe layers by using a temperature ramp growth method to achieve high-quality GaSb layers without destroying the ZnTe layers. The double heterostructures were grown by starting the growth at 300 °C and then ramping to 500 °C over the span of 10-15 nm of GaSb growth to achieve high-quality GaSb layers confined by ZnTe barriers. Figure 32 shows the XRD pattern of a 500 nm GaSb layer confined by 100 nm ZnTe barriers. Good agreement between the measured and simulated diffraction pattern, as well as prominent Pendellösung fringes, certify the high crystalline quality of the GaSb layers achieved by using a substrate temperature ramp. No destruction of the ZnTe layers or propagating defects were noticed in the double heterostructure even with a GaSb growth temperature

of 500 °C. With the temperature ramp method, GaSb can be grown at its optimal substrate growth temperature as long as the ZnTe layer is capped with a low-temperature GaSb layer to prevent the ZnTe from desorbing. This contrasts many other lattice-matched heterovalent material combinations, including GaAs/ZnSe and InSb/CdTe, which are susceptible to significant deterioration of the II-VI layer at the optimal III-V growth temperature. The GaSb/ZnTe material system is therefore an excellent candidate for structures which require thick, high-quality III-V layers, such as optical cavities.

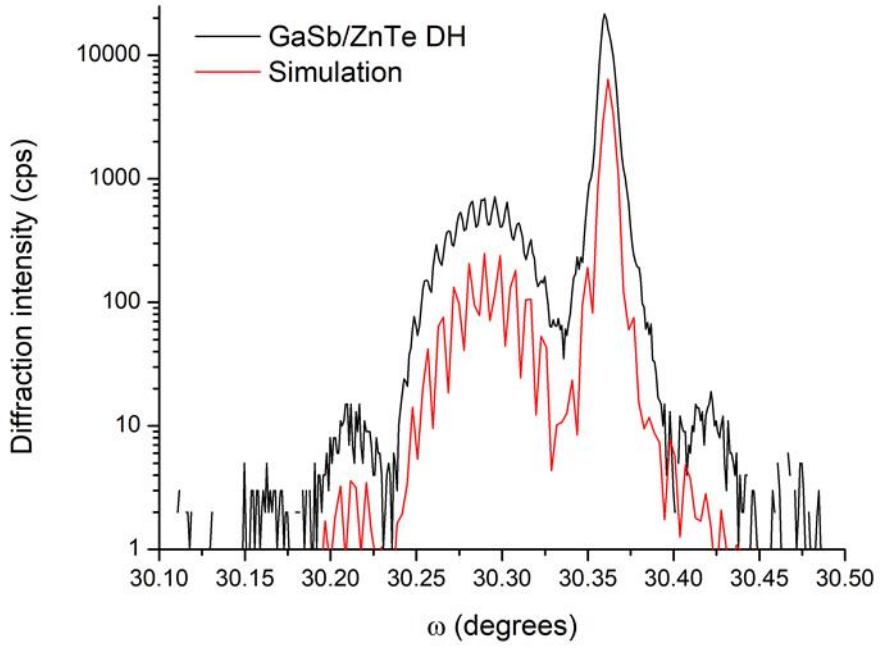

Fig. 32: XRD pattern and simulation of 500 nm GaSb confined by 100 nm ZnTe layers grown on GaSb substrates.

The GaSb/ZnTe material system is also closely lattice-matched to the InAs/CdSe system, with a lattice mismatch of 0.6 % between GaSb and InAs. By incorporating about 9 % Sb into the InAs lattice, InAsSb can even be perfectly lattice-matched to GaSb with a

significantly smaller band gap energy. InAsSb/ZnTe quantum wells and double heterostructures were grown on GaSb substrates with a small amount of Sb incorporated into the InAs growth to keep the InAsSb layer nearly lattice-matched to the GaSb/ZnTe material system. The quantum well samples were grown using MEE at a substrate temperature of 350 °C, and TEM images of the InAsSb/ZnTe quantum well, seen in figure 33, show well-defined interfaces and defect-free layers. During the low-temperature growth of the InAsSb layer, the surface reconstruction as observed by RHEED appeared spotty during the start of the growth, but a (2×4) pattern, shown in figure 34, was clearly evident shortly after starting the growth of the layer.

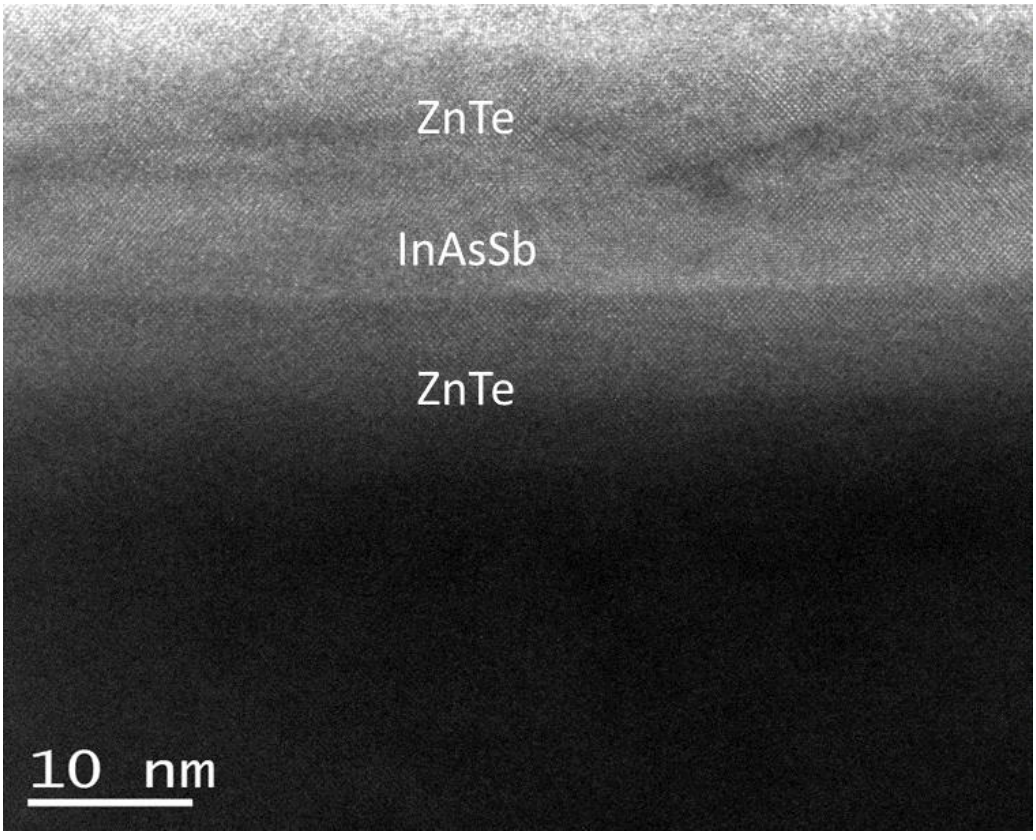

Fig. 33: TEM image of the InAsSb/ZnTe quantum well sample. Minimal propagating defects were seen when the InAsSb layer was grown using migration-enhanced epitaxy. Sample prep and imaging performed by Dr. Brian Tracy.

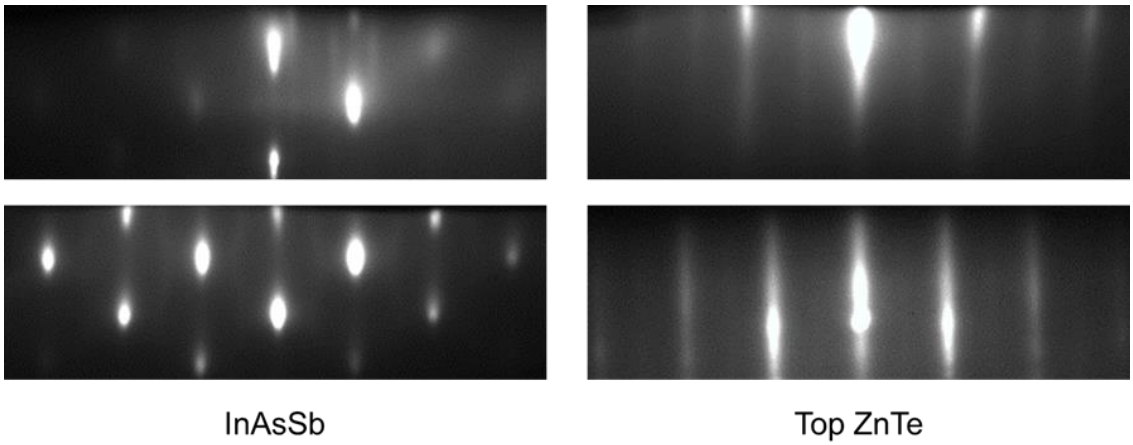

Fig. 34: (2×4) surface reconstruction of InAsSb on ZnTe buffer layers grown at 350 °C as measured by RHEED, and the c(2×2) reconstruction of the ZnTe barrier layer grown on InAsSb.

For thicker InAsSb layers, a temperature ramp from 370 °C to 450 °C was utilized to increase the crystal quality of the III-V material. Figure 35 shows the growth structure and surface reconstruction of an InAsSb/ZnTe double heterostructure grown on GaSb, and as the substrate temperature is increased during the InAsSb layer growth, the RHEED reconstruction becomes streakier signifying that the temperature ramp helps to smooth the growth surface and increase the material quality of the InAsSb. PL measurements, shown in figure 36, demonstrate the adequate optical quality of the material grown using the temperature ramp method. The low-energy tail of the higher-power PL spectrum is indicative of shallow below-band gap states present in the InAsSb layer, likely caused by an enhanced defect density from the low growth temperature at the beginning of the InAsSb growth. Due to the presence of these states, the first derivatives of the PL peaks were calculated to determine at which energy the optical density of states is highest, which corresponds to the optical band gap of the material [80]. Using this method, a band gap energy of 411 meV was determined for the InAsSb layer at 13 K. This value corresponds

to an As composition of 99 %, slightly higher than the target 98 % As. XRD measurements of the structure, shown in figure 37, confirm that the structural quality of the InAsSb layer is poor due to the extremely large FWHM of the InAsSb peak. While the InAsSb layer contains a high defect density, this preliminary structure demonstrates that optical emission can be achieved even in relatively low-quality InAsSb/ZnTe heterostructures, which suggests that ZnTe can be integrated into the GaSb/InAsSb material system with further development of the InAsSb growth on ZnTe.

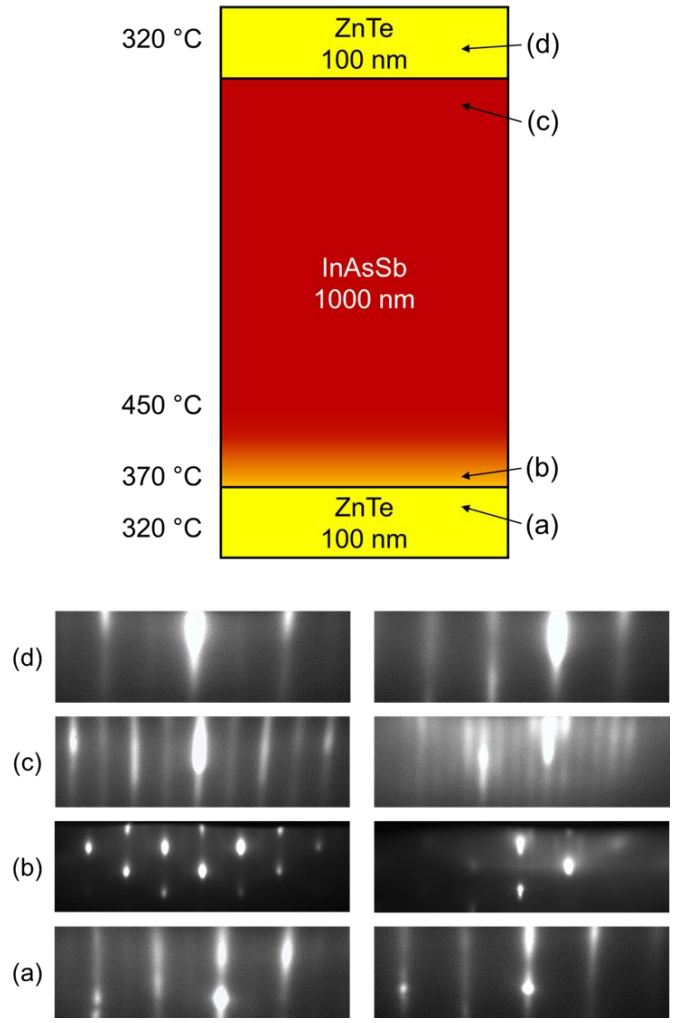

Fig. 35: Schematic growth structure, substrate growth temperatures, and surface reconstruction at various intervals during the growth of an InAsSb/ZnTe double heterostructure.

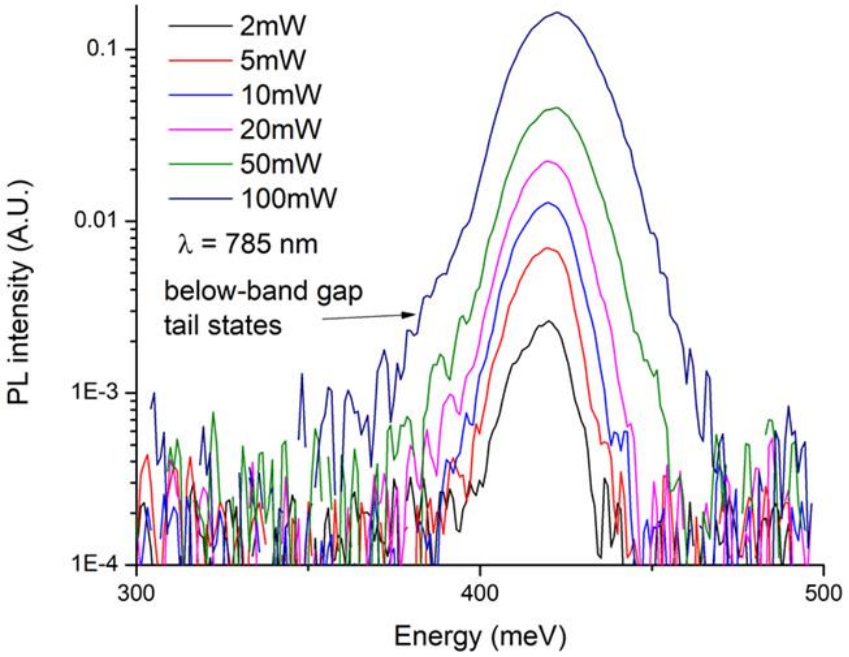

Fig. 36: Power-dependent PL spectrum of a 1 μm InAsSb layer with a target 2 % Sb incorporation confined by ZnTe barriers at 13 K.

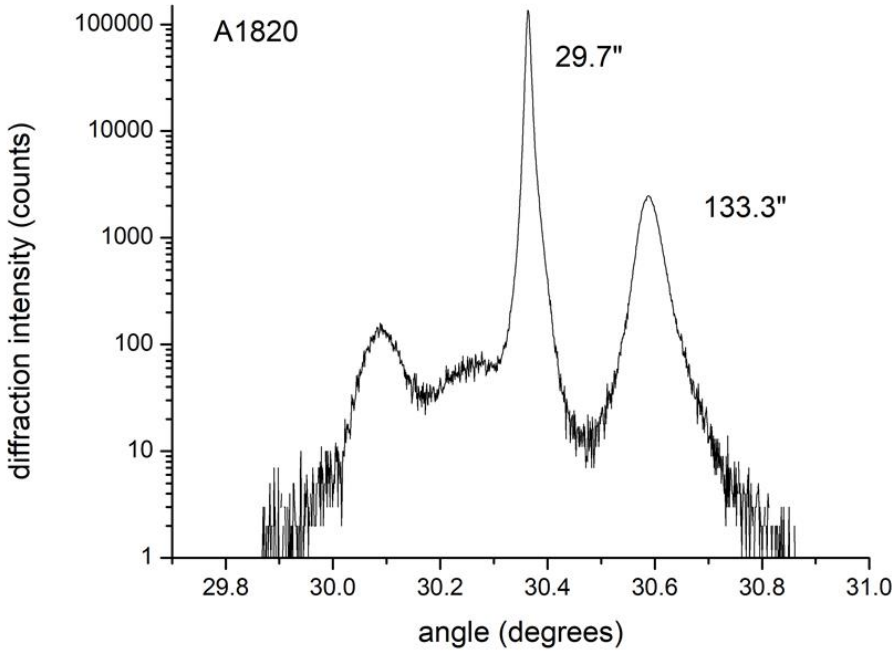

Fig. 37: XRD pattern of the InAsSb/ZnTe double heterostructure. The large FWHM of the InAsSb layer is caused by the low growth temperature used at the start of the InAsSb layer.

4.3 InSb/CdTe heterostructures

Electron mobilities in InSb are some of the highest reported values for compound semiconductors [81], but the large lattice constant leaves this crystal without any suitable lattice-matched III-V counterparts to form monolithic heterostructures. This hamstrings one of the most promising semiconductor materials, as essentially no monolithic device structure can be created by combining InSb with other III-V materials. Instead, CdTe can be combined with InSb to form a wide-band gap barrier layer lattice matched to InSb. InSb also has a relatively low growth temperature (390 °C) compared to most of the other III-V materials due to the relatively high diffusion length of the In and Sb adatoms. This property is beneficial for heterovalent integration because of the limits placed on the substrate temperature once the II-VI material has been deposited, as illustrated by figure 38, but also can cause problems since these atoms diffuse into the II-VI layers relatively easily [82]. Growth of InSb on CdTe was demonstrated with substrate temperatures up to 310 °C, but temperatures any higher resulted in significant interdiffusion between the CdTe and InSb layers. Sb and Cd overpressures were applied between each layer to suppress the formation of III-VI compounds at the interface [83]. Quantum well and superlattice samples were grown with InSb layer thicknesses ranging from 3-20 nm. For the quantum well samples, the InSb was surrounded by 200 nm CdTe layers to achieve sufficient absorption in the barriers from the 785 nm laser on the FTIR system. The superlattices used much smaller CdTe layers on the order of a few monolayers, with 20 nm CdTe barriers surrounding the structure to enhance the confinement in the superlattice.

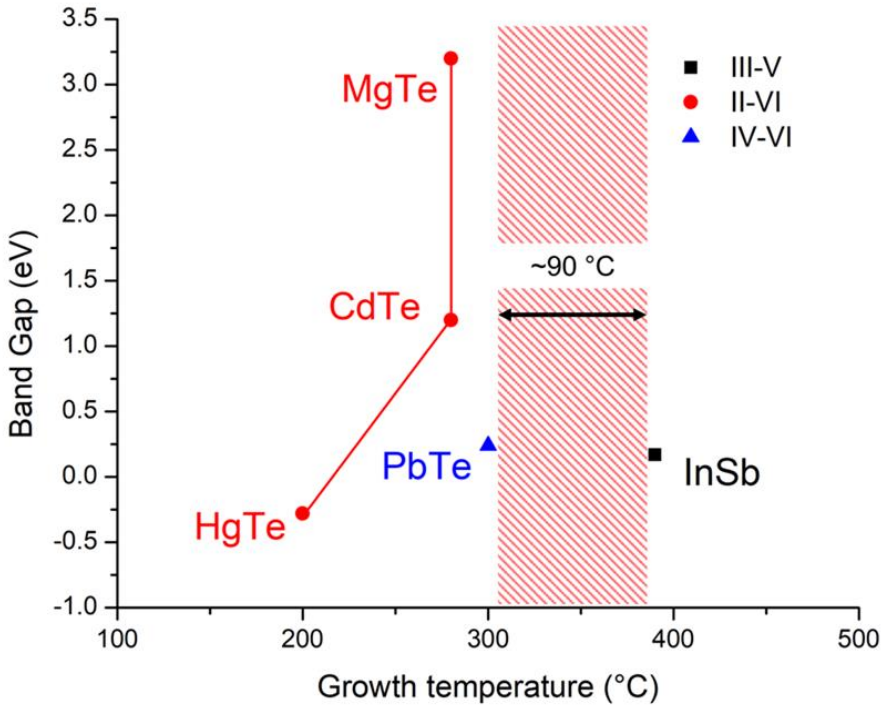

Fig. 38: Growth temperature mismatch and band gap energy of III-V, II-VI, and IV-VI materials lattice-matched to InSb substrates.

PL studies of the InSb/CdTe superlattices show a very strong emission peak that is blue-shifted compared to the InSb band gap energy, as seen in figure 39, but the exact source of the emission is still a matter of speculation due to the low quality of the superlattice crystal structure. Interestingly, this result contrasts the GaSb/ZnTe superlattice sample discussed previously, where the crystal quality was relatively good but the PL emission energy was redshifted with respect to the bulk GaSb band gap. XRD measurements of the superlattice, shown in figure 40, show no satellite peaks and therefore it can be concluded that the periodicity of the superlattice is lost due to defect formation and interface diffusion, among other causes. An emission peak similar to the one seen in the InSb/CdTe superlattice was observed from PbTe/CdTe superlattices which leaves the

low-quality CdTe layers the most likely source, but only when CdTe is combined with another material in multiple layers. This suggests that the emission is from defects within the CdTe layers, but more experiments are required to confirm this hypothesis. The emission from the InSb/CdTe superlattices tends to increase as the crystal quality of the layers decreases, and the roughest superlattices emitted the brightest PL signal out of all heterovalent samples grown in the single chamber system. Previous studies with PbTe/CdTe superlattices have demonstrated a similar phenomenon where the PL intensity decreases with increasing crystal quality [84], lending more evidence to the hypothesis that the CdTe layers are a key part of the intense IR emission. XRD measurements of the InSb/CdTe heterostructures show that while the crystal structure is primarily zincblende, a faint peak from the (002) plane indicates that there could be some compound formation at the heterovalent interface. Typically, the (002) diffraction condition is very weak for InSb and no peak should be noticeable in perfect materials. On the other hand, the condition for weak diffraction in fluorite crystals such as In_2Te_3 is satisfied for the (002) plane [85]. The intensity of the (002) diffraction peak can provide insights into the extent of the interfacial compounds, as a higher composition of In_2Te_3 at the interfaces will increase the (002) peak intensity, and also produce a lower quality zincblende crystal.

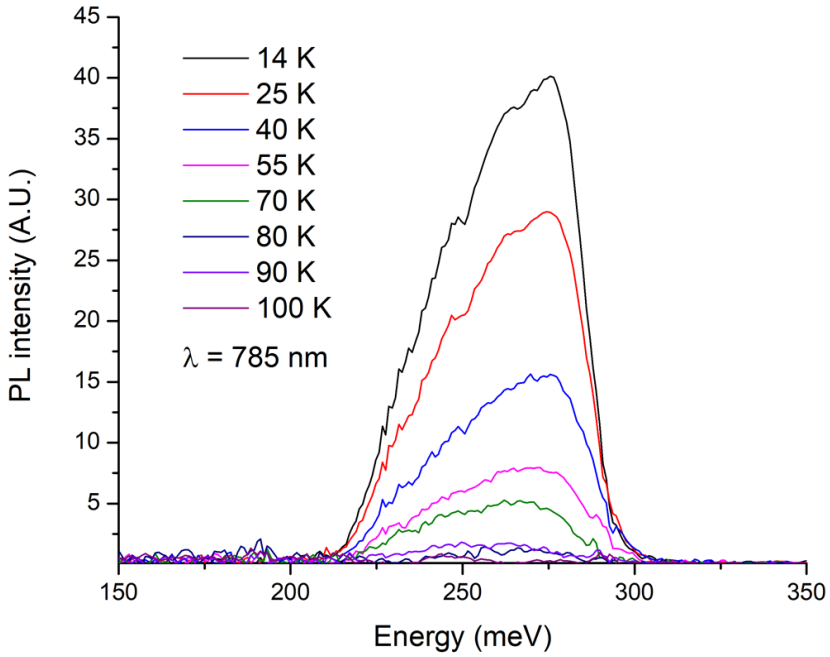

Fig. 39: FTIR spectrum of an InSb/CdTe superlattice sample. The emission from this sample is unexpected due to the low crystal quality of the layers.

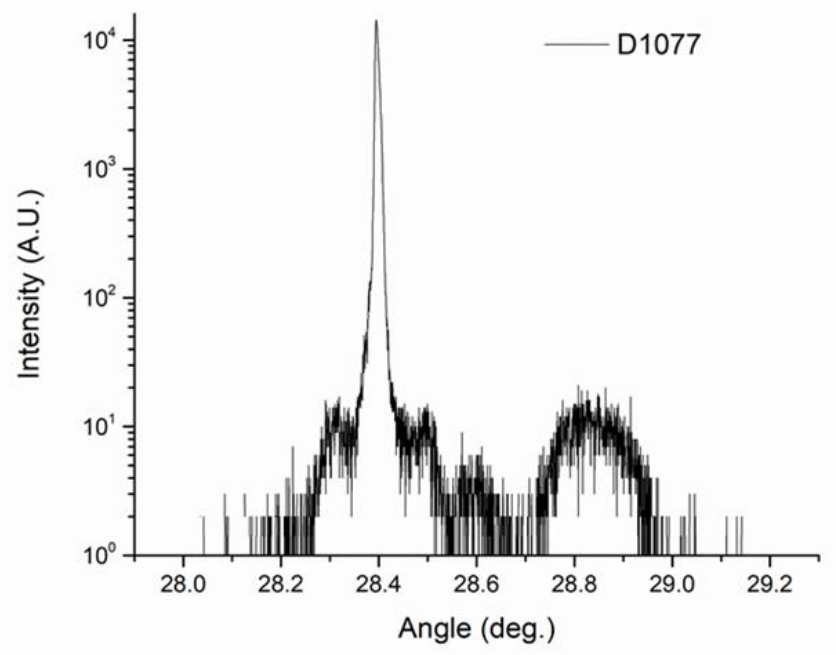

Fig. 40: (004) XRD pattern of the InSb/CdTe superlattice. Although the PL emission intensity is strong, the crystal quality of the superlattice is notably poor and no satellite peaks are seen in the diffraction pattern.

Other InSb/CdTe heterostructures were grown to help determine the origin of the enigmatic features seen in the PL and XRD results of the superlattice samples. An InSb/CdTe double heterostructure was grown to examine the effect of the different interfaces on the material properties. Figure 41 shows the growth schematic and XRD pattern for the double heterostructure, with a 300 nm InSb layer confined by 20 nm CdTe barriers. The InSb layer was initiated at a substrate temperature of 280 °C and ramped to 310 °C over the span of one minute. XRD results show a similar peak seen in the superlattice samples to the right of the InSb substrate peak, suggesting the InSb layer grown on CdTe may be affected by the interface bonding or the reduced growth temperature. Pendellösung fringes seen throughout the XRD scan suggest that even though the InSb layer may be highly strained, a coherent crystal structure is retained throughout the sample with reasonably sharp heterovalent interfaces. Unfortunately, the features in the XRD diffraction pattern show that the crystal structure of the heterostructure is far from what we expect to see and might be affected by the formation of unexpected layers or diffusion between CdTe and InSb.

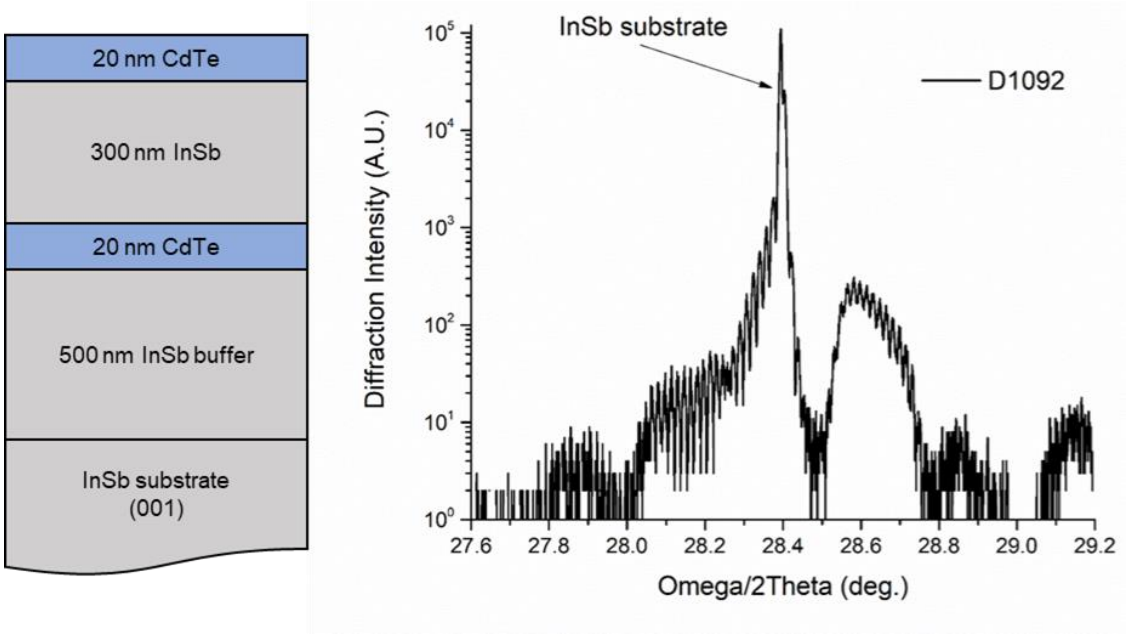

Fig. 41: Growth structure schematic and XRD spectrum of the InSb/CdTe double heterostructure. Pendellösung fringes suggest sharp, well-defined interfaces, but the peak at 28.6° is not associated with either CdTe or InSb.

While the growth of InSb on CdTe layers has presented a strong challenge, other IR materials are available for monolithic integration with InSb substrates. The ability to realize high-quality CdTe layers on InSb therefore suggests that materials with similarly low growth temperatures can be realized on this system. HgCdTe detectors are still the dominant technology for MWIR/LWIR detection due to its direct, tunable band gap [86], but state-of-the-art substrates for HgCdTe detectors are still incredibly small and expensive with a single supplier selling small (maximum 7 cm^2) CdZnTe substrates for thousands of dollars per cubic centimeter. By growing virtual CdZnTe substrates on lattice-matched (211) InSb wafers, which are available up to 4" in diameter, the price and array size can be made far more competitive than with the current CdZnTe substrates. Additionally, the lattice-matched nature of InSb, HgCdTe, and CdZnTe makes the defect density far lower

than any of the virtual substrates grown on GaAs or Si. Incorporation of other materials such as MgCdTe can be utilized for optical and electrical confinement, and sacrificial MgTe layers can be deposited before the CdZnTe virtual substrate to enable lift-off technology. This substrate separation technique is of interest for thin and flexible IR devices, and will allow for back-side illuminated devices and negate the effects of In diffusion from the InSb substrate during the high-temperature post processing steps. Development of II-VI growth on (211) InSb also enables polar heterovalent interfaces since the (211) zincblende surface is terminated with a single element. This feature may help to enhance the sharpness and electrical characteristics of the heterovalent interface due to the strict elemental bonding arrangement at polar interfaces. Additionally, structures to improve LWIR devices such as DBRs and optical cavities can be achieved on (211) InSb due to the close lattice match, which could enhance the performance of current state-of-the-art devices. The integration of these various lattice-matched heterovalent materials have a strong prospect to enable high-quality IR optical cavity devices, including lasers and detectors which span the entire IR spectrum.

Due to the complicated growth process of HgCdTe, the (211) axis is chosen as the growth face because it has been shown to enhance the growth efficiency and crystal quality of the II-VI material [87]. For growth on (211) substrates, the flux conditions were similar to the (100) conditions, with the composition of Zn in the CdZnTe alloy first calibrated on (100) substrates by calculating the lattice constant from the XRD spectrum peak before transferring over to the (211) substrates. During growth, the RHEED reconstruction showed an inclined streak pattern, seen in figure 42, which corresponds to a step-flow growth mode. The change in the RHEED pattern is due to the stepped growth surface of

the (211) face, compared to the relatively flat surface of the (100) face. XRD measurements, shown in figure 43, demonstrate a FWHM value of about 36" for a 3-micron CdZnTe virtual substrate grown on (211) InSb substrates. This corresponds to a low defect density, as illustrated by a confocal PL map of the sample in figure 44 from which a defect density of about 10^6-10^7 cm^{-2} was determined. Table 4 shows the structural characterization results of CdZnTe layers of different thicknesses with a target Zn incorporation of 4 %. Although no peaks associated with CdTe have been reported on any of the XRD scans for CdTe grown on (211) InSb, the addition of a small amount of Zn to the CdTe lattice has been shown to reduce the defect density in CdZnTe substrates [88] and a prominent peak associated with CdZnTe can be seen in the XRD scan. Therefore, while Zn helps to bring the lattice constant of the layer closer to HgCdTe, it also helps reinforce the structural integrity of CdTe layers grown on (211) InSb substrates.

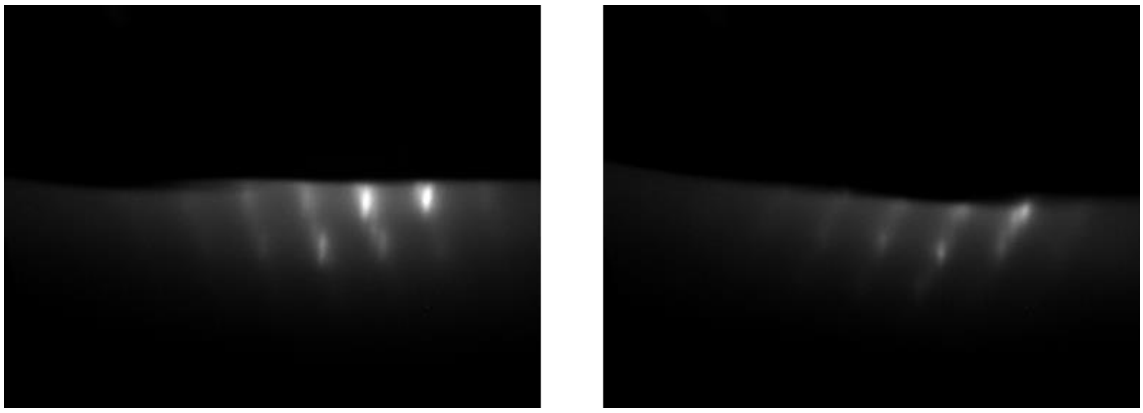

Fig. 42: Surface reconstruction of CdZnTe grown on (211) InSb substrates observed with RHEED.

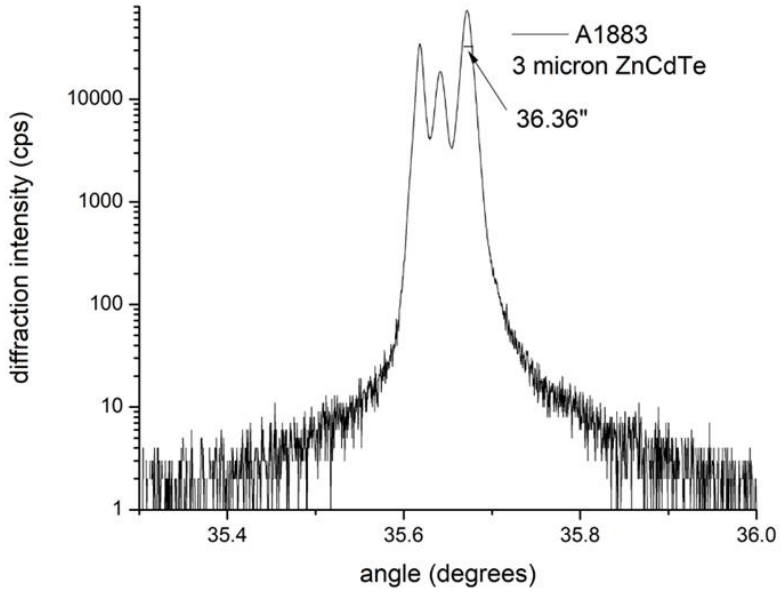

Fig. 43: (224) diffraction pattern of CdZnTe grown on a (211) InSb substrate. A Zn composition of approximately 3.25% was calculated from the angular displacement, and the FWHM of the CdZnTe peak was only 36". The center peak between the InSb and CdZnTe peaks is due to As incorporation in the InSb buffer layer.

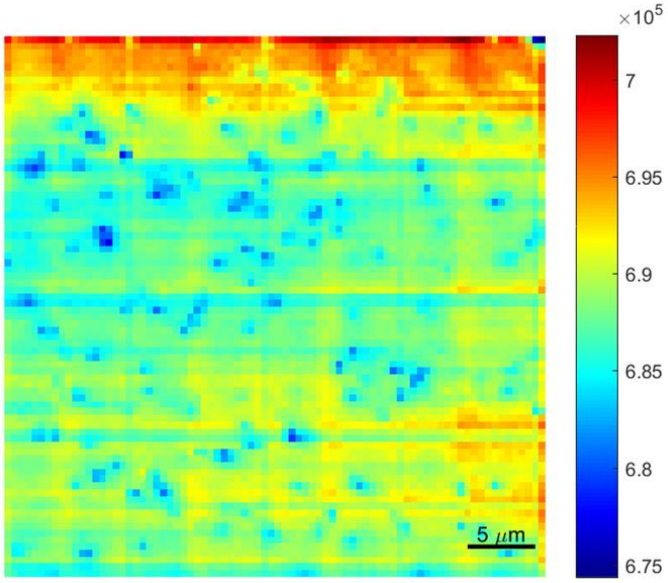

Fig. 44: Confocal PL map of a 3 micron CdZnTe virtual substrate grown on (211) InSb using a 532 nm pump laser. The dark spots correspond to areas where the PL signal was lower due to defects in the crystal, and a defect density on the order of 10^7 cm^{-2} can be calculated from the image.

Table 4: Analysis of some structural properties of CdZnTe samples grown on (211) InSb as determined by XRD measurements.

Sample #	Zn (%)	Thickness (μm)	Peak FWHM (“)
A1880	6.17	.75	95.90
A1881	3.77	.75	52.51
A1883	3.25	3	36.36
A1885	4.85	5	84.60
A1886	4.72	2	79.55

Even with the low FWHM of the CdZnTe virtual substrate, the usefulness of the wafers is limited by diffusion of In into the II-VI absorber layer from the InSb substrate during HgCdTe device post-processing. This issue can be mitigated using a number of different techniques, including using a PbTe buffer layer between the InSb and CdTe to block the mobile In atoms in the lattice, or by using a water-soluble MgTe sacrificial layer to lift the CdZnTe layer from the InSb substrate. Both of these techniques are compatible with HgCdTe growth and processing since the HgCdTe growth temperature is very low, on the order of 100 °C. Therefore, indium diffusion is not a significant problem during growth, but only occurs during post-processing where much higher temperatures are used to anneal and improve the uniformity of the HgCdTe material. By demonstrating the possibility of achieving high-quality CdZnTe layers on (211) InSb substrates, further development of this technology will undoubtedly enable large-area CdZnTe virtual substrates for HgCdTe IR detector applications in the near future.

4.4 Lead chalcogenide integration

IV-VI lead chalcogenides such as PbSe and PbTe are of interest for monolithic integration with zincblende III-V and II-VI materials due to their IR band gap and relatively low Auger coefficients [89], [90]. Although the lead chalcogenides have a rock-salt crystal structure, they are coincidentally lattice matched to certain binary zincblende semiconductors which enables epitaxial compatibility of these different material systems. Whereas the lead chalcogenides are generally grown with binary source materials in MBE due to their congruent evaporation nature [91], we have equipped our machine with elemental source material to experiment with both Pb rich and group-VI rich growth conditions. The properties of the lead salts could be used to advance the state of room-temperature IR emitters and detectors as the performance of current III-V detector technology is limited by Auger recombination at higher temperatures [92]–[95]. Auger recombination is a three-particle recombination process which scales with the carrier concentration cubed, and the Auger coefficient has also been shown to generally increase with an increase in temperature due to the increase in carrier concentration at elevated temperatures [96].

Due to the variation in the material properties of III-V, II-VI, and IV-VI semiconductors with similar lattice constants, the possibilities for band structure engineering, optical confinement, and carrier transport are further enhanced for a single monolithic device structure by incorporating lattice-matched lead salt crystals with the zincblende heterovalent heterostructures. For example, the large conduction band offset between PbTe and CdTe, with a value of 1.145 eV, compliments the large valence band offset of 0.89 eV between InSb and CdTe [97], [98], illustrated in figure 45, which could

be used to design unipolar barrier structures [99] for detectors integrated on InSb substrates. Additionally, the potential viability of large-area lead chalcogenide devices produced by integrating these materials with commercially available III-V wafers such as GaSb and InSb should not be overlooked, as many promising results are neglected due to the use of small, expensive fluorite substrates [100] or lattice-mismatched materials such as GaAs and Si [101], [102]. IV-VI/III-V integration has not been studied as extensively as lead chalcogenides grown on BaF or CaF substrates due to the large thermal expansion mismatch and the difference in crystal structures [103], but achieving high-quality heterostructures composed of monolithically-integrated III-V, II-VI, and IV-VI semiconductors will undoubtedly have a significant impact on IR device development, particularly for applications that require operation environments exceeding 300 K.

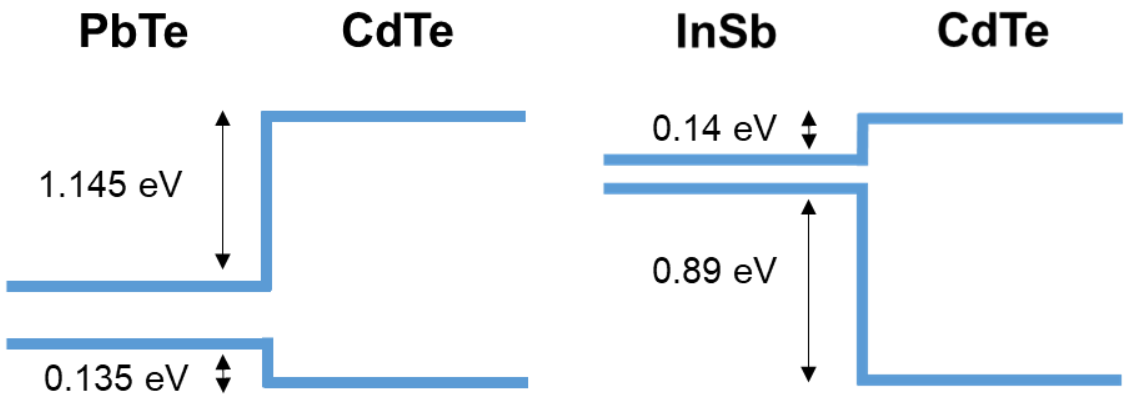

Fig. 45: Valence and conduction band offsets for PbTe/CdTe and InSb/CdTe heterojunctions.

The prospect for monolithic integration of these heterocrystalline heterostructures is exciting as they can possibly introduce new interface physics and a wealth of additional material properties for structures lattice-matched to III-V substrates. Formation of a two-

dimensional electron gas at the CdTe/PbTe interface [104], [105] and a relatively low Auger coefficient [106] in PbTe has stimulated recent interest in these heterocrystalline rock-salt/zincblende structures, but integration with III-V substrates has remained elusive since a specific, dedicated growth system is required to grow these heterostructures with an acceptable material quality. The addition of lead salts with the III-V/II-VI heterostructures could possibly reduce unintentional doping due to diffusion across the III-V/II-VI interface as the shift in lattice structure and the addition of heavy Pb atoms could block atomic migration in the crystal lattice. Other material parameters, such as thermal and electrical conductivity, absorption coefficient, refractive index, and band gaps can be manipulated within these monolithic heterocrystalline heterostructures because of the range of lattice-matched materials available and the variety of optical and electrical properties enabled by integrating semiconductors with different crystal structures.

Heterocrystalline zincblende/rock-salt InSb/CdTe/PbTe heterostructures were grown on (100) InSb substrates using a range of different growth conditions to optimize the epilayers and interfaces between the different materials. Figure 46 shows a TEM image of a PbTe/CdTe heterostructure with a clear shift in the crystal structure between the zincblende CdTe layer and the rock-salt PbTe. Due to the similar ideal growth temperatures of PbTe and CdTe, no growth temperature ramp or migration-enhanced techniques are required to grow thin, high-quality layers. The initial CdTe buffer layer was deposited using the same growth conditions as previous CdTe/InSb heterostructures before switching to the PbTe layer growth. Both Cd and Te fluxes were applied at the CdTe surface for a variable amount of time to examine how the interface termination affected the PbTe and CdTe epilayers. For thin (< 50 nm) PbTe quantum wells confined by CdTe

barriers, the interface termination primarily influenced the structure of the CdTe layers and left the PbTe layers virtually unaltered, as demonstrated by comparing the XRD of the (002) and (004) planes in figure 47. Other structures reported previously have shown similar results [107], suggesting that the atomic structure near the interface can be reconfigured by the charge distribution when the heterocrystalline interfaces are in close proximity. This structural reconfiguration was not seen in other III-V/II-VI heterostructures, such as GaSb/ZnTe and GaAs/ZnSe quantum wells, most likely because the materials are of the same crystal structure and require significant energy to alter the bonding structure. Therefore, both the charge buildup and the shift in crystal structure at the interface can contribute to the atomic redistribution seen in the samples.

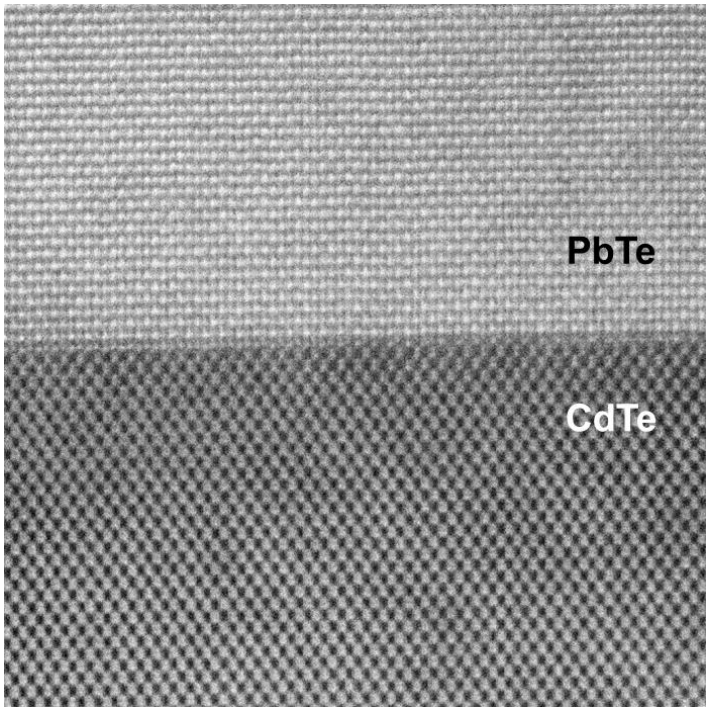

Fig. 46: TEM image of a PbTe/CdTe heterojunction. Although the two materials have a different crystal structure, their lattice constants are nearly identical and therefore they are compatible for monolithic integration via coincident epitaxy. Sample prep and imaging performed by Dr. Brian Tracy.

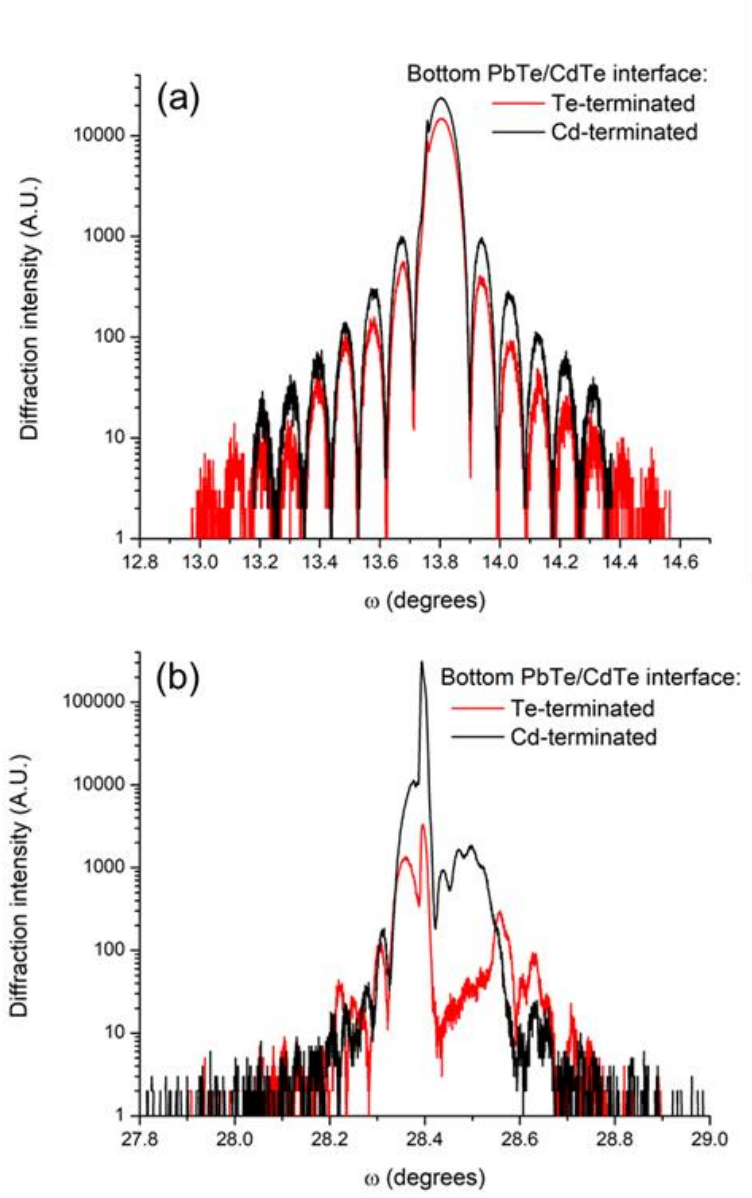

Fig. 47: XRD patterns for two PbTe/CdTe quantum wells grown with different interface terminations. The (002) plane in (a) shows virtually no deviation between samples, while the (004) plane in (b) shows a substantial shift.

PbTe layers were also grown directly on InSb to investigate the structural quality of bulk PbTe grown on zincblende substrates. XRD scans of the (002) diffraction plane show a PbTe peak corresponding to a lattice constant of 6.456 Å as seen in figure 48. A

comparison of the (004) diffraction plane between the CdTe/InSb and PbTe/InSb heterostructures, see figure 49, shows just how close the lattice constants of InSb, PbTe, and CdTe are at room temperature, even though they form two completely different crystal structures. The z-plane lattice constant of PbTe on CdTe is smaller than the fully-relaxed lattice constant of 6.462 Å due to tensile strain as the PbTe crystal expands in the x-y plane to conform to the larger InSb substrate lattice. Since CdTe grown on InSb is compressively strained and PbTe experiences tensile strain, these two materials can be integrated together to create strain-balanced heterostructures on InSb substrates if the thermal expansion difference can be mitigated.

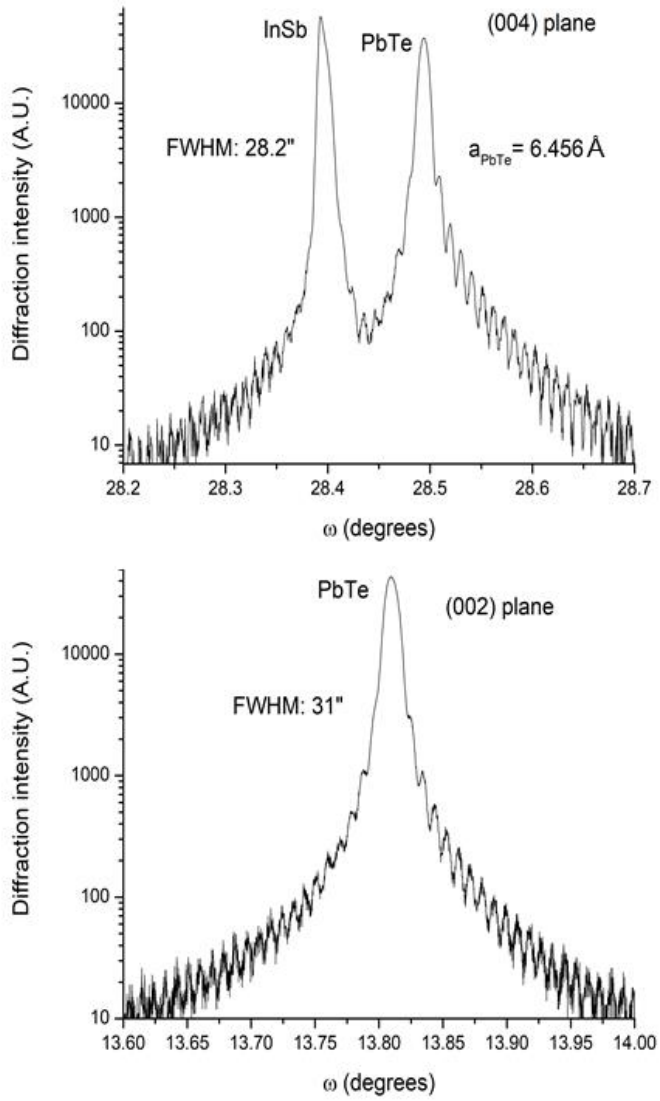

Fig. 48: (002) XRD scan for a PbTe/InSb heterostructure grown on an (001) InSb substrate. The FWHM of both peaks suggest minimal defect propagation in the PbTe layer.

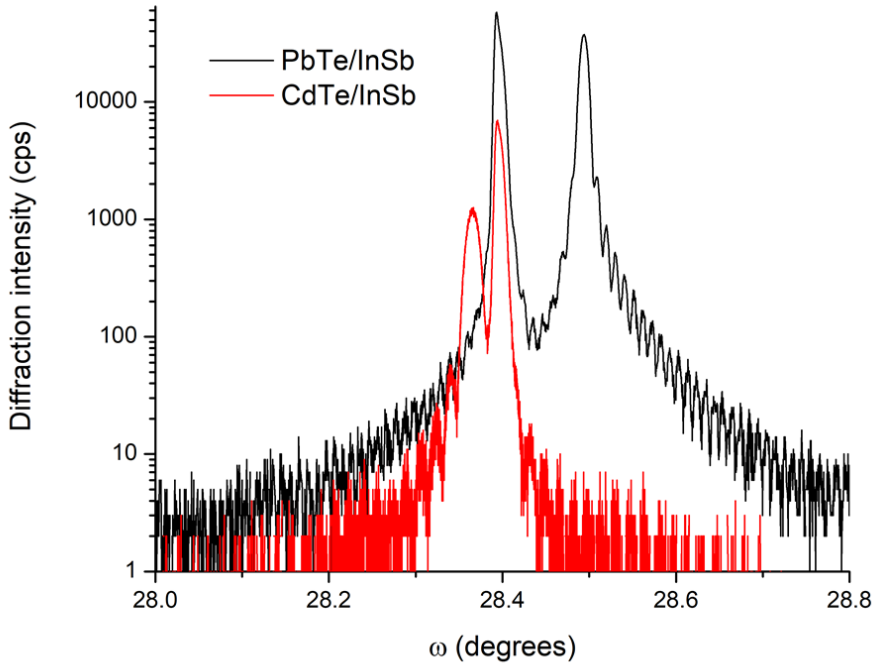

Fig. 49: (004) XRD scan of 500 nm PbTe (black) and 300 nm CdTe (red) heterostructures grown on (100) InSb substrates.

XRD results of the first preliminary PbTe growths, shown in figure 50, demonstrate that even with the different crystal structures, a high-quality rock-salt crystal layer can be grown directly on a zincblende III-V substrate such as InSb or by using a lattice-matched II-VI buffer layer with a common group-VI atom. Additionally, a strong diffraction peak is observed in the (002) plane, which should be very weak for InSb and CdTe crystals but contributes strongly to constructive interference in the rock-salt unit cell, certifying that the PbTe portion of the heterostructure has a different crystal structure. TEM images of the PbTe/CdTe heterostructures grown on InSb indeed confirm that the crystal structure changes from zincblende to rock-salt at the interface. No (002) InSb peak is noticeable in the scan because the difference in atomic scattering factor difference between In and Sb is

too small. Additionally, the XRD peak FWHM of the PbTe grown on InSb is slightly smaller than the PbTe grown on CdTe, corresponding to a higher-quality PbTe layer grown directly on InSb compared to layers which use a CdTe buffer layer. The TEM images in figure 51 show the heterocrystalline interface between PbTe and CdTe. Although the two materials have different crystal structures and a large thermal expansion mismatch, flat interfaces can be achieved for PbTe growth on CdTe. Further studies are needed to determine the appropriate growth conditions for CdTe growth on PbTe layers, specifically the interface termination and the initial growth temperature. The dislocations seen in the top layers of the heterostructure may also be caused by the thermal expansion mismatch between PbTe and the zincblende crystals, which could cause dislocations to form after the growth as the substrate is cooled from the growth temperature to room temperature. The thermal expansion coefficient of PbTe is 2.7E-5 K^{-1}, much larger than CdTe (4.7E-6 K^{-1}) or InSb (5.4E-6 K^{-1}). This creates a strongly-varying temperature-dependent lattice mismatch between PbTe and the zincblende crystals which can affect the structural and optical properties in numerous ways, as will be discussed shortly. If the thermal expansion mismatch can be mitigated, LWIR CdTe/PbTe DBRs are possible on InSb substrates, which could be relevant to InSb-based and HgCdTe-based detector technology due to the extremely high refractive index contrast (over three times higher than GaSb/ZnTe) and close lattice match between the absorber materials. Other group-IV semiconductor materials, including Ge and Sn alloys, could also be incorporated into PbTe to examine their electrical and optical properties and the potential for heterovalent integration with III-V, II-VI, and IV-VI crystals.

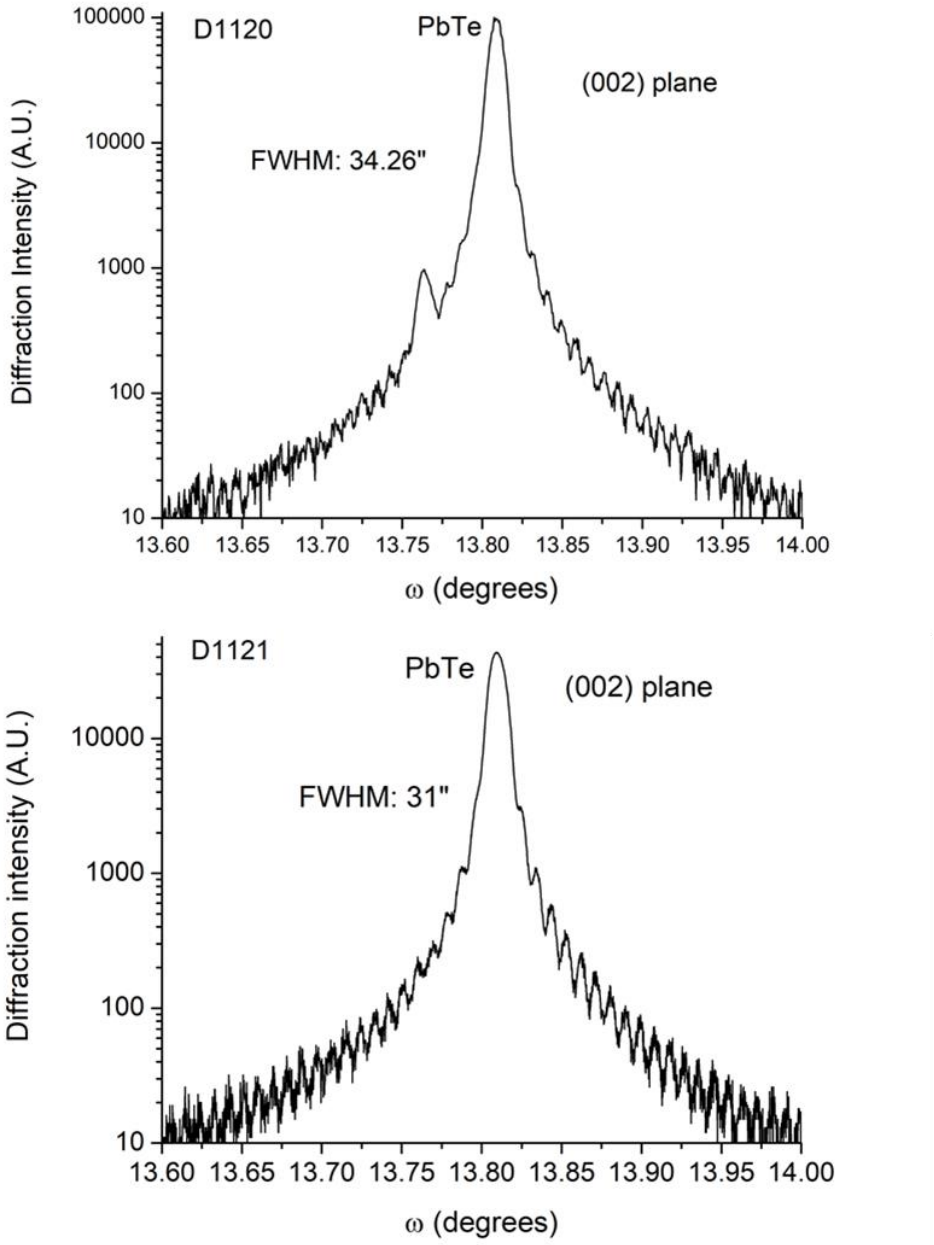

Fig. 50: XRD measurements of PbTe heterostructures grown on InSb. D1120 (top) is a 500 nm PbTe double heterostructure confined by 100 nm CdTe grown on (100) InSb, whereas D1121 (bottom) is simply 500 nm PbTe grown on (100) InSb without CdTe barrier layers.

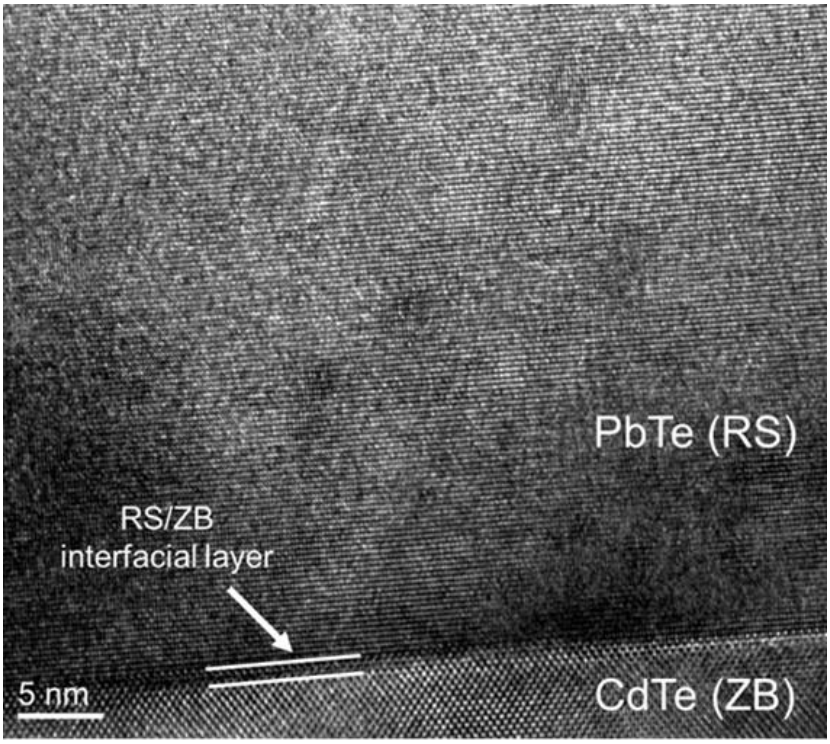

Fig. 51: TEM image of a PbTe/CdTe double heterostructure grown on (100) InSb. The interface roughness, on the order of 1-2 atomic layers, can be minimized by tuning the interface flux conditions. Sample prep and imaging performed by Dr. Brian Tracy.

PL measurements of the PbTe/CdTe quantum wells grown on InSb, seen in figure 52, show emission from both the PbTe quantum well and the CdTe/InSb heterojunction beneath the well layer. These two emission profiles can be distinguished not only from their slightly different peak energies, but also from the temperature trend of their peak energies. The CdTe/InSb heterojunction demonstrated a standard band gap temperature dependence seen in nearly every semiconductor material, where the band gap energy decreases as the temperature increases. The opposite case is true for the PbTe temperature dependence [108], which shows an increase in peak energy as the temperature increases. The anomalous temperature dependence of the lead salt band gaps has been attributed previously to an electron-phonon renormalization effect, as well as the temperature-

dependent lattice expansion [109]. As a general trend for PbTe/CdTe heterostructures, the optical emission strength dropped with thicker PbTe layers. This could possibly be due to the thermal expansion difference between the lead chalcogenides and zincblende crystals, which is large enough to possibly cause dislocations to form in thicker PbTe layers grown on InSb substrates. For example, the expected bulk lattice mismatch between PbTe and InSb will be 0.578 % at the growth temperature of 280 °C, but shifts to -0.274 % at room temperature and further to -1.23 % at 12 K where the PL measurements are measured [110]. The lattice mismatch between PbTe and InSb is calculated for some notable temperatures and shown in table 5. Therefore, for PL measurements of PbTe/CdTe/InSb heterostructures, room-temperature measurements should be made first before measuring at cryogenic temperatures since the low temperatures aggravate the lattice mismatch between the PbTe and the zincblende materials and can introduce more dislocations into the system that were not present after the growth. The number of dislocations can be estimated by making the assumptions that the lattices are completely relaxed and the strain is uniform throughout the crystal lattice, while in general the layer will only relax after the strain energy becomes too large to retain a coherent epitaxial layer, and the strain relationship of the crystal lattice requires a tensor to properly calculate the strain in each direction. Therefore, we can define equations 11-13.

$$f = \frac{a_{epi} - a_{sub}}{a_{sub}} \tag{11}$$

$$d_{dislocation} = \frac{a_0}{f} \tag{12}$$

$$d_c \sim \frac{1}{f}\ (monolayers) \tag{13}$$

The lattice constants between InSb, CdTe, and PbTe are plotted in figure 53, and it is clear that the lattice parameter of PbTe can shift a large amount compared to InSb and CdTe over a large temperature range, which can affect the growth and the characterization results. The calculated critical thickness and dislocation density ($=1/d_{dislocation}^2$) is shown in figure 54, and clearly the lattice mismatch between InSb and PbTe would cause complete relaxation for even relatively thin films at temperatures approaching 0 K. The thicker quantum wells with 40 nm PbTe layers emitted multiple peaks with a convoluted temperature dependence which converged into a single emission peak around 85 K, as seen in figure 55. This thickness dependence on the PL emission properties, including the multiple peaks in thicker layers, has been noticed before in PbTe/CdTe heterostructures grown on lattice-mismatched GaAs substrates [111]. The thermal expansion mismatch also affects the PL emission properties of the PbTe quantum well, which alters the deformation potential of the PbTe layers at different temperatures and can influence the ground state energy for thin layers. The strain in the PbTe lattice affects the band gap energy of the material since the deformation potential adds a perturbation to the Hamiltonian which alters the band structure of the material [112], resulting in a smaller-than-expected slope for PbTe grown on InSb when plotting the peak emission energy against the temperature. This can be seen in the plots of the peak energy of the quantum wells, seen in figure 56, where the emission energy of the 40 nm PbTe quantum well increases about twice as fast for a given change in temperature compared to the trend seen in the thinner 6 nm quantum wells. Additionally, similar to the InSb/CdTe superlattices, the samples that had XRD and RHEED data corresponding to low crystalline quality tended to have more intense PL signals, suggesting a disconnect between structural and optical

quality similar to the trend seen in the InSb/CdTe superlattices mentioned in the previous section.

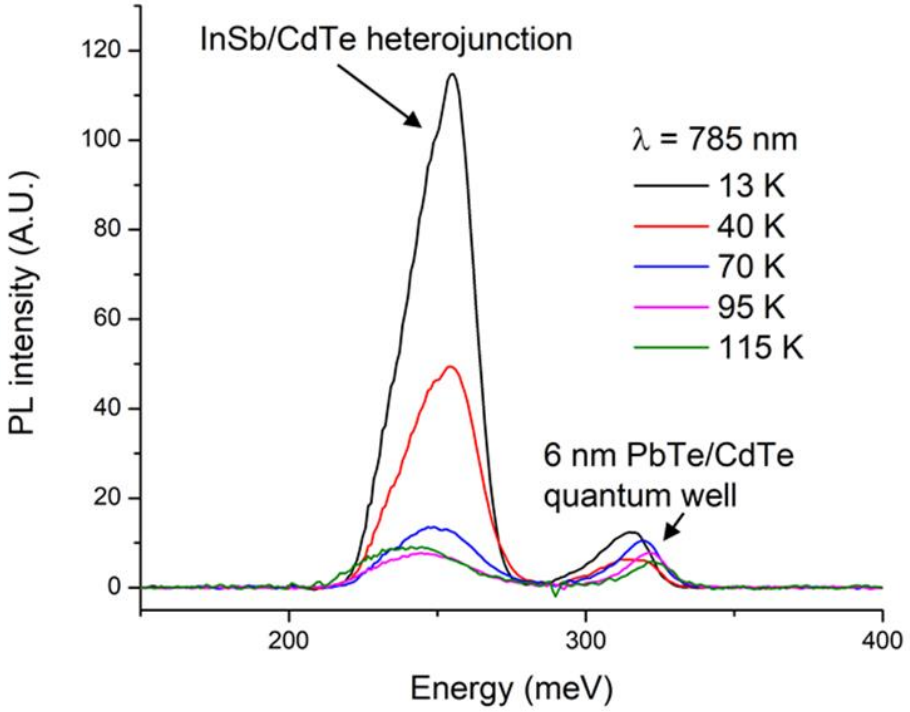

Fig. 52: PL spectrum of a 6 nm PbTe/CdTe quantum well grown on an InSb substrate. The stronger, low energy peak is from the InSb/CdTe heterojunction which has a standard temperature shift, whereas the peak associated with the PbTe quantum well shows an increase in peak energy as the temperature is increased.

Table 5: Lattice mismatch, theoretical critical thickness, and calculated defect separation for completely relaxed PbTe grown on InSb.

Temperature (K)	PbTe/InSb lattice mismatch (%)	Calculated critical thickness (nm)	Dislocation separation (nm)
1	-1.27	2.51	5.03
100	-0.937	3.42	6.84
273	-0.358	9.01	18.0
381	0.000972	1260	2520
550	0.566	5.77	11.5

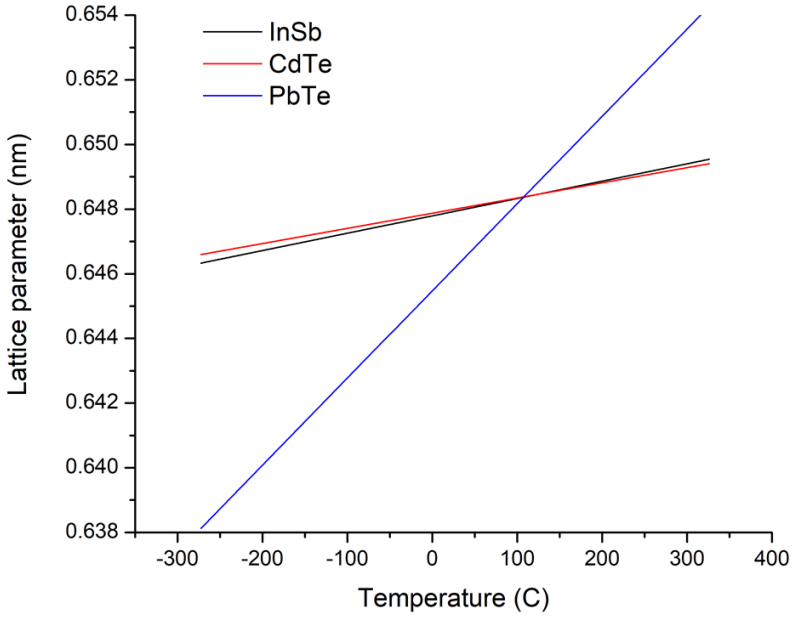

Fig. 53: First-order extrapolation for the lattice expansion of InSb, CdTe, and PbTe as a function of temperature. The lattice parameter of all three materials converge at about 107 °C, and the PbTe lattice will experience tensile strain when cooling past this temperature after growth at 280 °C.

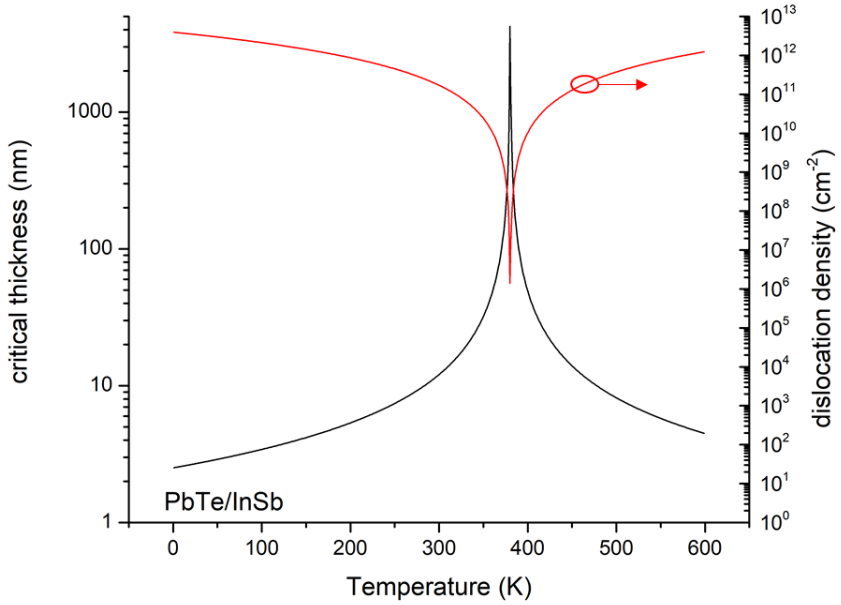

Fig. 54: Calculated dislocation density and critical thickness of PbTe grown on InSb as a function of temperature. In reality, for thicker PbTe films, the temperature change can cause the layer to relax or crack instead of forming dislocations.

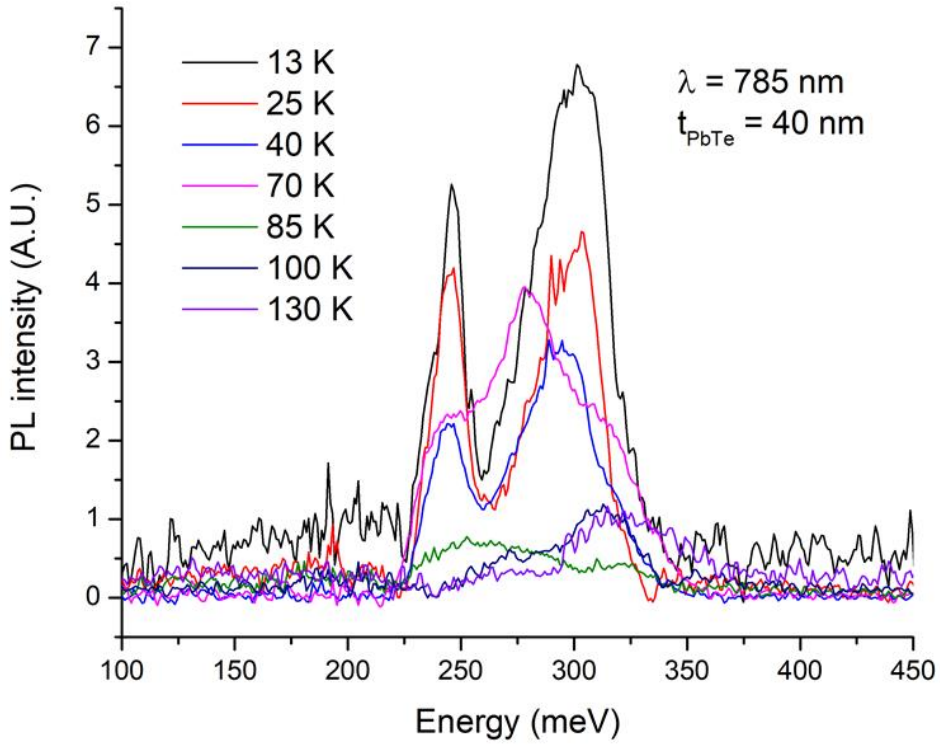

Fig. 55: PL spectrum of a 40 nm PbTe/CdTe quantum well grown on a (100) InSb substrate. The emission intensity of the individual peaks is reduced compared to the single peak observed from the 6 nm quantum well sample.

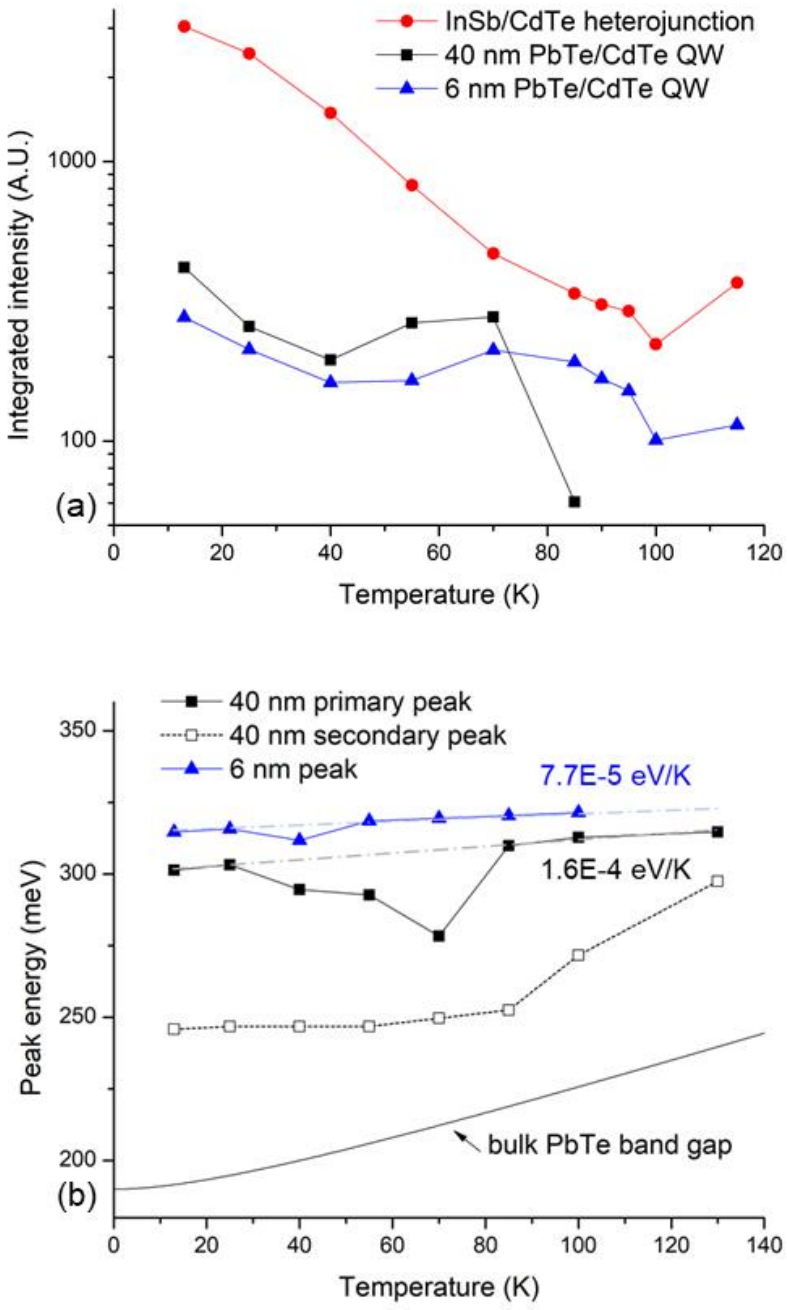

Fig. 56: (a) Integrated intensity and (b) peak energy temperature trend from the PbTe/CdTe quantum well samples grown on InSb substrates.

Further exploration of the heterovalent and heterocrystalline quantum wells is necessary to improve the interface quality and optical emission profile from heterovalent heterostructures grown on InSb substrates. Fine-tuning of the V/III ratio at lower temperatures is critical for improving the InSb/CdTe heterojunctions, particularly since Sb sticks to CdTe surfaces at low temperatures which can form uneven interfaces and poor InSb epilayers. The material quality of the PbTe layers can be enhanced if the Pb/Te stoichiometry can be more precisely calibrated to control the structural and optical properties of the PbTe films [113]. The PbTe/InSb and PbTe/CdTe interfaces require individual optimization, and the ordering of the materials may also change the optimal growth conditions. This can be seen in figure 57 where a significant difference is evident in the material quality between the top and bottom CdTe layers even though both layers had similar growth conditions. The dislocations seen in the PbTe/CdTe heterostructures could also be aggravated by post-growth compression of the PbTe, and therefore a maximum thickness of the IV-VI layers must exist where cracking due to the thermal mismatch may occur when the substrate is cooled after the growth. Additional studies of the structural integrity of PbTe films with varying thicknesses under different temperatures could help to illuminate potential solutions for mitigating the thermal expansion mismatch by tuning the growth conditions or layer geometry. All of these factors must be kept in mind when designing a growth structure that contains the III-V, II-VI, and IV-VI materials.

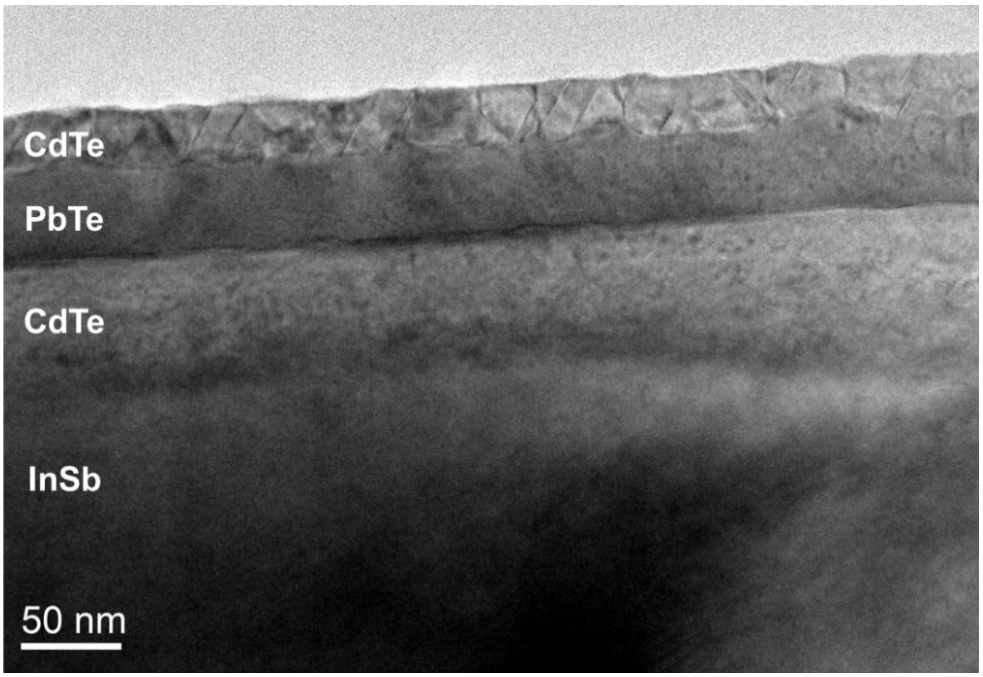

Fig. 57: TEM image of a PbTe/CdTe quantum well sample, where the bottom CdTe and PbTe layers are nearly defect-free, but the top CdTe layer contains a multitude of propagating defects mostly attributable to the uneven top surface of the PbTe layer. Sample prep and imaging performed by Dr. Brian Tracy.

The quantum well emission energies were calculated by numerically solving the transcendental solutions to Schrödinger's equation for a finite potential well between the first electron and heavy-hole energy states in the conduction and valence bands, respectively. The wavefunction of the bound states (i.e. for $E < V_0$) inside the well can be described by equations 14-15, where the even and odd solutions correspond to the cosine and sine portions of the wavefunction, respectively [114].

$$\psi(x) = ASin(kx) + BCos(kx) \tag{14}$$

$$k = \sqrt{\frac{2m(-V_0 + E)}{\hbar^2}} \tag{15}$$

Where A and B are normalization constants. Similarly, equations 16-18 describe the particle outside of the well.

$$\psi(x) = Ce^{\kappa x} \left(x < -\frac{d}{2}\right) \tag{16}$$

$$\psi(x) = De^{-\kappa x} \left(x > \frac{d}{2}\right) \tag{17}$$

$$\kappa = \sqrt{\frac{2mE}{\hbar^2}} \tag{18}$$

Figure 58 illustrates this fundamental case, where both the electron and hole are energetically separated in a quantum well with different potential barriers for each particle. Since both $\psi(x)$ and $d\psi(x)/dx$ must be continuous at the boundaries of the well, we can write equations 19-22 for the even solution.

$$BCos\left(-\frac{kd}{2}\right) = Ce^{-\frac{\kappa d}{2}} \left(x = -\frac{d}{2}\right) \tag{19}$$

$$BCos\left(\frac{kd}{2}\right) = De^{\frac{\kappa d}{2}} \left(x = \frac{d}{2}\right) \tag{20}$$

$$-BkSin\left(-\frac{kd}{2}\right) = Cke^{-\frac{\kappa d}{2}} \left(x = -\frac{d}{2}\right) \tag{21}$$

$$-BkSin\left(\frac{kd}{2}\right) = Dke^{\frac{\kappa d}{2}} \left(x = \frac{d}{2}\right) \tag{22}$$

From this set of relations we can remove the normalization constants and solve for the energy of the particle inside the well. Equation 23 describes how the transition energy levels in the quantum well can be numerically solved as a function of energy with knowledge of the layer thickness (d), particle effective mass (m^*), and barrier potential height (V_0).

$$\kappa Tan\left(\frac{kd}{2}\right) = \sqrt{\frac{2mV_0}{\hbar^2} - k^2} \tag{23}$$

This relation can be numerically or graphically solved, and the two equations are illustrated in figure 59 for the first bound conduction band state of a PbTe/CdTe quantum well of various thicknesses. It is clear from plotting these equations as a function of energy that as the well width increases, the number of energy levels increases and the value of the first transition energy level decreases. The PbTe well thickness was compared to the confinement energy measured by the PL spectrum peak, but a large discrepancy was seen in the calculated and measured ground state energy. This is in contrast to, for example, the GaAs/ZnSe quantum well where the calculated emission energy closely corresponds to the peak PL emission energy. For the PbTe quantum wells, additional factors such as the thermal mismatch-induced strain and the carrier concentration can also significantly affect the peak emission energy and therefore calculations were consistently lower than the measured peak energy. Since electrons are confined in the conduction band and holes in the valence band of the quantum well, the values of m* and V_0 must be known for both particles to calculate the ground state energy level. Typically, these values can be found in the literature, but in general the effective masses of carriers in a material are found with a number of different methods, most commonly with cyclotron resonance. The conduction and valence band offsets, which form the potential barrier V_0, can be experimentally verified with x-ray photoemission spectroscopy. While the band offsets of a heterojunction can be tested experimentally, the actual values can change depending on several different conditions such as the substrate orientation or the interface termination. This is particularly true for heterovalent heterojunctions, where charged states at the interface can alter the

bonding arrangement and thereby change the band alignment between the III-V and II-VI materials.

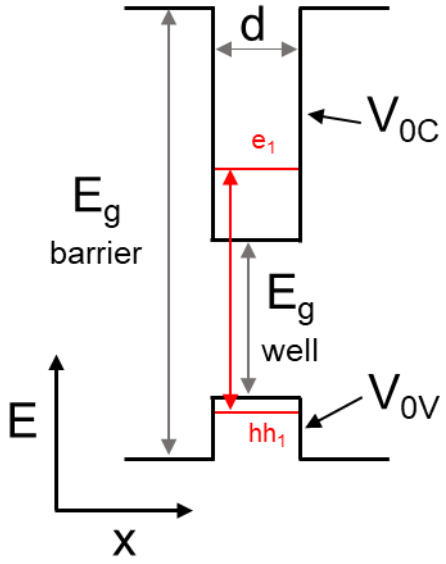

Fig. 58: Schematic of the ground-state energy levels in a quantum well structure. For the transition energy calculation, the energy separation was calculated between the first bound electron state in the conduction band and the first bound heavy hole state in the valence band.

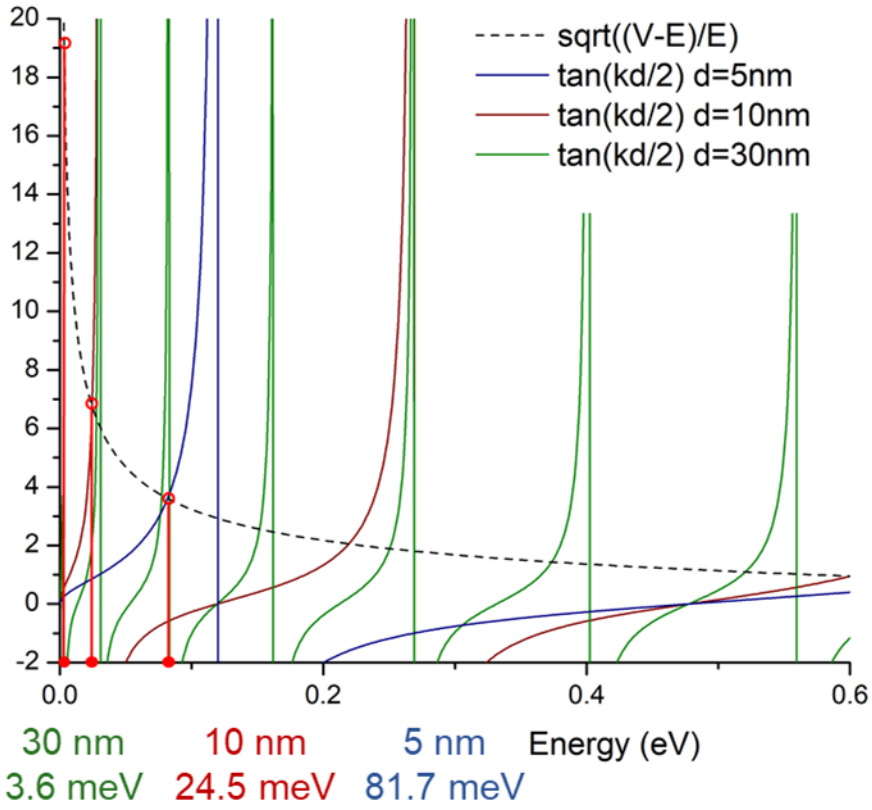

Fig. 59: Plot of the two sides of equation 23 for the conduction band of a PbTe/CdTe quantum well with widths between 5, 10, and 50 nm. The first bound states for each well width are marked at where the values of both equations are equal.

CHAPTER 5

POTENTIAL APPLICATIONS: DISTRIBUTED BRAGG REFLECTORS

DBRs designed to reflect mid-IR wavelengths were grown using alternating layers of lattice-matched II-VI and III-V materials with a high refractive index contrast. These high-precision reflectors are critical for confining light within epitaxial structures, such as VCSELs or resonant cavity detectors. The peak reflectance wavelengths for state-of-the-art DBRs are currently being pushed into the mid-IR spectral region for chemical and temperature sensing applications [115]. Optical feedback, for example, is required to promote stimulated emission and wavelength selectivity within the laser cavity and is the major difference between laser and LED structures. The high reflection in these structures can reduce the number of laser modes emitted from a VCSEL, which would enhance the finesse of the device, or alternatively, reduce the required thickness of the absorber layer of a detector, which would help to minimize non-radiative Shockley-Read-Hall (SRH) recombination in the absorber and enhance the operating speed of the device. The light which penetrates the structure experiences Fresnel reflection at the interface between the two layers, and the reflection is significantly enhanced at the interface when the light travels an optical path length of $\lambda/4$ through the material so that the reflected waves experience constructive interference, as shown in figure 60. By stacking alternating $\lambda/4$ layers with a high refractive index contrast, specific wavelengths can be selectively reflected and trapped in the cavity layer. The cavity layer for an IR device is generally a narrow-band gap active layer with a thickness of $\lambda/2$ confined on both sides by DBRs which are designed to reflect a peak wavelength corresponding to the desired optical mode. The thickness of the cavity layer is selected so that a particular optical mode experiences

constructive interference in the structure. This confined optical mode leads to low energy loss and high precision, making optical cavity devices desirable for detectors or emitters, or for any other applications which require thin active layers, optical feedback, or a very small detection or emission bandwidth. By utilizing lattice-matched II-VI and III-V materials, the refractive index contrast can be significantly increased compared to isovalent combinations of lattice-matched materials, which can improve the appeal of DBRs for IR wavelengths since mirrors with high reflectivity across a wide wavelength range can be grown epitaxially with much thinner DBR layers due to the high reflection at each interface. Additionally, the thinner total structure, along with the wide band gap and the self-compensating nature of the defects in II-VI materials, reduces the absorption in the layers attributed to the penetration depth and free carriers.

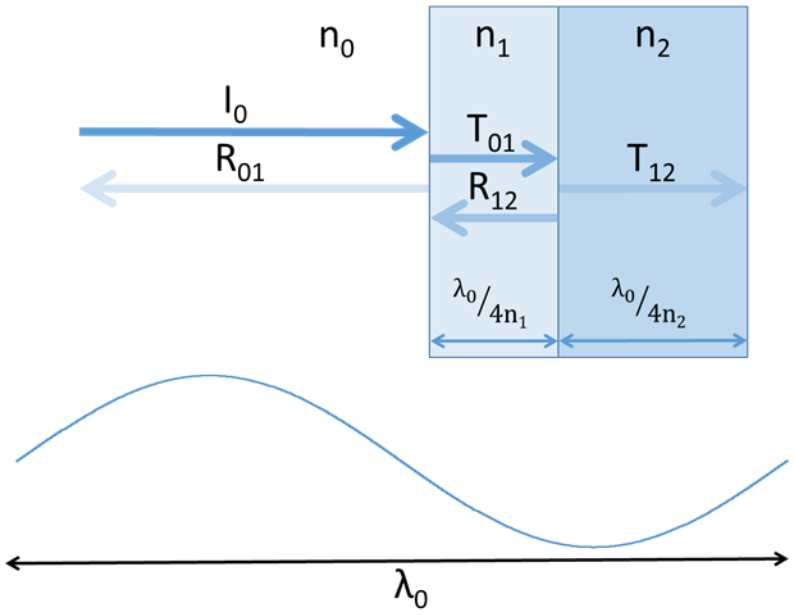

Fig. 60: Schematic illustrating Fresnel reflection and transmission through a stack of dielectric materials with different indices of refraction. The case of $n_1 >> n_2$ is ideal for higher reflection because of the large refractive index contrast between air (n=1) and the high-index top layer.

The DBR and optical cavity structures were simulated in MATLAB by solving the Fresnel equations for plane waves at normal incidence to calculate the fraction of light reflected for each wavelength [116]. The Fresnel equations can be derived directly from the Maxwell-Faraday equation by solving for the electric and magnetic components of the wave at every interface in the DBR structure, see equations 24-28.

$$\bar{E} = E_0 e^{i(\bar{k}\cdot\bar{r}-\omega t)} \tag{24}$$

$$\bar{B} = B_0 e^{i(\bar{k}\cdot\bar{r}-\omega t)} \tag{25}$$

$$\nabla \times \bar{E} = -\frac{\partial \bar{B}}{\partial t} \tag{26}$$

$$\frac{\partial \overline{E_x}}{\partial z}\hat{y} = -i\omega \overline{B_0} e^{i(\bar{k}\cdot\bar{r}-\omega t)} \tag{27}$$

$$k = \frac{\omega \widetilde{n_r}}{c} \tag{28}$$

Where *k* is the wavevector, which is an inverse function of the wavelength, and *r* is the distance traveled with both vectors pointing in the direction of propagation under the assumption that there is no magnetic polarization at the interfaces. If the **E** and **B** components of the electromagnetic wave are perpendicular, then the vector components of the cross product can be ignored and the magnitude of the waves can be described as the scalar relation in equation 29.

$$ikE_0 e^{i(kx-\omega t)} = -i\omega B_0 e^{i(kx-\omega t)} \tag{29}$$

And therefore, the relationship between the magnitude of the electric and magnetic components of the EM wave can be written as equation 30.

$$E_0 = -\frac{\omega}{k} B_0 = -\frac{c}{n_r} B_0 \tag{30}$$

With the assumptions that the medium is non-magnetic, the individual DBR layer thicknesses are not significantly longer than the wavelength, and the magnetic permeability of both materials is unity, then it is helpful to write the magnetic component as the **H** field instead of the **B** field since the influence of the magnetic properties of the materials can be neglected. This simplifies the equations while reminding us that we have to consider both the electric and magnetic components of the electromagnetic wave. Additionally, the index of refraction and the speed of light can be rewritten in terms of the magnetic and electric permeability of the material. This allows the magnitude of the **E** and **B** vectors to be related by the characteristic admittance η_0, and the refractive index of the medium as defined in equation 31.

$$E_0 = -\frac{B_0}{\sqrt{\epsilon_r \epsilon_0 \mu_0}} = -\frac{\mu_0 H_0}{\sqrt{\epsilon_r \epsilon_0 \mu_0}} = -\frac{\eta_0}{n_r} H_0 \tag{31}$$

Where the **H** field is simply $\mathbf{B}/\mu_0$, η_0 is $\sqrt{(\mu_0/\epsilon_0)}$, and n_r is defined as $1/\sqrt{\epsilon_r}$. When light passes through a layer of material thinner than the wavelength of the light, then the magnitude of the wave at the second interface can be described by applying a phase shift δ to the original state of the wave, as in figure 61.

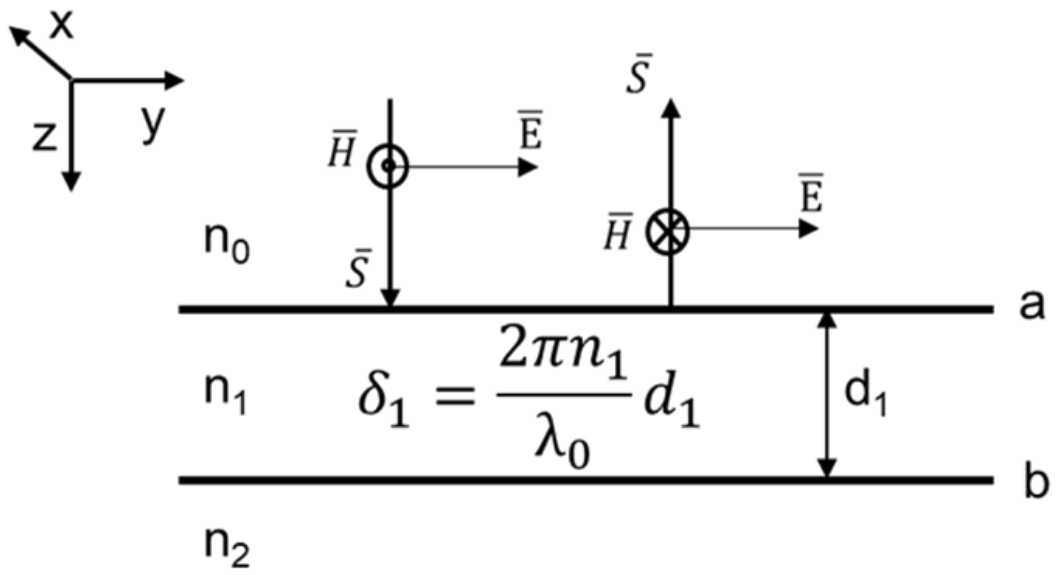

Fig. 61: Illustration of a light wave of a particular energy in a dielectric medium. The wave experiences a phase shift delta due to the optical path length, as well as an exponential decay from the absorption in the medium, both of which can be completely described by the index of refraction in non-magnetic materials.

If the materials are not magnetic, and the layers are sufficiently thin, then the only difference in the phase shift through the layers for different wavelengths is contained in the refractive index dispersion. To find how the energy density changes as the light travels through the medium, we need to look at the Poynting vector S which describes the energy flux of the electromagnetic wave. Also, the refractive index is generally a complex number, where the imaginary part is defined as the extinction coefficient and determines the absorption coefficient and the exponential decay of a plane wave in a uniform material, as described by equations 32-35.

$$\widetilde{n_r} = n_r + i\kappa \tag{32}$$

$$I = \overline{\langle S \rangle} = \frac{n_r \epsilon_0 c}{2} |E|^2 \tag{33}$$

$$I(x) = \frac{n_r \epsilon_0 c}{2}\left(E_0 e^{i(kx-\omega t)} * E_0^* e^{-i(k'x-\omega t)}\right) \tag{34}$$

$$\frac{I(x)}{I_0} = e^{i\omega\left(\frac{1}{c}(n_r+i\kappa)x-t\right)} * e^{-i\omega\left(\frac{1}{c}(n_r-i\kappa)x-t\right)} = e^{\frac{-2\omega\kappa}{c}x} \tag{35}$$

From this we can define the absorption coefficient α as a function of the extinction coefficient of the material as in equation 36.

$$\alpha = \frac{4\pi\kappa}{\lambda} \tag{36}$$

Since the structure is consistently repetitive with only two distinct layer materials with corresponding thicknesses, we only need to describe two different electromagnetic phase shifts no matter how many layers are in the DBR stack. This phase shift correlates the propagation of the light in the epitaxial structure and, when combined with the dispersion and absorption in the material, can describe the fraction of reflected light across the entire electromagnetic spectrum. Both the magnetic and electric field magnitudes at each interface can be efficiently described with a matrix operator. Due to the repeating geometry of the DBR, only two different matrix operators are required to describe the behavior of the optical wave in the material. The matrix operations can then be repeated for each stack in the structure, resulting in a total description of the electromagnetic field magnitude at the top interface and therefore the ratio of reflected light for all wavelengths incident normal to the structure surface.

For a designated peak reflection wavelength, the thickness of each DBR layer is designed with the refractive index dispersion in mind to be exactly one-quarter of the desired wavelength in the material, described in equation 37.

$$d_1 = \frac{\lambda_{peak}}{4 \cdot n_{1,peak}} \tag{37}$$

This results in a destructive phase shift of π/2 over the optical path in the DBR layer. To calculate the transmission at each interface, the electric fields on each side of the interface are connected with a transfer matrix. The transfer matrix formalism is described in equation 38, where the transmitted electric and magnetic field components are tied to the incident side by multiplication through the 2×2 matrix operators.

$$\begin{bmatrix} E_1 \\ \eta_0 \cdot H_1 \end{bmatrix} = \begin{bmatrix} Cos(\frac{2\pi n_1 \cdot d_1}{\lambda_1}) & i \cdot Sin(\frac{2\pi n_1 \cdot d_1}{\lambda_1}) \Big/ n_1 \\ i \cdot n_1 \cdot Sin(\frac{2\pi n_1 \cdot d_1}{\lambda_1}) & Cos(\frac{2\pi n_1 \cdot d_1}{\lambda_1}) \end{bmatrix} \begin{bmatrix} E_2 \\ \eta_0 \cdot H_2 \end{bmatrix} = M_{1,2} \begin{bmatrix} E_2 \\ \eta_0 \cdot H_2 \end{bmatrix} \tag{38}$$

Each interface has its own matrix component, and the reflection is calculated by multiplying through the entire series of matrices, as in equations 39 and 40.

$$\begin{bmatrix} A \\ B \end{bmatrix} = \prod_{m}^{2N} (M_{m,m+1}) \begin{bmatrix} 1 \\ n_{sub} \end{bmatrix} \tag{39}$$

$$R(\lambda) = \left(\frac{1 - \frac{B}{A}}{1 + \frac{B}{A}} \right) \cdot \overline{\left(\frac{1 - \frac{B}{A}}{1 + \frac{B}{A}} \right)} \tag{40}$$

The transmission, reflection, and absorption properties of normal-incidence light through a DBR structure can be calculated with these equations and a computer model can be created with knowledge of the materials' refractive index and extinction coefficient, as well as their dispersion effects for different wavelengths. Text files for the refractive index dispersion are sufficient to explain a significant portion of the reflection and absorption due to band-to-band transitions. Clearly for maximum reflection, a high refractive index contrast is desired between the two materials, coupled with low extinction coefficients

which are manifested in the imaginary portion of the refractive indices. Also evident from a glance at the equations above is that DBRs for longer wavelengths require thicker layers to obtain high reflectance, so optical cavities composed of materials with a low refractive index contrast can become prohibitively thick, especially for devices operating in the MWIR or LWIR wavelength ranges. This issue gives these heterovalent DBRs a distinct advantage which could help to make resonant cavity technology relevant for MWIR and LWIR applications. As the refractive index contrast increases, the number of required stacks is reduced and the stop bandwidth of the reflection peak is enhanced. In addition, the higher band gap of the II-VI materials and the thinner structures help to reduce the below-band gap absorption in the DBR, which also enhances the peak reflection.

Below-band gap absorption due to the extinction coefficient and free carriers was accounted for in the DBR simulations. The absorption due to the extinction coefficient is an intrinsic property of the material and cannot easily be varied, but the free carrier absorption depends on the density of free carriers and their lifetimes in the material, and can vary significantly from sample to sample even for similar materials and growth structures. Due to the relatively large band gap of the II-VI materials, low carrier concentrations within the DBR layers can be achieved which can drive down the free carrier absorption and enhance the reflection of the structure. Additionally, the absorption can be noticeably reduced by designing the DBR such that the primary reflection surface is a low-carrier concentration II-VI layer since the largest portion of light is absorbed in the top DBR layer. The free carrier absorption for below-band gap photons can be described using equations 41 and 42.

$$\alpha_{FCA} = \frac{\sqrt{\varepsilon_0}\omega_p{}^2\lambda^2}{4\pi c^3\tau} \tag{41}$$

$$\omega_p = \sqrt{\frac{4\pi n q^2}{m^*\varepsilon_0}} \tag{42}$$

For longer wavelengths, we can see from these equations that the effective mass, carrier concentration, and carrier lifetime of the materials will affect the absorption in the DBR layers. Even if the layers are not intentionally doped, a perfectly pure lattice is energetically impossible and point defects (and therefore free carrier) will always be present in any material. The minimum number of carriers in the material tends to be reduced as the band gap of the material increases since a significant change in the Fermi energy is required to activate the defect levels in the material and the native defects present can keep the Fermi energy close to the center of the band gap. The radiative minority carrier lifetime in the material can be determined from time-resolved photoluminescence (TRPL) measurements. With this technique, the decay time of the minority carriers (electrons in p-type materials and holes in n-type materials) is measured by using a pulsed laser and a fast detector to observe the PL intensity decay as a function of time as illustrated by figure 62. The decay curve can be fitted with the exponential decay function in equation 43, where τ is defined as the radiative recombination lifetime or the average time required for an excited carrier to decay back to a non-excited state.

$$I(t) = I_0 e^{-t/\tau} \tag{43}$$

Accounting for absorption, the transfer matrix with the complex refractive index now becomes equation 44.

$$\begin{bmatrix} Cos\left(\frac{2\pi(n_1 + i\kappa_1)\cdot d_1}{\lambda_1}\right) & i\cdot Sin\left(\frac{2\pi(n_1 + i\kappa_1)\cdot d_1}{\lambda_1}\right)\Big/ n_1 \\ i\cdot n_1\cdot Sin\left(\frac{2\pi(n_1 + i\kappa_1)\cdot d_1}{\lambda_1}\right) & Cos\left(\frac{2\pi(n_1 + i\kappa_1)\cdot d_1}{\lambda_1}\right) \end{bmatrix} \begin{bmatrix} E_2 \\ \eta_0 \cdot H_2 \end{bmatrix} = M_{1,2} \begin{bmatrix} E_2 \\ \eta_0 \cdot H_2 \end{bmatrix} \quad (44)$$

Figure 63 shows the difference in the reflection spectrum with and without accounting for below-band gap absorption in the DBR layers. The simulated spectrum with absorption also accounts for the dispersion of the complex index of refraction over the range of simulated wavelengths. Clearly, the imaginary portion of the refractive index reduces the peak reflection, the stop-band width, and impacts the reflection spectrum significantly.

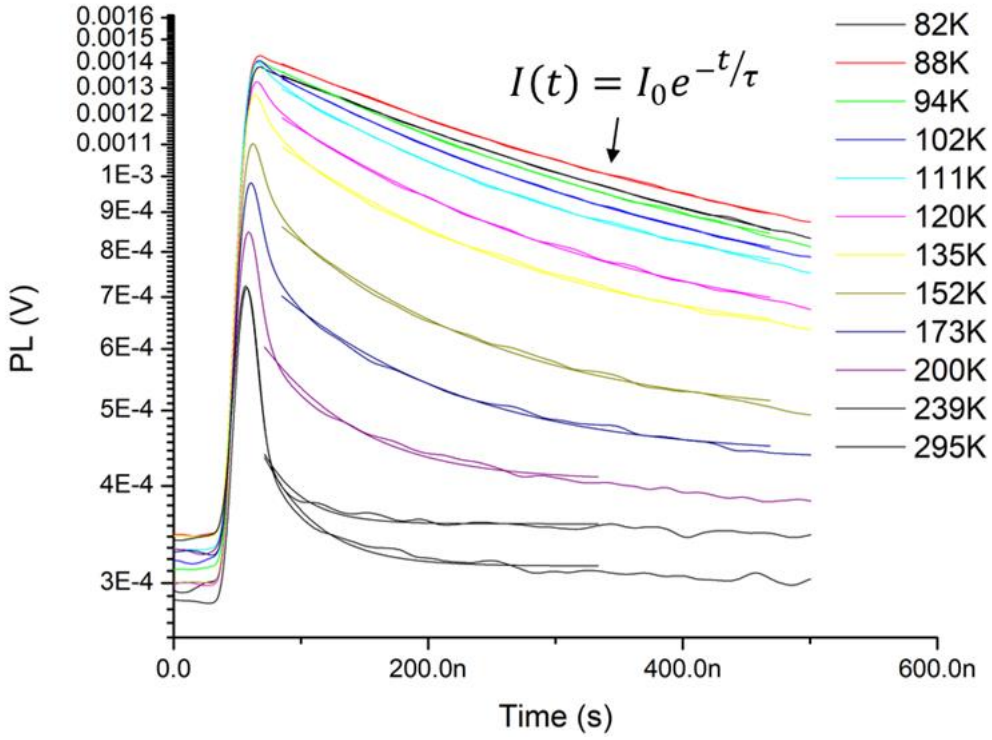

Fig. 62: Temperature-dependent TRPL decay curves and exponential fitting of a GaSb/ZnTe heterostructure. Measurements were made at AFRL in Kirtland AFB.

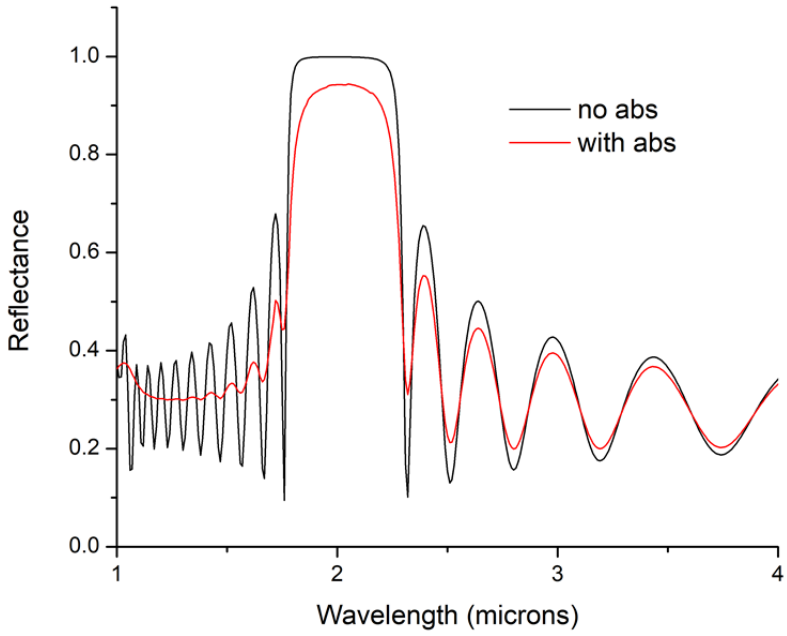

Fig. 63: Reflection spectra of a 10-pair GaSb/ZnTe DBR tuned for a peak reflectance of 2 microns with (red) and without (black) accounting for below-band gap absorption.

It is clear from figure 64 that the free carrier absorption increases significantly for longer wavelengths, and therefore the absorption coefficient of any material will increase with lower photon energies even below the band gap energy due to the absorption of free carriers. Consequently, the background carrier concentration in the mirrors of any mid- or long-wave IR optical cavity device will need to be suppressed to maintain a high peak reflection. For materials that are not intentionally doped, or for materials with narrow band gap energies, the total absorption in the DBR structure is dominated by the extinction coefficients as illustrated in figure 65. Wide band gap materials like ZnTe with a self-compensation mechanism have a distinct advantage as the background carrier concentration can be driven extremely low with careful control of the defect incorporation. Sources have reported background carrier concentrations in Te-rich ZnTe below 10^{10} cm^{-3}

[117], which would render the free carrier absorption insignificant even at very low photon energies. Integration of these II-VI materials with more commonly used IR materials could transform the scope of IR devices and push the viability of optical cavity structures to longer wavelength ranges unachievable with current III-V materials alone.

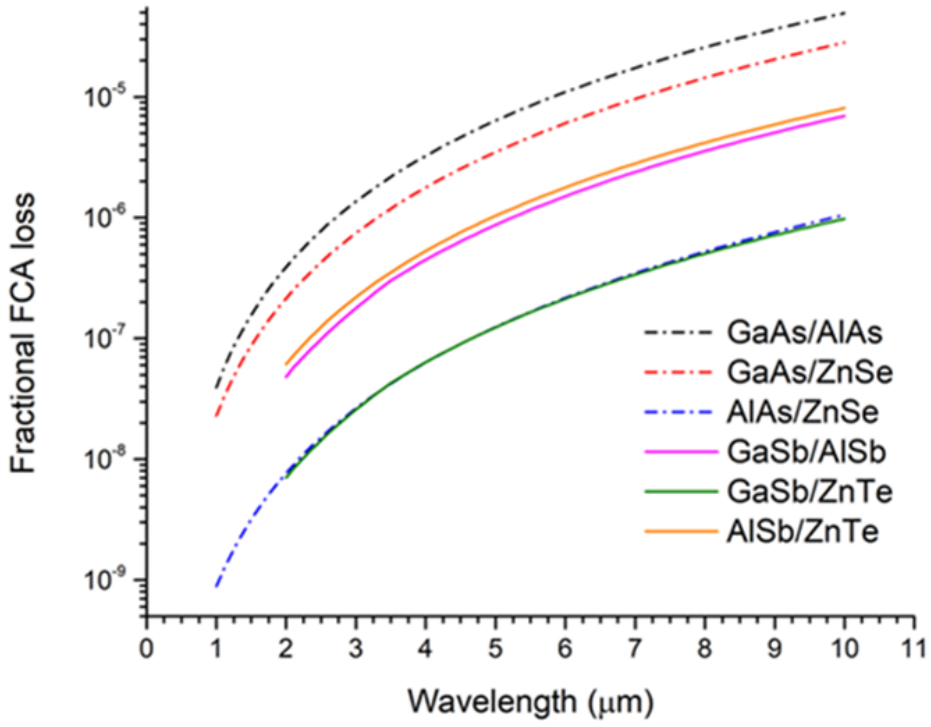

Fig. 64: Calculated fractional free carrier absorption in thick DBR structures with various materials lattice-matched to GaAs (dashed lines) and GaSb (solid lines). Carrier concentrations for each material were obtained from the minimum values found in literature.

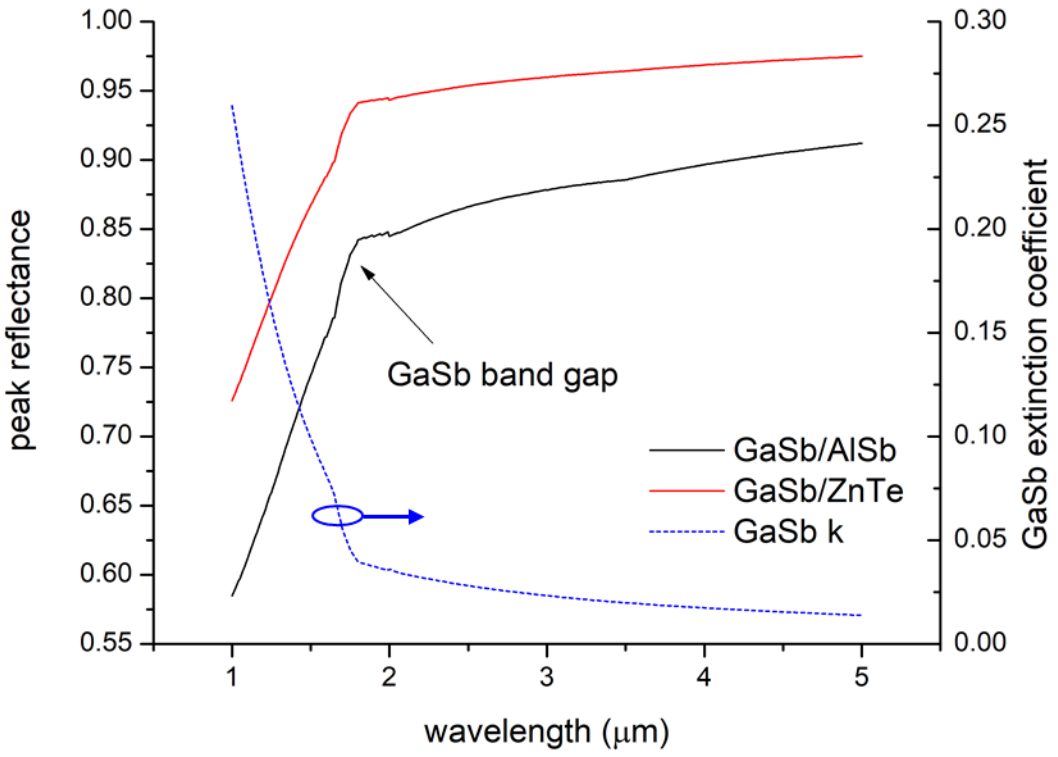

Fig. 65: Peak reflectance in thick GaSb/ZnTe and GaSb/AlSb DBRs plotted against the extinction coefficient dispersion of GaSb. The extinction coefficient of GaSb results in the majority of below-band gap absorption in both structures between the wavelengths of 2-5 μm.

Optical cavity structures, such as the one illustrated in figure 66, were modeled with the transfer matrix formalism that was used to calculate the DBR reflection spectrum, but a half-wavelength active cavity layer consisting of a narrow-band gap material is inserted between the mirrors, as described by equation 45.

$$d_c = \frac{\lambda_{peak}}{2 \cdot n_{r,cav}} \tag{45}$$

The active region must operate at wavelengths transparent to the bulk DBR materials, otherwise the parasitic absorption will render the DBR useless. The finesse, or Q-factor, of the cavity is inversely related to the FWHM of the absorption peak and is a critical

characteristic of any Fabry-Pérot cavity. High finesse optical cavities are required for single-mode lasers and high-precision chemical sensors, among other applications. The finesse is completely determined by the peak reflection of the DBR, as shown in equation 46.

$$F \equiv \frac{\pi\sqrt{R}}{1-R} = \frac{c}{2n_c \cdot d_c \cdot \Delta\nu_{FWHM}} \tag{46}$$

The finesse is a numerical representation of the energy lost to the mirrors for the peak wavelength, and therefore we can see in figure 67 that the finesse rapidly rises as the DBR peak reflectance approaches unity, signifying low parasitic absorption.

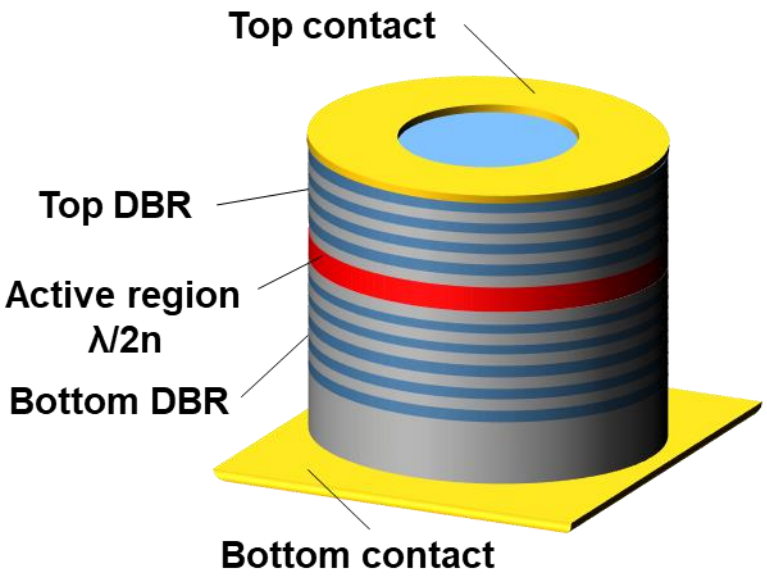

Fig. 66: A VCSEL device structure based on an optical cavity with DBRs.

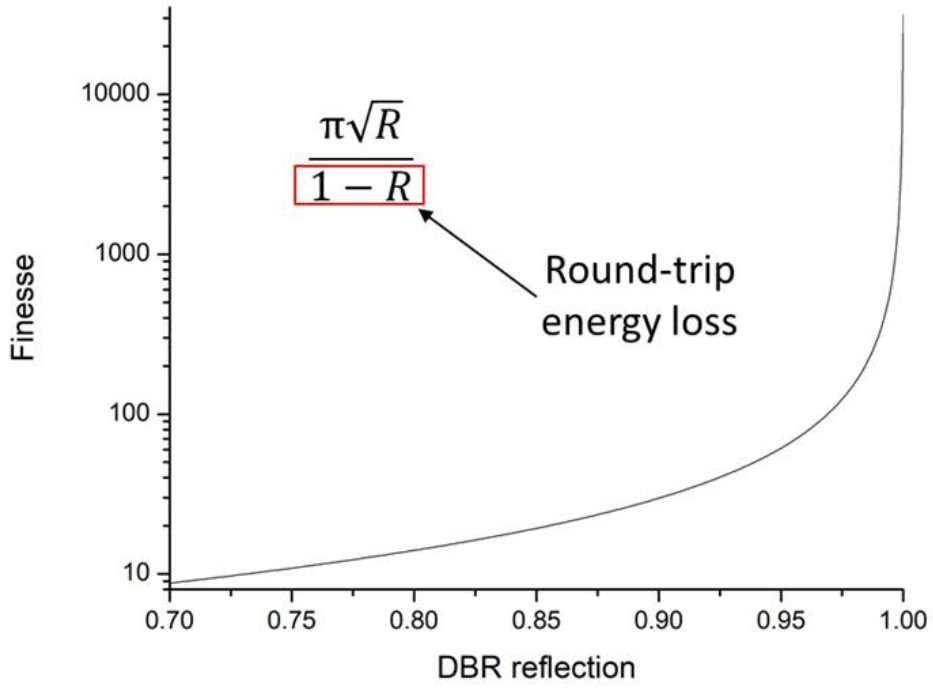

Fig. 67: DBR finesse as a function of the peak reflection. The finesse is generally measured for the target peak reflection wavelength.

Both isovalent and heterovalent DBR structures for MWIR applications were simulated using the transfer matrix formalism to illustrate the benefit of the large refractive index contrast between II-VI and III-V materials. The material system lattice-matched to GaSb substrates is a particularly good example since many MWIR devices are proposed and demonstrated for this lattice constant. The major issue with isovalent GaSb-based DBRs is the lack of a high-band gap III-V material with a low index of refraction to compliment the GaSb layers, with state-of-the-art devices utilizing GaSb-AlAsSb stacks which have a refractive index contrast of 0.56 at a wavelength of 2 microns. This pales in comparison to GaSb-ZnTe with a refractive index contrast of 1.04 at the same wavelength.

The benefits of this higher refractive index contrast are clear from figure 68, where essentially every theoretical aspect of an optical cavity structure is better with the heterovalent DBR. Table 6 shows a comparison of the calculated isovalent and heterovalent DBR thicknesses required to reflect a set percentage of light for different MWIR wavelengths. As the desired wavelength becomes longer, the DBR structures become unfeasibly thick, especially for the isovalent pair. From the calculations, it is clear that the required thickness of a DBR structure can be approximately halved by doubling the refractive index contrast.

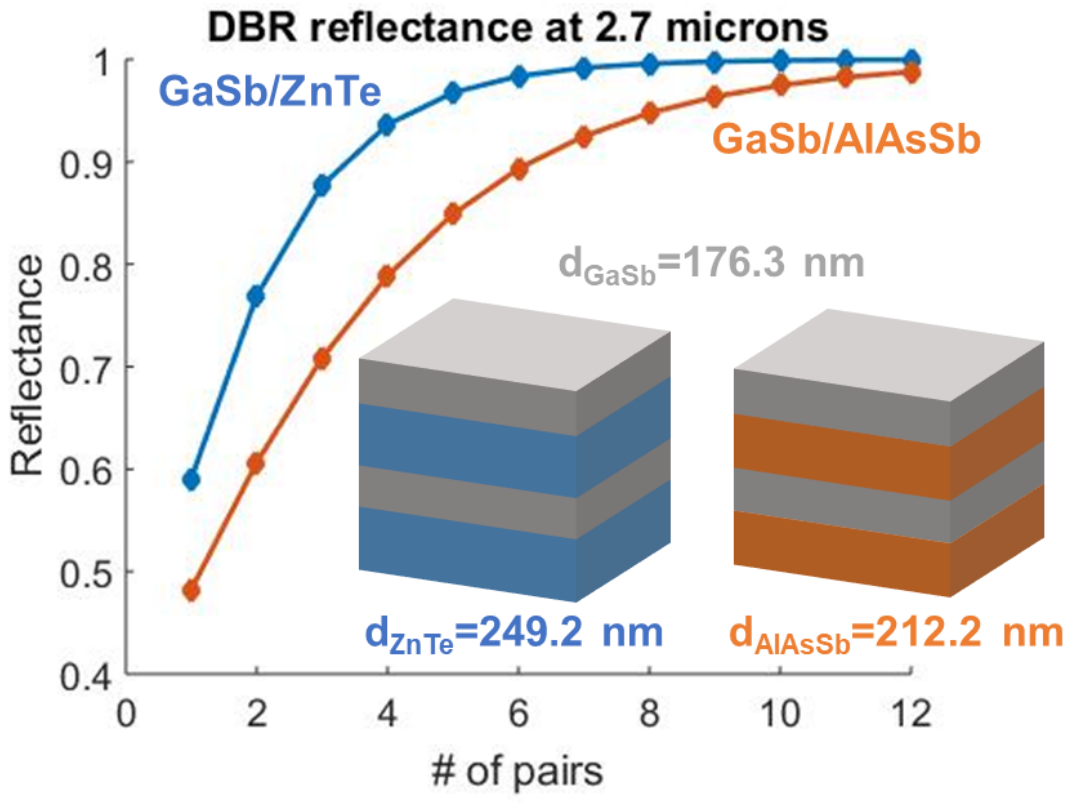

Fig. 68: Reflectance comparison of GaSb/ZnTe and GaSb/AlAsSb DBRs. The heterovalent DBRs reach a higher reflectivity than the isovalent DBRs for any given number of pairs due to the high refractive index contrast.

Table 6: Total structure thicknesses required for ultra-high reflection in GaSb/ZnTe and GaSb/AlAsSb DBRs.

	GaSb/ZnTe	GaSb/AlAsSb
Δn	**1.04**	**0.56**
Thickness for reflectance @ 2.5 μm		
99%	2843 nm	4833 nm
99.9%	4061 nm	7064 nm
Thickness for reflectance @ 3.5 μm		
99%	4448 nm	6426 nm
99.9%	6116 nm	10685 nm
Thickness for reflectance @ 4.5 μm		
99%	5650 nm	9166 nm
99.9%	7867 nm	13090 nm

Heterovalent DBR structures consisting of alternating ZnTe/GaSb layers were grown on (100) GaSb substrates in a single-chamber MBE system. A Zn overpressure was applied prior to initiating the ZnTe growth at a substrate temperature of 300 °C, and a 30 second Sb flux was used after the ZnTe layer growth to promote Sb-Zn bonding before starting the GaSb layer growth at a substrate temperature of 300 °C. The substrate temperature was then ramped during the growth to 500 °C at a rate of 30 °C/min, resulting

in a high quality GaSb layer. XRD and TEM measurements, shown in figure 69, present conclusive results that the interfaces are indeed abrupt and the material is nearly defect-free. This leads to an extremely high peak reflectance value as measured by FTIR reflectance spectroscopy. From the reflectance spectrum shown in figure 70, we can determine a stop bandwidth of 1.2 μm and a peak reflection value of 96.4 % for a DBR structure designed to reflect a wavelength of 4.6 μm with only 6 GaSb/ZnTe pairs. The results of the heterovalent DBRs far outpace those of isovalent III-V DBR structures, and further characterization is needed to determine the relevant thermal and electrical conductivity between the layers for device applications.

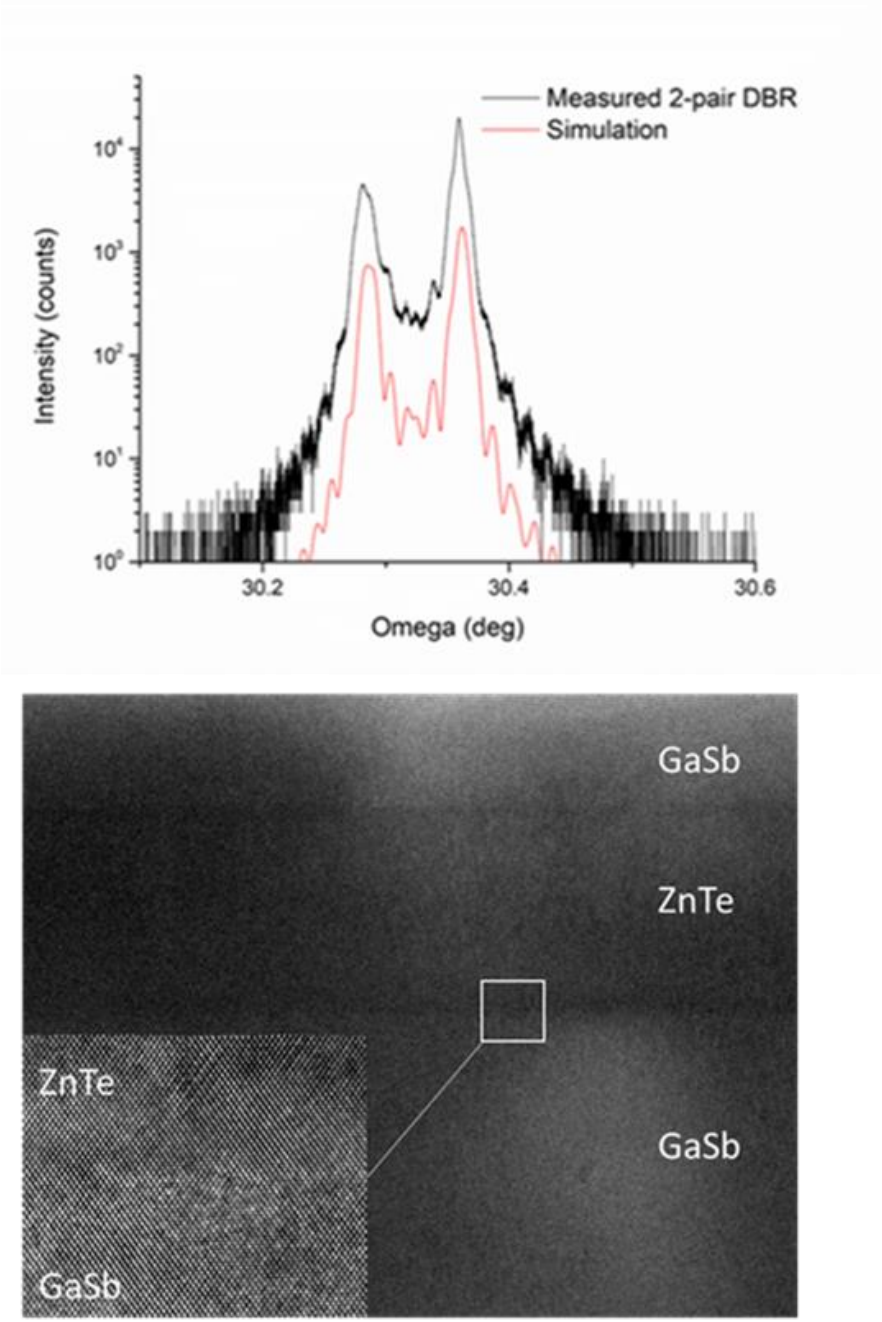

Fig. 69: TEM and XRD measurements of the GaSb/ZnTe heterovalent DBRs showing abrupt interfaces and virtually defect-free layers. Sample prep and imaging performed by Dr. Brian Tracy.

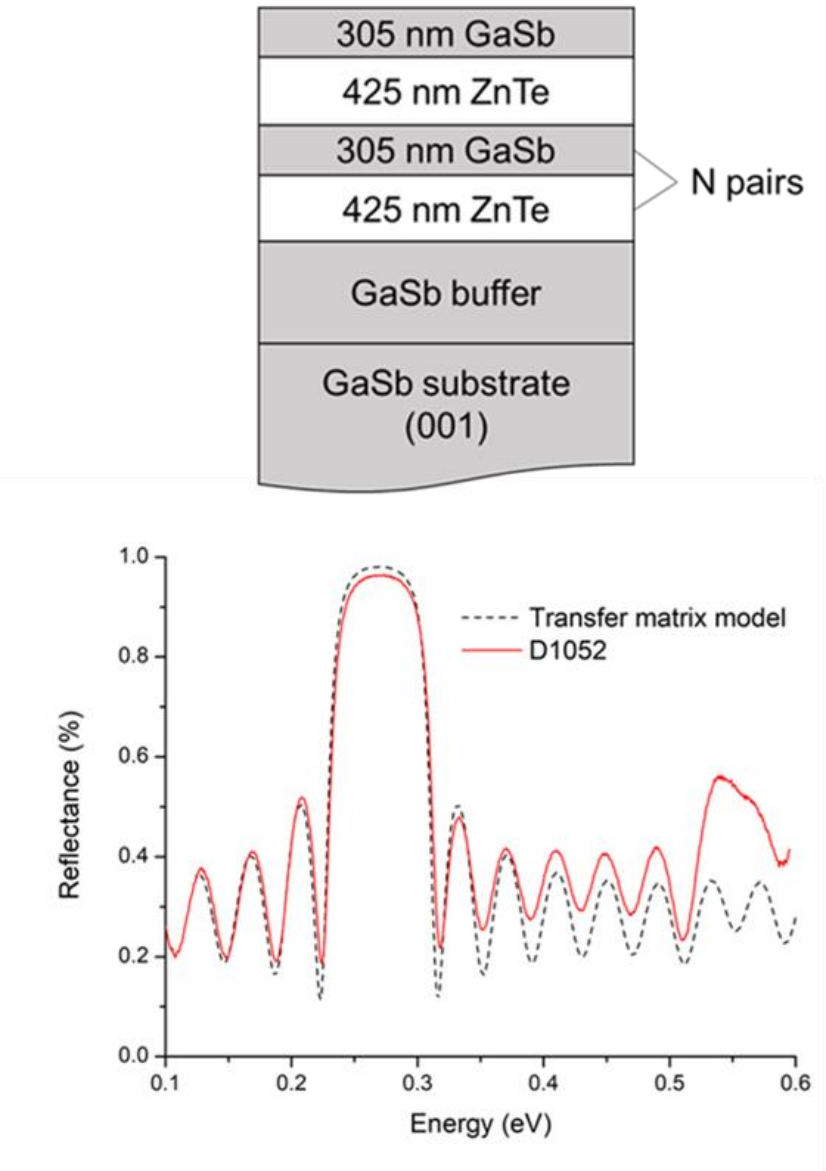

Fig. 70: Schematic growth structure and reflectance spectrum of a 6-pair GaSb/ZnTe DBR designed for reflectance at 4.6 μm.

In addition to the ZnTe/GaSb material system, other heterovalent material combinations can possibly be used to obtain high reflectance values for a range of wavelengths. For example, the CdTe/PbTe material system has a relatively high refractive index contrast of approximately 3.3 for photon wavelengths longer than 4 μm, which can

be used for longer-wavelength applications with a target photon energy low enough to avoid absorption in the narrow band gap PbTe layers. The key for a good DBR is to maximize the refractive index contrast between the two materials while limiting any parasitic absorption in the structure. Therefore, the choice of material depends strongly on the desired peak reflection wavelength since band-to-band recombination must be avoided above all else in the structure, as illustrated by figure 71. Other factors to remain mindful of when selecting the material combination include the lattice-match and the refractive index contrast between the two materials. The epitaxial compatibility between the materials is a key factor since DBR structures tend to be many microns thick and any defect formation or interface diffusion will undoubtedly destroy the delicate reflection profile of the structure. Table 7 shows the notable characteristics between relevant heterovalent material combinations for DBR structures, and from this table it is clear that the material parameters for the heterovalent combinations are more suitable for DBR structures compared to the isovalent combinations. While the GaSb/ZnTe material system has been demonstrated as a viable DBR for IR applications, other heterovalent materials have the potential to advance the epitaxial viability for IR technology at other lattice constants, such as the established IR device platform for HgCdTe and InSb lattice-matched to the 6.5 Å lattice constant.

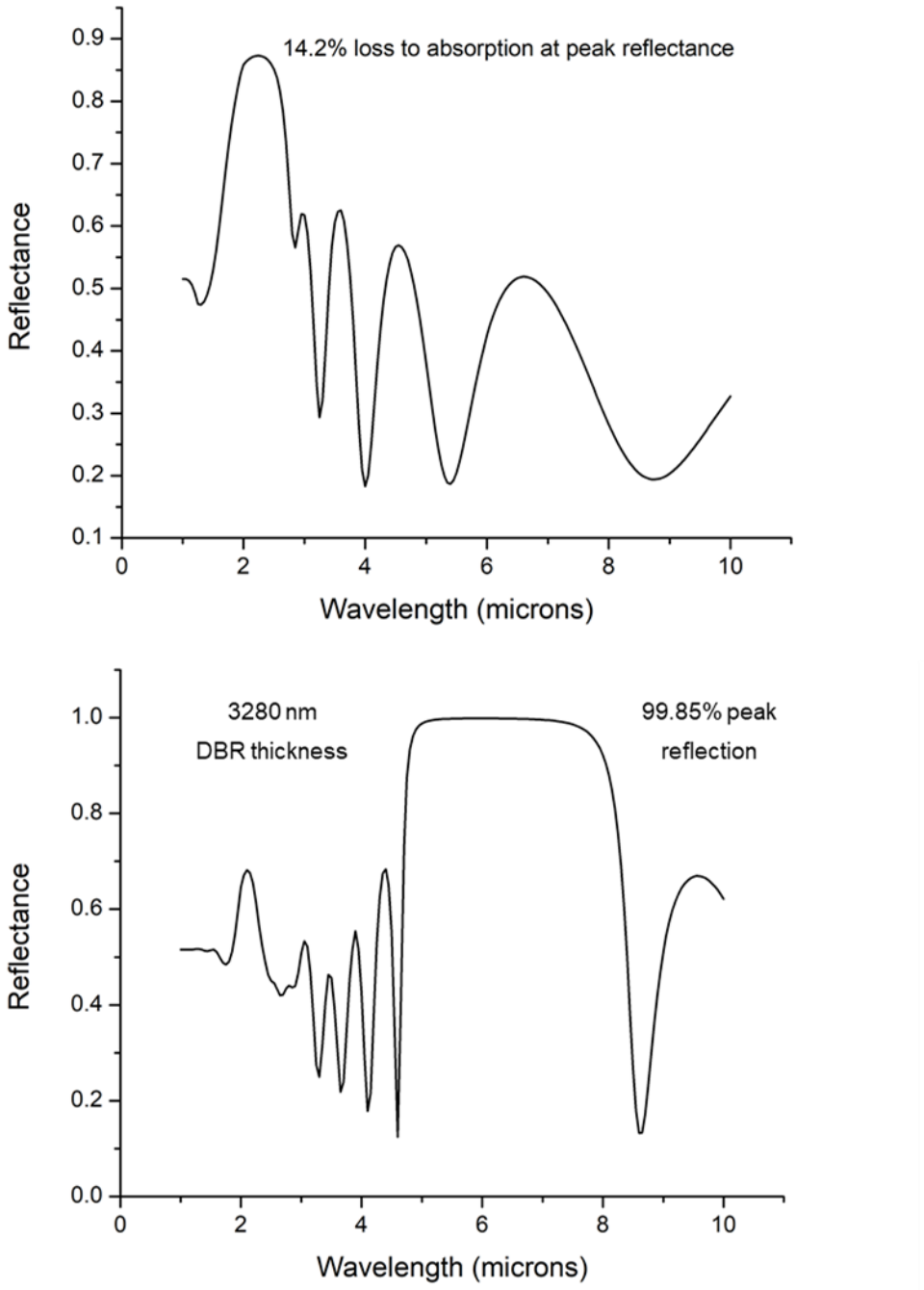

Fig. 71: Simulated reflection spectra of PbTe/CdTe DBRs tailored to reflect different wavelengths. Due to the narrow band gap of PbTe, a significant amount of absorption is experienced in these DBRs for shorter wavelengths.

Table 7: Material properties relevant to DBR design for various lattice-matched semiconductor combinations.

Heterojunction	Lattice constant (Å)	Refractive index (@ 2μm)	Band gap (eV)	Thermal expansion coefficient ($°C^{-1}$)
GaAs / ZnSe	5.653 / 5.668	3.34 / 2.45	1.52 / 2.82	5.73E-6 / 7.1E-6
GaAs / AlAs	5.653 / 5.661	3.34 / 2.88	1.52 / 2.17	5.73E-6 / 5.20E-6
InAs / CdSe	6.058 / 6.050	3.45 / 2.47	0.43 / 1.84	4.52E-6 / 4.28E-6
GaSb / ZnTe	6.096 / 6.101	3.90 / 2.72	0.73 / 2.26	7.75E-6 / 8.19E-6
GaSb / AlSb	6.096 / 6.136	3.90 / 3.21	0.73 / 1.58	7.75E-6 / 2.55E-6
InSb / CdTe	6.479 / 6.480	4.00 / 2.70	0.23 / 1.61	5.37E-6 / 4.5E-6
PbTe / CdTe	6.454 / 6.480	6.09 / 2.70	0.25 / 1.61	2.7E-5 / 4.5E-6

Since the semiconductors with large lattice constants also tend to have small band gaps, the 6.5 Å materials are the most intuitive choice for monolithically-integrated LWIR optoelectronic devices. As mentioned before, HgCdTe is the premier single-crystal IR detector material because it has a high absorption coefficient for LWIR radiation and can detect a relatively large amount of photons with a thin absorber. By incorporating DBRs with these devices, much thinner absorber layers would be required to completely absorb the relevant photons due to the multiple reflections and increased optical path length in the optical cavity structure. Because of this, SRH recombination, which is volume-dependent, can be reduced in the absorber layer and the response speed can be enhanced since the carrier transit time is inversely proportional to the thickness of the intrinsic region in the absorber. Since many HgCdTe detectors operate with a fully-depleted absorber layer, the depletion layer thickness will essentially be the same as the thickness of the HgCdTe layer.

Therefore, we can see how enhancing the absorption in the HgCdTe will enable a thinner absorber layer which will lower the transit time of the carriers in the absorber. Fast detectors are desirable to analyze high-frequency optical signals, which can enhance the frequency bandwidth of optical systems and increase the speed of optical communication equipment.

Absorption in heterovalent optical cavities was analyzed by simulating the reflection in the structures both with and without accounting for the cavity layer absorption. Absorption in the DBR layers was included in both simulations, leaving the cavity absorption the only change between the two calculations. By making three additional assumptions; that there is no transmission from the bottom of the structure, that the phase shift caused by the extinction coefficient is negligible, and that every absorbed photon creates exactly one collected photogenerated electron, the expected absorption in the optical cavity layer would then be the difference in the reflection profile between the structure which neglects absorption in the cavity layer and the structure which accounts for absorption in the cavity layer, as shown in figure 72. Since the transfer matrix code calculates the reflection percentage of all wavelengths, the actual photogenerated current in the cavity would depend on the number of photons per wavelength in the incident spectrum. The designated application for the detector will ultimately determine the acceptable amount of background absorption in the cavity. For longer wavelength applications, a significant amount of photons with energies which do not correspond to the cavity wavelength are present from the ~300 K room temperature blackbody radiation, as illustrated by figure 73, but the fraction of photogenerated current from these photons can mostly be attributed to the low-energy photons due to the higher energy cost of converting

the high energy photons. For ultra-precise wavelength detection for applications such as chemical sensing, an optical cavity structure can impact LWIR detector technology by filtering nearly all photons except for those compatible with absorption in the cavity layer.

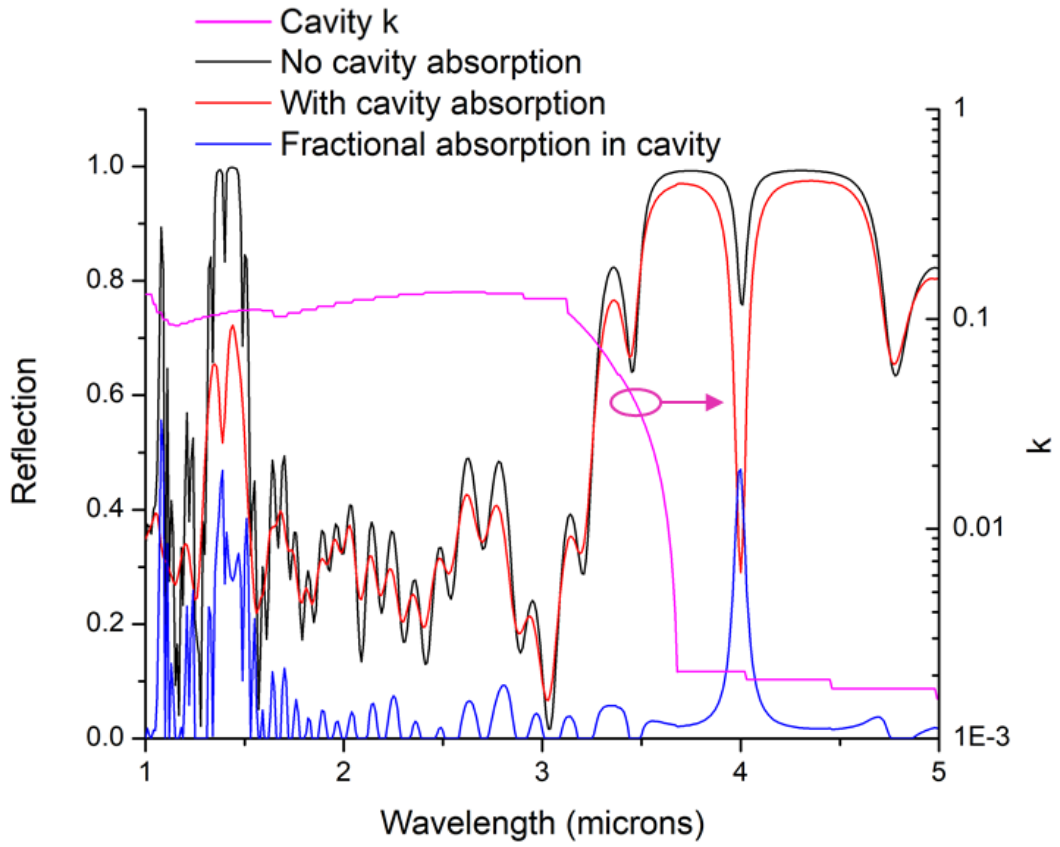

Fig. 72: Potential reflectance and cavity absorption in an InAs optical cavity with ZnTe/GaSb DBRs as a function of wavelength. The cavity absorption can be enhanced by incorporating Sb into the InAs lattice to reduce the band gap energy.

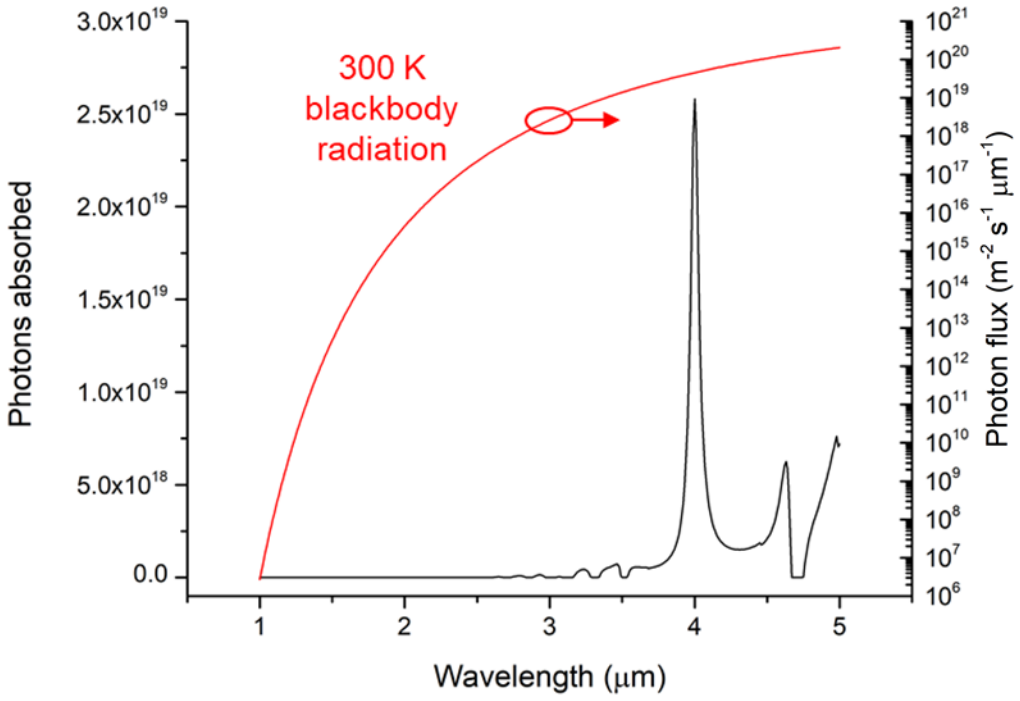

Fig. 73: Simulated cavity absorption of a device illuminated with 300 K blackbody radiation. At room temperature, the high-energy photon noise is negligible, but the low-energy photon noise can pose a problem for IR devices.

Comparison of the isovalent and heterovalent DBR structures shows that by combining lattice-matched III-V and II-VI materials with a high refractive index contrast, the peak reflection, stop bandwidth, and cavity absorption can be enhanced for longer-wavelength applications with thinner DBR structures, as demonstrated by figure 74. From this simulation, if all other parameters such as the peak reflection wavelength and the number of stacks are held constant, the GaSb/ZnTe DBR significantly outperforms the GaSb/AlSb DBR in terms of the peak reflection (95.85 % to 87.61 %) and 90 % peak reflection stop-band width (580 nm to 270 nm) due to the larger refractive index contrast.

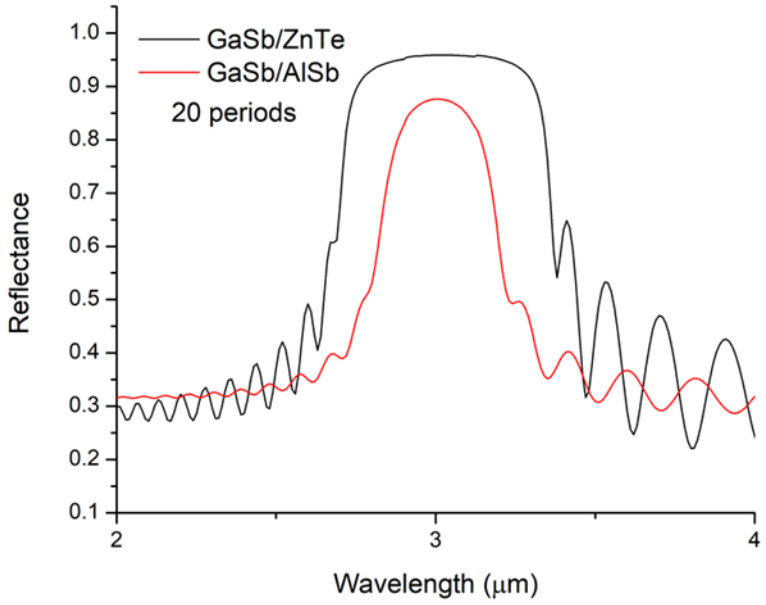

Fig. 74: Comparison of heterovalent and isovalent DBRs with 20 periods for 3 μm applications demonstrating the superior properties of the II-VI/III-V structures with a high refractive index contrast.

CHAPTER 6

CONCLUSIONS AND SUMMARY

This work has shown that with careful optimization of the growth conditions, the non-radiative recombination at the heterovalent interfaces can be reduced sufficiently and optical emission in lattice-matched materials confined by heterovalent and heterocrystalline interfaces can be achieved. It has also been shown that select materials can be used to grow high-quality heterovalent semiconductor heterostructures in a single MBE chamber with minimal cross-contamination effects. While much progress has been made with the growth of novel material combinations and growth techniques, the effects of the heterovalent bonding still need to be examined with respect to how the crystal structure and material characteristics change depending on the polarity and proximity of the interfaces. Atomic diffusion, a critical concern for heterovalent integration, will need to be minimized if devices are to be achieved with these material combinations. This will take careful experimentation with growth conditions, material combinations, and crystal structures to determine the best way to block interdiffusion in each individual material system. While the GaSb/ZnTe material system was shown to be structurally robust by utilizing a substrate temperature ramp and MEE, no ideal solution has yet been demonstrated to completely mitigate the growth temperature mismatch of the GaAs/ZnSe and CdTe/InSb systems while retaining high-quality III-V layers. Controlled doping and carrier transport in the heterovalent heterostructures must be characterized and optimized to realize the device possibilities of different types of heterovalent heterostructures, and carrier isolation from the conductive substrate must also be demonstrated for the Sb-based materials.

Lead chalcogenides were epitaxially integrated with lattice-matched zincblende semiconductors on III-V substrates to demonstrate the ability of forming heterocrystalline heterostructures for IR device applications. A positive band gap – temperature relationship in PbTe was confirmed by PL measurements, and a good agreement was noticed between our results with monolithic PbTe/CdTe heterostructures grown on lattice-matched InSb substrates and those grown on lattice-mismatched GaAs substrates in previous studies. The thermal expansion mismatch affected the PL properties of the PbTe/CdTe heterostructures by reducing the PL intensity from thicker PbTe layers and altering the temperature dependence of the ground state energy. Multiple PL peaks were seen from thicker quantum well samples, but no emission was seen from PbTe layers thicker than 40 nm.

Heterovalent DBRs with a large refractive index contrast between the two layers were modeled, grown, and characterized for MWIR resonant cavity device applications. Due to the close lattice match and the large difference in the refractive indices between the layers, extremely high reflection values can be obtained for IR wavelengths using relatively thin structures compared to state-of-the-art III-V DBRs. GaSb/ZnTe DBRs were demonstrated for MWIR devices lattice-matched to GaSb substrates, which includes materials such as InAs/InAsSb type-2 superlattices, InAsSbBi, and PbSe. Since there are a great deal of MWIR materials lattice-matched to GaSb substrates, and since there are no adequate material pairs for high-reflectivity DBRs on these substrates, the GaSb/ZnTe DBRs are ideal for optical cavity structures lattice-matched to GaSb substrates.

Virtual CdZdTe substrates grown on (211) InSb substrates for HgCdTe device applications have been demonstrated with defect densities as low as 10^6 cm^{-2} in the II-VI layers. The virtual substrates currently under development could be further enhanced by

combining with heterovalent DBR structures for MWIR-LWIR applications, which would enhance the device performance and allow for high-precision IR applications. Additionally, other materials such as Pb or Mg could be incorporated to mitigate outdiffusion of In from the substrate during post-processing steps and allow for flexible, back-side illuminated HgCdTe devices.

After experimenting with the growth of three different material platforms, namely those lattice-matched to GaAs, GaSb, and InSb, some conclusions about the viability of the different material systems can be gathered. The most viable heterovalent system is the GaSb/ZnTe combination since both materials can be grown subsequently without fear of destroying any of the layers. This contrasts both GaAs/ZnSe and InSb/CdTe, where the crystalline quality of the II-VI materials will be adversely affected if the III-V materials are grown at their optimal growth temperatures. Since the GaAs system has nearly lattice-matched AlGaAs available for carrier confinement layers and commercially-available semi-insulating substrates, the integration of ZnSe offers minimal advantages when paired with the potential drawbacks of combining GaAs and ZnSe into multi-layered heterostructures. On the other hand, heterovalent integration with the InSb material system presents many strong potential advantages but can be complicated due to the difficulties associated with growing InSb on CdTe at the moment. PbTe provides an alternate route for the InSb/CdTe material system and PbTe/CdTe heterostructures have the potential to enable room-temperature IR optoelectronic devices if the issues associated with the thermal expansion mismatch between the two materials can be solved for thicker PbTe layers. Heterovalent integration with the InSb material system could also enable high-quality HgCdTe detectors and optical cavities since CdZnTe virtual substrates have been

demonstrated with very low defect densities on (211) InSb substrates. IR DBRs are one of the most promising applications for heterovalent integration, and preliminary growths of heterovalent DBRs have already demonstrated outstanding performance compared to similar isovalent structures. Issues with cross-contamination and interfacial bonding effects have been pointed out in the different systems and a variety of solutions have been proposed to mitigate these issues with heterovalent integration. Further exploration with growth conditions and different substrate orientations and materials will help to further the understanding of the epitaxial relationship between III-V, II-VI, and IV-VI semiconductors.

REFERENCES

[1] A. Y. Cho, “Film Deposition by Molecular-Beam Techniques,” *J. Vac. Sci. Technol.*, vol. 8, no. 5, pp. S31-S38, Sept. 1971.

[2] R. N. Hall, G. E. Fenner, J. D. Kingsley, T. J. Soltys, and R. O. Carlson, “Coherent Light Emission From GaAs Junctions,” *Phys. Rev. Lett.*, vol. 9, no. 9, pp. 366–368, Nov. 1962.

[3] H. Kroemer, “A Proposed Class of Heterojunction Injection Lasers,” *Proc. IEEE*, vol. 51, no. 12, pp. 1782-1783, Dec. 1963.

[4] A. Rogalski, “Infrared detectors: an overview,” *Infrared Phys. Technol.*, vol. 43, no. 3–5, pp. 187–210, Jun. 2002.

[5] M. B. Reine, A. K. Sood, and T. J. Tredwell, “Chapter 6: Photovoltaic Infrared Detectors,” *Semicond. Semimetals*, vol. 18, pp. 201–311, Jan. 1981.

[6] M. B. Reine, “HgCdTe photodiodes for IR detection: a review,” *Proc. SPIE*, vol. 4288, pp. 266–277, June 2001.

[7] W. P. Dumke, J. M. Woodall, and V. L. Rideout, “GaAs-GaAlAs heterojunction transistor for high frequency operation,” *Solid. State. Electron.*, vol. 15, no. 12, pp. 1339–1343, Dec. 1972.

[8] H. Kroemer, “Heterostructure Bipolar Transistors and Integrated Circuits,” *Proc. IEEE*, vol. 70, no. 1, pp. 13-24, Jan. 1982.

[9] A. Zur and T. C. McGill, “Lattice match: An application to heteroepitaxy,” *J. Appl. Phys.*, vol. 55, no. 2, pp. 378–386, Jan. 1984.

[10] M. Cardona and N. E. Christensen, “Band offsets in tetrahedral semiconductors,” *J. Vac. Sci. Technol. B Microelectron. Nanom. Struct.*, vol. 6, no. 4, p. 1285, Jul. 1988.

[11] N. E. Christensen, “Semiconductor heterojunctions and superlattices: Band offsets and electronic structures,” *Philos. Mag. B*, vol. 70, no. 3, pp. 567–581, Sep. 1994.

[12] A. Ohtake *et al.*, “Characterization and control of II-VI/III-V heterovalent interfaces,” *J. Cryst. Growth*, vol. 184–185, pp. 163–172, 1998.

[13] A. Frey, U. Bass, S. Mahapatra, C. Schumacher, J. Geurts, and K. Brunner, “Band offsets and band bending at heterovalent semiconductor interfaces,” *Phys. Rev. B*, vol. 82, no. 19, p. 195318, Nov. 2010.

[14] F. Lu, K. Kimura, S. Q. Wang, Z. Q. Zhu, and T. Yao, “Interfacial properties of ZnSe/GaAs heterovalent interfaces,” *J. Cryst. Growth*, vol. 184–185, pp. 183–187, 1998.

[15] D. Li, Y. Nakamura, N. Otsuka, J. Qiu, M. Kobayashi, and R. L. Gunshor, “Vacancy ordering at heterovalent interfaces,” *Surf. Sci.*, vol. 267, no. 1–3, pp. 181–186, Jan. 1992.

[16] J. Qiu *et al.*, “ZnSe/GaAs heterovalent interfaces: interface microstructure versus electrical properties,” *J. Cryst. Growth*, vol. 111, no. 1–4, pp. 747–751, May 1991.

[17] R. L. Gunshor, M. Kobayashi, N. Otsuka, and A. V. Nurmikko, “Properties of II–VI/III–V heterovalent interfaces,” *J. Cryst. Growth*, vol. 115, no. 1–4, pp. 652–659, Dec. 1991.

[18] R. Nicolini *et al.*, “Local interface composition and band discontinuities in heterovalent heterostructures,” *Phys. Rev. Lett.*, vol. 72, no. 2, pp. 294–297, Jan. 1994.

[19] L. Kassel, J. W. Garland, P. M. Raccah, M. A. Haase, and H. Cheng, “Effects of Zn and Ga interdiffusion on ZnSe/n^+ GaAs interfaces,” *Semicond. Sci. Technol.*, vol. 6, no. 9A, pp. A146–A151, Sep. 1991.

[20] A. T. S. Wee, Z. C. Feng, H. H. Hng, K. L. Tan, R. F. C. Farrow, and W. J. Choyke, “XPS and SIMS studies of MBE-grown CdTe/InSb(001) heterostructures,” *J. Phys. Condens. Matter*, vol. 7, no. 23, pp. 4359–4369, Jun. 1995.

[21] D. L. Smith and V. Y. Pickhardt, “Molecular beam epitaxy of II-VI compounds,” *J. Appl. Phys.*, vol. 46, no. 6, pp. 2366–2374, Jun. 1975.

[22] A. Baczewski, “Epitaxial Growth of ZnSe on GaAs,” *J. Electrochem. Soc.*, vol. 112, no. 6, p. 577, Jun. 1965.

[23] T. Tamura, T. Moriizumi, and K. Takahashi, “ZnTe-InAs Heterojunctions Prepared by Liquid-Phase Epitaxy,” *Jpn. J. Appl. Phys.*, vol. 11, no. 7, pp. 1024–1031, Jul. 1972.

[24] T. Niina, T. Minato, and K. Yoneda, “Ga-Doped ZnSe Grown by Molecular Beam Epitaxy for Blue Light Emitting Diodes,” *Jpn. J. Appl. Phys.*, vol. 21, no. 6, pp. L387-L389, Jun. 1982.

[25] K. Yoneda, Y. Hishida, T. Toda, H. Ishii, and T. Niina, “Growth of undoped, high purity, high resistivity ZnSe layers by molecular beam epitaxy,” *Appl. Phys. Lett.*, vol. 45, no. 12, pp. 1300-1302, Dec. 1984.

[26] M. Aven and J. Devine, “Advances in Injection Luminescence of II-VI Compounds,” *J. Lumin.*, vol. 7, pp. 195-212, Jan. 1973.

[27] J. Nishizawa, K. Itoh, Y. Okuno, and F. Sakurai, “Blue light emission from ZnSe p-n junctions,” *J. Appl. Phys.*, vol. 57, no. 6, pp. 2210-2216, Mar. 1985.

[28] H. Okuyama, K. Nakano, T. Miyajima, and K. Akimoto, “Epitaxial Growth of ZnMgSSe on GaAs Substrate by Molecular Beam Epitaxy,” *Jpn. J. Appl. Phys.*, vol. 30, no. 9B, pp. L1620–L1623, Sep. 1991.

[29] M. C. Tamargo *et al.*, “Multiple Chamber Molecular Beam Epitaxy Growth System: Growth Of GaAs/ZnSe Heterostructures,” 1989, vol. 1037, p. 73.

[30] H. Jeon *et al.*, “Blue and green diode lasers in ZnSe-based quantum wells,” *Appl. Phys. Lett.*, vol. 60, no. 17, pp. 2045–2047, Apr. 1992.

[31] W. Xie *et al.*, “Room temperature blue light emitting p-n diodes from Zn(S,Se)-based multiple quantum well structures,” *Appl. Phys. Lett.*, vol. 60, no. 16, pp. 1999-2001, Apr. 1992.

[32] R. M. Park, *ZnSe growth by conventional molecular beam epitaxy: a review of recent progress*, (Springer Science, 1992) p. 84.

[33] H. E. Ruda, Ed., *Widegap II–VI Compounds for Opto-electronic Applications*, (Springer, Boston, 1992) p. 94.

[34] J. Ren *et al.*, “ZnSe light-emitting diodes,” *Appl. Phys. Lett.*, vol. 57, no. 18, pp. 1901-1903, Oct. 1990.

[35] D. J. Chadi and K. J. Chang, “Self-compensation through a large lattice relaxation in p-type ZnSe,” *Appl. Phys. Lett.*, vol. 55, no. 6, pp. 575–577, 1989.

[36] M. C. Tamargo, *II-VI semiconductor materials and their applications*, (Taylor & Francis, 2002) p. 60.

[37] S. Nakamura, T. Mukai, and M. Senoh, “High-Power GaN P-N Junction Blue-Light-Emitting Diodes,” *Japan. J. Appl. Phys.*, vol. 30, no. 2, p. 12A. 1991.

[38] Y. Zhao *et al.*, “Monocrystalline CdTe solar cells with open-circuit voltage over 1 V and efficiency of 17%,” *Nat. Energy*, vol. 1, no. 6, pp. 16067, 2016.

[39] S. Wang *et al*. “MBE growth of II-VI materials on GaSb substrates for photovoltaic applications,” *J. Cryst. Growth*, vol. 311, no. 15, pp. 2116-2119, Mar. 2009.

[40] G. V. Klimko *et al.*, "Optical and Structural Properties of GaAs/AlGaAs Quantum Wells Grown by MBE in the Vicinity of As-Rich-GaAs/ZnSe Heterovalent Interface," *Acta Phys. Pol. A*, vol. 126, no. 5, pp. 1184–1186, 2014.

[41] S. Krishna, M. N. Kutty, C. Chen, S. Myers, J. D. Phillips, and E. Plis, "Passivation of long-wave infrared InAs/GaSb superlattice detectors with epitaxially grown ZnTe," *Infrared Technol. Appl. XL*, vol. 9070, no. June 2014, p. 907010, 2014.

[42] Q. Liu, X. Zhang, L. B. Abdalla, and A. Zunger, "Transforming Common III-V and II-VI Semiconductor Compounds into Topological Heterostructures: The Case of CdTe/InSb Superlattices," *Adv. Funct. Mater.*, vol. 26, no. 19, pp. 3259–3267, May 2016.

[43] A. A. Toropov, I. V. Sedova, S. V. Sorokin, Y. V. Terent'ev, E. L. Ivchenko, and S. V. Ivanov, "Resonant spin-dependent electron coupling in a III-V/II-VI heterovalent double quantum well," *Phys. Rev. B - Condens. Matter Mater. Phys.*, vol. 71, no. 19, pp. 2–7, 2005.

[44] J. Lu *et al.*, "Towards defect-free epitaxial CdTe and MgCdTe layers grown on InSb (001) substrates," *J. Cryst. Growth*, vol. 439, pp. 99–103, Apr. 2016.

[45] J. Venables, *Introduction to surface and thin film processes*, (Cambridge University Press, 2000) p.146.

[46] J. Fan, L. Ouyang, X. Liu, J. K. Furdyna, D. J. Smith, and Y. H. Zhang, "GaSb/ZnTe double-heterostructures grown using molecular beam epitaxy," *J. Cryst. Growth*, vol. 371, pp. 122–125, 2013.

[47] M. Funato, S. Fujita, and S. Fujita, "Energy states in ZnSe-GaAs heterovalent quantum structures," *Phys. Rev. B*, vol. 60, no. 24, pp. 16652–16659, Dec. 1999.

[48] S. V. Ivanov *et al.*, "II-VI/III-V structures with a heterovalent interface in the active region: New opportunities in band engineering," *Phys. Status Solidi C Conf.*, vol. 1, no. 6, pp. 1468–1476, 2004.

[49] D. R. Menke *et al.*, "An x-ray photoelectron spectroscopy study of bonding at II–VI/III–V heterovalent interfaces," *J. Vac. Sci. Technol. B Microelectron. Nanom. Struct.*, vol. 9, no. 4, p. 2171, Jul. 1991.

[50] T. Nakayama, "Electronic Structures of Heterovalent (001) Semiconductor Superlattices: GaP/ZnS and GaAs/ZnSe," *J. Phys. Soc. Jpn.*, vol. 61, no. 7, pp. 2458-2468, Jul. 1992.

[51] Z.-Y. He, C. Campbell, M. B. Lassise, Z.-Y. Lin, J. J. Becker, and Y.-H. Zhang, "Monolithically integrated CdTe/InSb visible/midwave-infrared two-color detectors," *IR phys. & Technol.*, vol. 97, pp. 58-62, Mar. 2019.

[52] E. Litwin-Staszewska, W. Szymańska, and R. Piotrzkowski, “The Electron Mobility and Thermoelectric Power in InSb at Atmospheric and Hydrostatic Pressures,” *Phys. status solidi*, vol. 106, no. 2, pp. 551–559, Aug. 1981.

[53] F. Lu, K. Kimura, S. Q. Wang, Z. Q. Zhu, T. Yao, “Interfacial properties of ZnSe/GaAs heterovalent interfaces,” *J. Cryst. Growth*, vol. 184-185, pp. 183-187, 1998.

[54] J. Fan, X. Liu, J. K. Furdyna, and Y. H. Zhang, “ZnTe/GaSb distributed Bragg reflectors grown on GaSb for mid-wave infrared optoelectronic applications,” *Appl. Phys. Lett.*, vol. 101, no. 12, pp. 4–7, 2012.

[55] P. Fellgett, “Conclusions on Multiplex Methods,” *Le J. Phys. Colloq.*, vol. 28, no. C2, pp. C2-165-C2-171, Mar. 1967.

[56] B. D. Cullity and S. R. Stock, Elements of X-ray Diffraction, 3rd ed. (Prentice Hall, Ney Jersey, 2001), p. 131.

[57] P. F. Fewster, “X-ray analysis of thin films and multilayers,” *Reports Prog. Phys.*, vol. 59, no. 11, pp. 1339–1407, 1996.

[58] J. H. Neave, B. A. Joyce, P. J. Dobson, and N. Norton, “Dynamics of film growth of GaAs by MBE from Rheed observations,” *Appl. Phys. A*, vol. 31, no. 1, pp. 1-8, May 1983.

[59] M. B. Lassise, P. Wang, B. Tracy, G. Chen, D. J. Smith, and Y.-H. Zhang, “Growth of II-VI/III-V heterovalent quantum structures,” *J. Vac. Sci. Technol. B*, vol. 36, no. 2, p. 02D110, Mar. 2018.

[60] M. B. Lassise, T. McCarthy, B. Tracy, D. J. Smith, and Y.-H. Zhang, “Structural and optical properties of heterovalent PbTe/CdTe/InSb heterostructures grown by molecular beam epitaxy,” *Appl. Phys. Lett.*, submitted 2019.

[61] X. Zhang *et al.*, “Structural Characterization of Integrated II-VI and III-V Heterostructures for Solar Cell Applications,” *J. Elect. Mater.*, vol. 38, no. 8, pp. 1558-1562.

[62] S. Ramesh, N. Kobayashi, and Y. Horikoshi, “Study of high-quality ZnSe/GaAs/ZnSe single quantum well and ZnSe/GaAs heterostructures,” *J. Cryst. Growth*, vol. 115, no. 1–4, pp. 333–337, Dec. 1991.

[63] J. R. Arthur, “Interaction of Ga and As_2 Molecular Beams with GaAs Surfaces,” *J. Appl. Phys.*, vol. 39, no. 8, pp. 4032–4034, Jul. 1968.

[64] S. Tatarenko, B. Daudin, D. Brun, V. H. Etgens, and M. B. Veron, “Cd and Te desorption from (001), (111) *B* , and (110) CdTe surfaces,” *Phys. Rev. B*, vol. 50, no. 24, pp. 18479–18488, Dec. 1994.

[65] A. Krost, W. Richter, D. R. T. Zahn, and O. Brafman, “Compound formation and large microstrains at the interface of II-VI/III-V semiconductors detected by Raman spectroscopy,” *Semicond. Sci. Technol.*, vol. 6, no. 9A, pp. A109–A114, Sep. 1991.

[66] W. G. Wilke and K. Horn, “Valence-band offset and interface formation in ZnTe/GaSb (110) studied by photoemission using synchrotron radiation,” *J. Vac. Sci. Technol. B Microelectron. Nanom. Struct.*, vol. 6, no. 4, p. 1211, Jul. 1988.

[67] J. Qiu *et al.*, “Characterization of Ga2Se3at ZnSe/GaAs heterovalent interfaces,” *Appl. Phys. Lett.*, vol. 58, no. 24, pp. 2788–2790, 1991.

[68] M. P. Halsall, D. Wolverson, J. J. Davies, B. Lunn, and D. E. Ashenford, “Ga2Te3and tellurium interfacial layers in ZnTe/GaSb heterostructures studied by Raman scattering,” *Appl. Phys. Lett.*, vol. 60, no. 17, pp. 2129–2131, 1992.

[69] G. E. Franklin, T. Miller, and T.-C. Chiang, “Growth phases of ZnTe on GaSb(100),” *Phys. Rev. B*, vol. 46, no. 7, pp. 3940–3947, Aug. 1992.

[70] J. Tersoff, M. D. Johnson, and B. G. Orr, “Adatom Densities on GaAs: Evidence for Near-Equilibrium Growth,” *Phys. Rev. Lett.*, vol. 78, no. 2, pp. 282–285, Jan. 1997.

[71] M. C. Tamargo, M. J. S. P. Brasil, R. E. Nahory, R. J. Martin, A. L. Weaver, and H. L. Gilchrist, “MBE growth of the (Zn,Cd)(Se,Te) system for wide-bandgap heterostructure lasers,” *Semicon. Sci. & Technol.*, vol. 6, no. 9A, 1991.

[72] S. Ramesh, N. Kobayashi, and Y. Horikoshi, “Migration-enhanced epitaxy growth and characterization of high quality ZnSe/GaAs superlattices,” *Appl. Phys. Lett.*, vol. 57, no. 11, pp. 1102–1104, 1990.

[73] S. Zhang and N. Kobayashi, “Photoluminescence and structure properties of GaAs/ZnSe quantum wells,” *Appl. Phys. Lett.*, vol. 60, no. 7, pp. 883-885, 1992.

[74] S. Ramesh, N. Kobayashi, and Y. Horikoshi, “High-quality ZnSe/GaAs superlattices: MEE growth, and structural and optical characterization,” *J. Cryst. Growth*, vol. 111, no. 1–4, pp. 752–756, May 1991.

[75] H. H. Farrell, M. C. Tamargo, J. L. de Miguel, F. S. Turco, D. M. Hwang, and R. E. Nahory, “‘Designer’ interfaces in II-VI/III-V polar heteroepitaxy,” *J. Appl. Phys.*, vol. 69, no. 10, pp. 7021–7028, May 1991.

[76] D. Y. Kim, T. W. Kang, and T. W. Kim, “Optical properties of a strained GaAs/Si heterostructure after rapid thermal annealing,” *Thin Solid Films*, vol. 250, no. 1–2, pp. 202–205, Oct. 1994.

[77] L. F. Luo, K. F. Longenbach, and W. I. Wang, “p-channel modulation-doped GaSb field-effect transistors,” *Electron. Lett.*, vol. 27, no. 5, p. 472, 1991.

[78] J. Fan *et al.*, “Growth and material properties of ZnTe on GaAs, InP, InAs and GaSb (0 0 1) substrates for electronic and optoelectronic device applications,” *J. Cryst. Growth*, vol. 323, no. 1, pp. 127–131, May 2011.

[79] E. T. Yu *et al.*, “Interfacial reactions and band offsets in the AlSb/GaSb/ZnTe material system,” *Phys. Rev. B*, vol. 46, no. 20, pp. 13379–13388, Nov. 1992.

[80] P. T. Webster *et al.*, “Measurement of InAsSb bandgap energy and InSb/InAsSb band edge positions using spectroscopic ellipsometry and photoluminescence spectroscopy,” *J. Appl. Phys.*, vol. 118, no. 24, p. 245706, Dec. 2015.

[81] D. L. Rode, “Electron Transport in InSb, InAs, and InP,” *Phys. Rev. B*, vol. 3, p. 3287, May 1971.

[82] K. Sugiyama, “Properties of CdTe films grown on InSb by molecular beam epitaxy,” *Thin Solid Films*, vol. 115, no. 2, pp. 97-107, May 1984.

[83] D. Zahn *et al.*, “The influence of Cd overpressure in the molecular beam epitaxy of InSb/CdTe heterostructures: A combined raman and infrared spectroscopy study,” *Appl. Surf. Sci.*, vol. 41-42, pp. 497-503, Jan. 1990.

[84] G. Karczewski *et al.*, “Midinfrared electroluminescence from PbTe/CdTe quantum dot light-emitting diodes,” *Appl. Phys. Lett.*, vol. 98, no. 2, p. 021106, 2011.

[85] J. C. Woolley and P. N. Keating, “Solid solubility of In_2Se_3 in some compounds of zinc blende structure,” *J. Less Common Mater.*, vol.3, no. 3, pp. 194-201, Jun. 1961.

[86] W. Lei, J. Antoszewski, and L. Faraone, “Progress, challenges, and opportunities for HgCdTe infrared materials and detectors,” *Appl. Phys. Rev.*, vol. 2, no. 4, 2015.

[87] J.-P. Faurie, S. Sivananthan, and P. S. Wijewarnasuriya, “Current status of the growth of HgCdTe by molecular beam epitaxy on (211)B CdZnTe substrates,” *Proc. SPIE*, vol. 1735, p. 141, Dec. 1992.

[88] W. J. Everson, C. K. Ard, J. L. Sepich, B. E. Dean, G. T. Neugebauer, and H. F. Schaake, “Etch pit characterization of CdTe and CdZnTe substrates for use in mercury cadmium telluride epitaxy,” *J. Electron. Mater.*, vol. 24, no. 5, pp. 505–510, May 1995.

[89] P. Findlay, C. Pidgeon, R. Kotitschke, A. Hollingworth, and B. Murdin, “Auger recombination dynamics of lead salts under picosecond free-electron-laser excitation,” *Phys. Rev. B - Condens. Matter Mater. Phys.*, vol. 58, no. 19, pp. 12908–12915, 1998.

[90] V. Hinkel, H. Haak, C. Mariani, L. Sorba, K. Horn, and N. E. Christensen, "Investigation of the bulk band structure of IV-VI compound semiconductors: PbSe and PbTe," *Phys. Rev. B*, vol. 40, no. 8, pp. 5549–5556, 1989.

[91] G. Springholz, *Molecular Beam Epitaxy of IV-VI Semiconductors: Multilayers, Quantum Dots, and Device Applications*. In E. Henini, *MBE from Research to Mass Production*, (Elsevier, Massachusetts, 2013), p. 266.

[92] W. E. Tennant, "Limits of Infrared Imaging," *Int. J. High Speed Electron. Syst.*, vol. 20, no. 03, pp. 529–539, Sep. 2011.

[93] J. R. Meyer *et al.*, "Auger coefficients in type-II InAs/Ga1−xInxSb quantum wells," *Appl. Phys. Lett.*, vol. 73, no. 20, pp. 2857–2859, Nov. 1998.

[94] B. C. Connelly, G. D. Metcalfe, H. Shen, and M. Wraback, "Study of recombination mechanisms limiting the performance of Sb-based III-V type II superlattices for infrared detectors," vol. 8155, p. 81550L, 2011.

[95] P. M. Young, C. H. Grein, H. Ehrenreich, and R. H. Miles, "Temperature limits on infrared detectivities of InAs/$In_xGa_{1-x}Sb$ superlattices and bulk $Hg_xCd_{1-x}Te$," *J. Appl. Phys.*, vol. 74, no. 7, pp. 4774–4776, Oct. 1993.

[96] K. G. Svantesson and N. G. Nilsson, "The temperature dependence of the Auger recombination coefficient of undoped silicon," *J. Phys. C Solid State Phys.*, vol. 12, no. 23, pp. 5111–5120, Dec. 1979.

[97] K. K. Lee, W. Priyantha, and T. H. Myers, "Growth and valence band offset measurement of PbTe/InSb heterojunctions," *Appl. Phys. Lett.*, vol. 100, no. 5, pp. 2–6, 2012.

[98] J. Si, S. Jin, H. Zhang, P. Zhu, D. Qiu, and H. Wu, "Experimental determination of valence band offset at PbTe/CdTe(111) heterojunction interface by x-ray photoelectron spectroscopy," *Appl. Phys. Lett.*, vol. 93, no. 20, p. 202101, Nov. 2008.

[99] G. R. Savich, J. R. Pedrazzani, D. E. Sidor, and G. W. Wicks, "Benefits and limitations of unipolar barriers in infrared photodetectors," *Infrared Phys. Technol.*, vol. 59, pp. 152–155, Jul. 2013.

[100] G. Springholz, G. Bauer, and G. Ihninger, "MBE of high mobility PbTe films and PbTe/Pb1-xEuxTe heterostructures," *J. Cryst. Growth*, vol. 127, no. 1–4, pp. 302–307, 1993.

[101] A. Hochreiner *et al.*, "Midinfrared electroluminescence from PbTe/CdTe quantum dot light-emitting diodes," *Appl. Phys. Lett.*, vol. 98, no. 2, p. 021106, Jan. 2011.

[102] C. Yan *et al.*, "Experimental Observation of Dirac-like Surface States and Topological Phase Transition in $Pb_{1-x}Sn_xTe$ (111) Films," *Phys. Rev. Lett.*, vol. 112, no. 18, p. 186801, 2014.

[103] P. H. O. Rappl *et al.*, "Molecular beam epitaxial growth of high quality $Pb_{1-x}Sn_xTe$ layers with $0 < x < 1$," *J. Cryst. Growth*, vol. 191, no. 3, pp. 466-471, 1998.

[104] S. Jin, C. Cai, G. Bi, B. Zhang, H. Wu, and Y. Zhang, "Two-dimensional electron gas at the metastable twisted interfaces of CdTe/PbTe (111) single heterojunctions," *Phys. Rev. B*, vol. 87, no. 23, p. 235315, Jun. 2013.

[105] B. Zhang *et al.*, "Phonon blocking by two dimensional electron gas in polar CdTe/PbTe heterojunctions," *Appl. Phys. Lett.*, vol. 104, no. 16, p. 161601, Apr. 2014.

[106] R. Rosman and A. Katzir, "Lifetime calculations for Auger recombination in lead-tin-telluride," *IEEE J. Quantum Electron.*, vol. 18, no. 5, pp. 814–817, May 1982.

[107] K. Koike *et al.*, "Structural and electronic properties of PbTe (rocksalt)/CdTe (zinc-blende) interfaces," *Appl. Surf. Sci.*, vol. 254, no. 1, pp. 397-400, 2007.

[108] Y. W. Tsang and M. L. Cohen, "Calculation of the temperature dependence of the energy gaps in PbTe and SnTe," *Phys. Rev. B*, vol. 3, no. 4, pp. 1254–1261, 1971.

[109] B. Houston, R. E. Strakna, and H. S. Belson, "Elastic Constants, Thermal Expansion, and Debye Temperature of Lead Telluride," *J. Appl. Phys.*, vol. 39, no. 8, pp. 3913–3916, Jul. 1968.

[110] M. E. Straumanis and C. D. Kim, "Lattice Parameters, Thermal Expansion Coefficients, Phase Width, and Perfection of the Structure of GaSb and InSb," *J. Appl. Phys.*, vol. 36, p. 3822, 1965.

[111] K. Koike, T. Honden, I. Makabe, F. Ping Yan, and M. Yano, "PbTe/CdTe single quantum wells grown on GaAs (1 0 0) substrates by molecular beam epitaxy," *J. Cryst. Growth*, vol. 257, pp. 212–217, 2003.

[112] L. G. Ferreira, "Deformation potentials of lead telluride," *Phys. Rev.*, vol. 137, no. 5A, 1965.

[113] G. Springholz and G. Bauer, "Systematic study of PbTe (111) molecular-beam epitaxy using reflection high-energy electron-diffraction intensity oscillations," *J. Appl. Phys.*, vol. 77, no. 2, pp. 540-552, Jan. 1995.

[114] D. J. Griffiths, *Introduction to Quantum Mechanics*, (Prentice Hall, New Jersey, 1995) p. 61.

[115] G. D. Cole *et al.*, “High-performance near- and mid-infrared crystalline coatings,” *Optica*, vol. 3, no. 6, pp. 647-656, (Jun. 2003).

[116] H. A. Macleod, *Thin Film Optical Filters*, (Taylor & Francis, Boca Raton, 2010) p. 219.

[117] W. Kuhn *et al.*, “The MOVPE growth and doping of ZnTe,” *Semicond. Sci. Technol.*, vol. 6, no. 9A, pp. A105–A108, Sep. 1991.

APPENDIX A

HETEROVALENT MBE SYSTEM OPERATION

Chamber D is a VG-V80 MBE system originally configured for the growth of HgCdTe IR detectors and reconfigured to grow III-V, II-VI, and IV-VI semiconductors in a single growth chamber. Mercury is extremely mobile and requires a relatively high flux rate for growth, and because of this every part taken off of the machine can be considered Hg contaminated and **should not** be reused on any of the other systems in the lab. The entire system consists of four isolatable vacuum chambers connected by gate valves. The controllers for the various pumps are on the bottom of the electronics rack. The ion pump controllers are on the bottom right and should always be in protect mode, they should be in start mode only when started below pressures of 10^{-6} Torr and only for a few seconds. Isolated ion pumps can be opened to the chamber if the pressure in the chamber is below 10^{-5} Torr by slowly opening the gate valve and keeping an eye on the ion pump current displayed on the front panel. There are four chambers are labeled as the load lock, the prep chamber, the buffer chamber, and the growth chamber. Only one gate valve should be opened at a single time when transferring wafers, and the valve should be open only for the shortest possible time to complete a transfer. There are two cart tracks, one in the prep chamber and one in the buffer chamber, which are used to transfer wafers from chamber to chamber. The track can be moved with the knob on the left, and the cart can be moved with the knob on the right. The system is old and the tracks do not always cooperate; for example, the prep chamber track cannot be moved to the left if the cart is sitting at the left end of the track. The track and cart do not move completely independent of each other, so both knobs must be used simultaneously to avoid sticking. The load lock is an intermediary chamber which holds the cassette, a device that can be removed to load and unload samples. The cassette should **never** touch anything that is not UHV clean, and should always be

removed or loaded using clean UHV-compatible gloves. The load lock pressure is measured with an ion gauge and is pumped with a single 60 L/s ion pump which can be isolated by closing the adjacent gate valve. Operators must fully understand vacuum pumps and gauges before attempting to vent the load lock. The prep chamber connects to the load lock via the elevator that lowers the cassette into the prep chamber. Always make sure the cart is out of the path of the elevator before moving the elevator up or down. The elevator can cause serious damage to the cart if it is clipped, and the parts required to repair the cart are expensive and not always readily available. **Please take two seconds to check that the cart is out of the way before moving the elevator**, a small amount of prevention will save everyone in the lab an enormous headache. It is not fun to repair the cart, and making this mistake is the easiest way to become the most unpopular person in the lab. Additionally, the prep chamber also houses the heating stage. The heating stage is controlled with the Emeralt software on the computer and is used to outgas samples and holders to remove contaminants before being transferred into the growth chamber. The buffer chamber serves little purpose other than additional UHV wafer storage with the parking stage. Only wafer holders which have already been outgassed can be moved into the buffer chamber. The whiteboard on the server rack should be updated to show the location and condition of every wafer holder in use to avoid confusion and mishaps. Both the prep chamber and the buffer chamber have a dedicated 400 L/s ion pump which can be isolated with a gate valve, and each has a single ion gauge to monitor the pressure. The gate valve on the prep chamber ion pump leaks, so during vents the prep chamber ion pump should be turned off and backfilled with nitrogen. The growth chamber is obviously the most significant chamber on the system. There are many dozens of flanges on the growth

chamber alone, which means leak checking this chamber requires diligence and patience. The surface area inside the growth chamber is also much larger than any of the other chambers, so the growth chamber is always the slowest to pump down after a full system vent. The growth chamber has three pumps, a 400 L/s ion pump, a titanium sublimation pump (TSP) and a cryopump. The pressure ranges for the operation of the various vacuum pumps can be found in table A1. The cryopump is controlled with a pneumatic valve which requires about 50 psi to operate properly and can be opened to chamber pressures below 10^{-5} Torr. The valve has two Swagelok connections, one closes the valve when pressure is applied and the other opens the valve. These are clearly marked and fairly self-explanatory. The growth chamber also has two ion gauges, one for the baseline pressure and one on the beam flux monitor (BFM) which can be moved in front of the manipulator to calibrate fluxes.

Table A1: Vacuum pumps on the MBE system and their pressure ranges.

	Turbo/roughing pump	Cryopumps	Ion pumps
Max operating pres.	760 Torr	10^{-3} Torr	10^{-5} Torr
Min obtainable pres.	10^{-6} Torr	10^{-10} Torr	10^{-10} Torr

The chambers are connected in two spots (buffer chamber and load lock) by bakeable angle valves to a nitrogen gas manifold. The nitrogen manifold is typically isolated from the vacuum chambers except when venting or pumping down. In the case of loading and unloading, only the load lock should be connected to the manifold while the other three chambers remain isolated under UHV conditions. The nitrogen gas manifold

is connected to the turbopump by an angle valve, the growth chamber cryopump by a needle valve, and the pressurized nitrogen gas lines by a needle valve, regulator, and N2 filter. The nitrogen gas lines pressurize all of the pneumatic valves on the system and can provide an inert system overpressure for venting the chambers. The nitrogen gas line attaches to the cryopump's gate valve, the shutter control N2 distributor, and the N2 manifold with separate regulators to control the pressure at each point. The gas line is also connected to a gas hose with a needle valve in case anything on the system needs to be purged with gas, for example, in the case of a long water cooling failure. The N2 gas line's main valve is in the ceiling close to the phase separator. To turn off the gas supply to the system the green valve must be turned off, or the regulator must be closed on the main supply (the regulator attached to the turbopump exhaust pipe). Before operating the system, the user must understand the importance of each of these connections, how to open and close each valve, and under which conditions the valves should be open or closed. Failure to understand these connections could lead to errors such as unexpected venting, damaging or destroying gauges and pumps, system contamination, or personal injury.

To load a sample, the load lock needs to be isolated and vented. Make sure your desired wafer holder is on the cassette in the load lock before starting the vent procedure, consult figure A1 for the manifold valve positions. To vent the load lock:

- Make sure the load lock is completely closed and isolated.
- Shut the gate valve to isolate the 60 L/s ion pump on the load lock.
- Turn off the load lock ion gauge.
- Make sure the valve from the manifold to the buffer chamber is **closed**. This should never be open unless venting the entire system.

- Open the angle valve to connect the load lock to the manifold.
- Turn the needle valve below the manifold slowly to introduce N2 gas to the load lock. You can stop turning the valve once you hear the N2 start to flow.
- Wait for the top of the load lock to open, this should only take a few seconds.
- With a UHV clean glove, reach into the load lock (make sure you don't open the load lock with the same hand you grab the cassette since the top of the load lock is not clean) and pull out the cassette.
- With clean gloves, load your wafer into the desired wafer holder and mark on the whiteboard which wafer you loaded onto which holder.
- With clean gloves, place the wafer holder back into the load lock. Twist the cassette until it "clicks" and sinks down into the load lock. There is a small hole on the bottom of the cassette that should lock into a peg in the load lock.
- Turn off the N2 at the needle valve, open the angle valve to the turbo pump (ensure it is not spinning first by listening for the high-frequency whine of the rotating blades), and turn the knob to start the turbo pump. You will also need to press down on the cap of the load lock to ensure the system pumps down properly.
- After 15-20 minutes, you can check the ion gauge on the turbo pump. To activate the display, flip on the switch underneath the display. Once the

display is on, the HFIG1 control should be highlighted. Press the + button to switch it to “on” and press the “OK” button.

- Once the turbo pump ion gauge reads below 10^{-6} Torr, switch on the load lock ion gauge and open the gate valve to the load lock ion pump. Ensure the load lock ion pump stays on by monitoring the front of the control panel. If the ion pump shuts down, you can restart the pump by switching the pump off protection mode and flipping the switch. Make sure you put the pump back into protected mode after about 10-15 seconds. This is true for both the 60 L/s pump and the larger 400 L/s pumps.
- Close the angle valve that connects the load lock to the manifold, then close the angle valve that connects the manifold to the turbo pump in this order to ensure the manifold stays under vacuum.
- Turn off the turbo pump ion gauge by highlighting the HFIG1 control, hitting the “-“ button to switch it to “off”, then hit “OK”. The ion gauge filament should stop glowing. Once this is done you can turn off the turbo pump and the vent is complete.

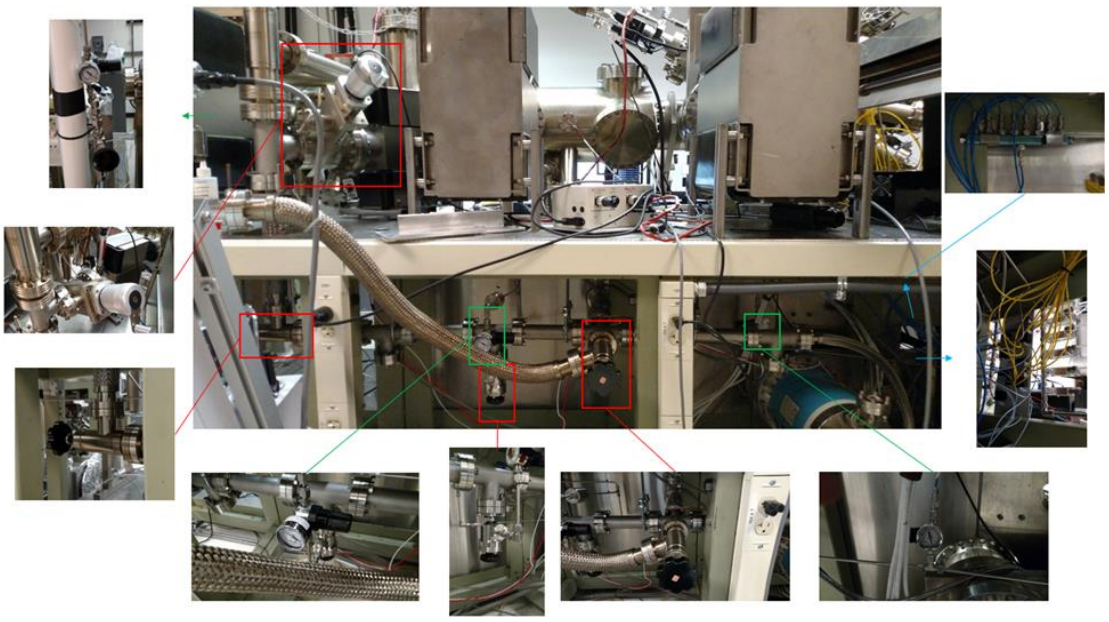

Fig. A1: Valves (red lines), regulators (green lines), and shutter manifold (blue lines) associated with the N2 lines and vent manifold. Valves outlined in red are used for venting the load lock.

The growth chamber has a residual gas analyzer (RGA) which is a mass spectrometer that measures the partial pressure of different gasses in the system. This needs to be refreshed periodically, such as when vents or leak checks are performed. To stop the scan, hit the red stop sign and then save the data. If you are venting the growth chamber, be sure to turn off the filament, the electron multiplier, and disconnect the RGA head. These three tasks can be performed by pressing the corresponding icons on the taskbar above the graph. To enter leak check mode, stop the scan and select the "mode" tab. Before you hit "go", click "save as" and label the data as the date and time using the same standard as the other files. Once the data is saved you can start the scan, be sure to always save when you complete the leak check or switch modes. To set the RGA back to normal operation, you can switch the mode back to PvT and open an older file so you do

not have to manually input the gas masses into the software. Once the RGA is in PvT mode and the correct gas masses are on screen, hit “save as” and label the data with the date again. Once the graph is saved, you can hit “go” and the RGA will resume normal operation. You can change the graph axis under the “graph” tab, and you can change the gas molecules monitored the system scans by using the “scan parameters” under the “scan” tab.

Careful attention must be paid to every single instrument on the growth chamber, remember that if a critical component in the growth chamber fails then the entire system needs to be vented. This can cause large setbacks in projects and lead to more contamination in the chamber. Please be sure to understand the equipment and materials before attempting to use the growth chamber. The growth chamber has eight effusion cell ports, each with its own corresponding pneumatic shutter port. Effusion cells are essentially a crucible made of thermally conductive, electrically resistive material, usually either graphite or pyrolytic boron nitride (pBN), surrounded by a resistive filament made of a refractory metal, commonly tantalum, and cooled by water circulated through stainless steel cooling coils. When power is supplied to the filament, the crucible is heated and the source material is be evaporated from the cell. The temperature of the cell varies dramatically depending on which part you are observing. We would like to know the actual temperature of the source material inside the crucible, but making this measurement is not very practical. Therefore cells are typically manufactured with thermocouples that measure the temperature right next to the crucible. Thermocouples can read the temperature by measuring the difference in work functions between two dissimilar metals at a junction. The thermocouples are read by the Eurotherm controllers, which act as the

point of communication between the cells, power supplies, and control computer. It is important to understand how Eurotherms PID controllers operate, specifically how to switch from automatic to manual mode, how to set limits, alarms, PID parameters and ramp rates, how to enter configuration mode, and how the Eurotherms interface with the power supplies and control computer. Recognize that the reading on the Eurotherm might not always be correct. The thermocouples can be shorted or the configuration can be switched which will significantly alter the temperature reading. If you observe unexpected outgassing on the ion gauges or RGA, or if the power supply output is higher or lower than normal, then you may have a problem with your thermocouple or Eurotherm settings. Troubleshooting is made easier by paying attention to your hardware and keeping detailed notes.

Effusion cells are not universal for all source materials, the heat shielding, crucible material and design, cooling water flow, and filament and thermocouple resistance vary from cell to cell. Take the time to familiarize yourself with each different cell and the source material properties, specifically the vapor pressure and flux curves. Read any available manuals before using a cell you are unfamiliar with. If you are installing a new cell or material, a new flux curve must be generated. A beam equivalent pressure (BEP) flux curve can be generated by measuring the flux of the cell with the BFM ion gauge down in the measurement position. The BEP flux curve is not a final calibration and is not ideal to report for publications. A more standard flux curve is the flux ratio curve, which will be discussed later. **Never** move the manipulator when the BFM is down or serious damage to the BFM or manipulator will occur. Be sure to leave visible notes on the system so everybody knows the BFM is down – there is no interlock on the system to avoid this.

Serious damage to the cells can occur in many different ways, and no cell design is completely perfect. Table A2 contains the operating temperatures of some of the effusion cells used on the chamber. Use common sense when operating cells, some general rules to follow with all cells:

- Never heat a cell above 100 °C when water is left sitting in the cell cooling lines – the water will boil and release steam, which etches stainless steel and will cause a leak in the cooling coils.
- Never turn on the water supply to introduce water to the empty cooling lines when any of the cells are above 100 °C for the same reason.
- 300 °C is the highest temperature the cells can safely be raised without LN2 flow to the cryopanel – stainless steel outgasses heavily when heated above a certain point and the large thermal gradients and poor thermal conductivity can cause leaks at the flanges or damage the cryopanel due to thermal expansion.
- When heating or cooling the bulk zone of a valved cracker cell, ensure that the valve is open approximately halfway – otherwise the rapidly changing temperature could force the valve into the crucible, which could damage the crucible. Never heat a cell above the posted setpoints and check every night before leaving the lab that the cells have been set to their standby temperatures
- Don't heat the cells faster than 15 °C/min – faster ramp rates require higher power output from the power supply. The power supplies all have current limits, so the actual temperature will lag behind the working

setpoint on the controller and cause the Eurotherm to overcompensate, which will make the temperature oscillate about your setpoint.

- Cracker cell valves should be opened before changing the temperature of the bulk zone to avoid damaging the crucible.

Table A2: Operating temperatures and Emeralt call commands. Emeralt should reflect this in the working conditions, above is red and below is green. This can be checked or reconfigured in the Emeralt configuration file.

Cell (emeralt call)	Standby temp	Operating range	Outgas temp
Ga (ga.t)	600	850-980	1000
In (in.t)	600	700-880	920
As bulk (asb.t)	370	340-380	420 (depleting)
As cracker (asc.t)	1000	900-1050	1200
Sb (sb.t)	280	300-500	520
Zn (zn.t)	100	150-280	300
Cd (cd.t)	100	140-240	275
Te bulk (teb.t)	200	275-400	450
Te tip (tet.t)	225	300-425	475
Se bulk (seb.t)	270	240-300	320 (depleting)
Se cracker (sec.t)	810	800-1000	1200
Substrate (sub.t)	200	250-840	400

The cooling lines for the effusion cells are supplied by a water chiller and reservoir in the storage room. There is no backup power for the chiller, so if there is a power outage the water circulation in the cells will stop. Therefore, to be prepared for emergencies, all operators must know how to fill and replace the reservoir, how to set up the reservoir so it feeds water into the chiller without overflowing, how to turn on the chiller after a failure, how to selectively shut off the water in the lab, how to purge the water lines, how to read the temperature of the water, how to attach and detach the water lines from the cells, and how to measure the water flow through the cells. The reservoir must be filled with **distilled water**, a distilled water supply is located in the first floor hallway of PSD. We have two reservoirs, the backup should be filled at all times in case of emergencies. The water will overflow out of the reservoir if the cap is left unsealed. When replacing the reservoir make sure that the spout is open and the cap is sealed. The water lines on chamber D can be monitored and isolated at the flow meters next to the electronics rack. The water supply and return are next to the chamber A control computer. The supply is on top and return on the bottom, both are labelled chamber D.

The RHEED system on chamber D is antiquated and requires some finesse to operate properly. Please refer to the manual for more detailed information. The switches on the control box are off when flipped up and on when down, which is counterintuitive. The LED lights should turn on when the power, filament, and HV are turned on. To warm up the RHEED gun, increase the voltage to 15 kV at a pace of 1 kV every 2 seconds. Next, increase the current to above 2 A. You should take at least 30 seconds to reach 2 A, otherwise the gun can arc and damage the filament. The filament current won't start to increase until you reach about 2 A, no emission will be visible on the screen until the

filament current starts to rise. Ensure the gate is open on the RHEED window. If you still cannot see any emission on the screen, turn the X knob to about 9 and the Y knob to 0, this will ensure the gun is pointed directly at the screen and a single dot should appear. The intensity can be increased by increasing the current, but the gun is unstable so the intensity will rise and fall as the current increases. Increase the intensity so that the dot becomes a large saturated feature on the screen, then move the position around until a pattern from the sample is visible on the screen. The RHEED gun will periodically change intensity so you may need to adjust the current knob throughout your growth. The TSP will also alter the RHEED emission so you will either need to readjust the gun or turn the TSP off for the growth. Remember to close the window shutter when not checking the RHEED to keep the window from getting coated. There is no blanking feature on this system unlike the RHEED guns on chambers A and B.

Loading samples into the chamber D growth chamber is completely different from A and B, so be sure you understand how the manipulator works before attempting to load a sample. Instead of swinging the entire manipulator into the loading position, this manipulator has a gate that lowers from a hinge. The manipulator is controlled by a control box at the bottom of the power rack. The controller connects to a control box, which is then hooked up to the manipulator apparatus. If the control box is unplugged the manipulator will not work. The manipulator has a "home" setting which is defined by a metal rod on the gear next to the manipulator motor. As the manipulator turns, the rod passes through a sensor. When the rod touches the sensor, the manipulator reads this as the home position. This should be when the manipulator gate opens downwards so that samples can be loaded, but the manipulator is magnetically coupled and this might not

always be the case if someone has used the manipulator improperly. There is an interlock that prevents the manipulator gate from being lowered if it is not at home, but this does not work if the controller is turned off. The gate is lowered by the apparatus above the motor. Turning the cylinder raises or lowers the gate. Sensors on the back of the apparatus tell the control box if the gate is closed or open. The manipulator will not rotate if the controller reads that the gate is open. If you want to manually rotate the manipulator for something such as a RHEED measurement, you will need to turn off the controller to unlock the manipulator. **Always be sure you watch the manipulator gate as you lower it**, if it is out of position, the wafer holder and the sample will be dumped into the chamber. Also make sure the BFM is not lowered into the chamber. The filament on the manipulator heater is old and unfortunately causes temperature oscillations. Be aware of this when making RHEED measurements or monitoring the temperature. Whenever a sample is not in the chamber, the blank holder should be placed on the manipulator to avoid any errors that could cause damage to the manipulator filament.

To load a sample, make sure the cells and manipulator are at their standby temperatures and the manipulator is in the correct home position by checking both the controller and the growth chamber interior. Check the pressures of the buffer and growth chamber before opening the gate valve. Make sure you have outgassed your sample and it is sitting on the parking stage in the buffer chamber. The switches on the manipulator controller should be set to (**local**/remote) and (go/**index**). The lights should look like the following: Flip (off until the gate is open), go home (off), at home (on). If the manipulator is not at home, press the switch that only says "home" down once to bring the manipulator into the home position. When you have visually checked all of the equipment, open the

manipulator gate while watching inside the chamber to make sure the gate opens properly. When the manipulator gate is parallel to the ground, you can place your sample on the transfer cart, open the gate valve, and bring the sample into the growth chamber. As stated before, the cart and rail design on this system is not very well thought out. You will need to use the wobble stick to place the sample holder in the manipulator, then with the wobble stick still holding the sample on the manipulator arm, move the cart rail out of the chamber. After the cart is moved, remove the wobble stick from under the sample and bring it back to the resting position and close the gate valve between the growth and buffer chamber. This procedure is required because the cart blocks the wobble stick from being moved from under the manipulator in the transfer position. Always make sure something is under your sample before moving equipment in the chamber. Close the manipulator gate and start the rotation of the manipulator by flipping the switch from "index" to "go".

The chamber D control computer runs Linux so take some time to familiarize yourself with the operating system before trying to run programs. There is a metal USB drive (named "Transcend" under devices) on the front of the computer with information such as the Emeralt user manual and operating guide. Please look through these documents if you are unfamiliar with the Emeralt connections and operation. **Important - do not disconnect either of the devices named "primary", this is the hard drive and will cause serious problems if you disconnect them**! Emeralt runs off of a USB drive on the back of the computer called user_01. The Emeralt files can be found in the directory "/run/media/emeralt/ user_01/emeralt/emeralt/", this includes the kernel, the data logs, and the configuration file. The configuration file (emeralt.cfg) is a text file that specifies how the computer communicates with the controllers. This should not be changed unless you

know what you are doing, and only if you have discussed the changes with the user responsible for the system. The effusion cells, manipulator heater, heating stage, and shutters are controlled by the Emeralt program on the computer. You should know how to restart Emeralt in case it gets shut down or crashes. To start Emeralt, go to the chameleon icon on the bottom left of the computer desktop and click the "console" icon (black and grey > sign on the left of the popup window) twice to bring up two separate consoles. In both terminals, type "cd /run/media/emeralt/user_01/emeralt/emeralt/". Next, in only one of the terminals, type "su" to designate that terminal a superuser and enter the password. Wait a few seconds and the command prompt should turn red, when this happens type "./em_kernel" and wait until you receive the READY message. After doing this and the superuser terminal reads READY, go to the other terminal and type "java –jar em_gui.jar" to launch the emeralt GUI. Emeralt should start up and you will be ready to operate. If you have not used Emeralt before, please read the user manual to familiarize yourself with the commands and programs associated with the software. Commands such as "reach(XX.t, ###, ##/m)" will ramp an analog device such as a Eurotherm (e.g. ga.t or sub.t) to a specified temperature (in the middle) at a rate of ## degrees per minute (can be /s for seconds but this should not be used). Remember that all commands in Emeralt are case sensitive, and devices typically registered in lowercase. Use this instead of typing "XX.t = ###, which will automatically put the setpoint at whatever you type immediately. Commands like "shut(cd.s)" or "open(in.s)" will open or close a binary device, i.e. the cell shutters. To get an idea of the commands needed to run the system, take a look at the other programs to see how cells are ramped and when shutters are opened, etc. To exit Emeralt (no need to do this when done, but you may need to do this to restart the kernel), close the

GUI then go to your superuser terminal (will be emeralt : em_kernel) and hit Ctrl+C. Wait for the command prompt to reappear and enter “exit” twice to close the window. In the other terminal, enter “exit” and Emeralt will be terminated.

The Eurotherm controllers and power supplies work in tandem with the computer to control the temperature of all the analog devices on the chamber, this includes the effusion cells, heating stage, and manipulator heater. The power supplies should always be operated in current limited mode, and current limits should be set on all equipment to avoid frying any filaments. You can view the power supply limits by pressing the preview (prev) button on the front, this will bring up the maximum set values for the voltage and current of the supply. These should not be changed unless you know the power limits of the filament being supplied with power. The substrate is a low-resistance filament so the current required to reach temperatures above 500 °C is very high, please turn the current limit down to 6 A when the manipulator is at standby. The Eurotherms control the power supplies by telling them what voltage to output, this can be seen by the bar scale on the Eurotherm display. Temperature, ramp rate, and output voltage limits can be set in the Eurotherms, see the Eurotherm guide for more information. The Eurotherms can be set to automatic mode (i.e. you specify the output voltage of the power supply) by pressing the a/man button on the front display, this may be useful in the event of a power outage. Use the “page” button on the bottom right of the display to toggle through the controller’s menus and the back button to make selections. Nothing in the Eurotherm should be changed without consulting the individual responsible for the system, and all documentation should be updated once anything is changed.

Certain daily procedures should be followed when operating chamber D. Always check the Eurotherms, ion gauges, cooling water circulation, and vacuum pumps before you start and after you finish your growth. Before loading a sample into the growth chamber, it needs to be outgassed on the heating stage in the prep chamber. The heating stage should not be taken above 500 °C, this is different from the heating stage on chambers A/B which is water cooled and can withstand higher temperatures. Use the Emeralt program corresponding to your substrate material to outgas your sample. Certain cells need to be outgassed to remove impurities if they have not been used for some time. Use the Emeralt programs to outgas the cells, the general idea is to raise the cell temperature higher than your operating temperature until any contaminants on the RGA reading start to trend downward. **Always make sure the blank flange is in the manipulator, the gate is closed, and the growth chamber is isolated before outgassing or serious damage to the manipulator can occur**. The flux of the effusion cells should also be monitored every couple of weeks, this can be done using the BFM. If the surface stoichiometry ratios and growth rates are already calibrated, then the curves can be recalibrated by matching the flux and shifting the curve so that the temperatures give the correct flux reading. The growth rate and stoichiometry ratios are directly related to the BEP flux at a standard substrate temperature, so you only need to check one data point (preferably near the operating point) to recalibrate the data. To generate a new set of data, which is needed after venting the growth chamber, you will need to generate a BEP curve for a range of temperatures using the BFM. The standard procedure is to heat the cell with the shutter closed, open the shutter for a set time limit such as 10 seconds, record the flux and the background pressure, close the shutter, and repeat 2-3 times to get an average BEP flux.

Do this in temperature increments of 5-10 °C, depending on if you're measuring a low temperature or high temperature cell. The surface stoichiometry points can be found by growing with an overpressure, lowering the overpressure flux, and using RHEED to monitor either a shift in the surface reconstruction pattern or by measuring RHEED oscillations until the growth rate starts to decrease. Make note of the 1:1 stoichiometry point, the growth rate, and the substrate temperature and print the data for all users.